“Railplug Ignition System for Enhanced Engine Performance and Reduced Maintenance”
Final Technical Report
September 30, 2001 - December 31, 2004

DK Ezekoye, Co-PI, Prof. of Mech. Engineering
Matt Hall, Co-PI, Prof. of Mech. Engineering
Ron Matthews, Co-PI, Prof. of Mech. Engineering
August 2005

DE-FG26-01NT41334

The University of Texas
1 Longhorn Station, C2200
Austin, TX 78712

DISCLAIMER

ABSTRACT

This Final Technical Report discusses the progress that was made on the experimental and numerical tasks over the duration of this project. The primary objectives of the project were to 1) develop an improved understanding of the spark ignition process, and 2) develop the railplug as an improved ignitor for large bore stationary natural gas engines.

We performed fundamental experiments on the physical processes occurring during spark ignition and used the results from these experiments to aid our development of the most complete model of the spark ignition process ever devised. The elements in this model include 1) the dynamic response of the ignition circuit, 2) a chemical kinetics mechanism that is suitable for the reactions that occur in the plasma, 3) conventional flame propagation kinetics, and 4) a multi-dimensional formulation so that bulk flow through the spark gap can be incorporated. This model (i.e., a Fortran code that can be used as a subroutine within an engine modeling code such as KIVA) can be obtained from Prof. Ron Matthews at rdmatt@mail.utexas.edu or Prof. DK Ezekoye at dezekoye@mail.utexas.edu.

Fundamental experiments, engine experiments, and modeling tasks were used to help develop the railplug as a new ignitor for large bore natural gas engines. As the result of these studies, we developed a railplug that could extend the Lean Stability Limit (LSL) of an engine operating at full load on natural gas from $\phi = 0.59$ for operation on spark plugs down to $\phi = 0.53$ using railplugs with the same delivered energy (0.7 J). However, this delivered energy would rapidly wear out the spark plug. For a conventional delivered energy (<0.05 J), the LSL is $\phi = 0.63$ for a spark plug. Further, using a permanent magnet to aid the plasma movement, the LSL was extended to $\phi = 0.54$ for a railplug with a delivered energy of only 0.15 J/shot, a typical discharge energy for commercial capacitive discharge ignition systems. Here, it should be noted that railplugs and the associated ignition circuit should not cost much more than a conventional spark ignition system. Additionally, it is believed that the railplug performance can be further improved via continued research and development.

TABLE OF CONTENTS

EXECUTIVE SUMMARY

This Final Technical Report discusses the progress that was made on the experimental and numerical tasks over the duration of this project. The primary objectives of the project were to 1) develop an improved understanding of the spark ignition process, and 2) develop the railplug as an improved ignitor for large bore stationary natural gas engines.

Due to these two objectives, the experimental subtasks involved 1) detailed measurements regarding the physical processes occurring during spark ignition, and 2) measurements of the factors that affect railplug performance. Similarly, the modeling subtasks involved developing an improved model for the conventional spark ignition process and developing a model for railplug performance and ignition.

The four phases of spark ignition are pre-breakdown, breakdown, arc, and glow. We performed measurements of all four phases, including the effects of spark gap size and pressure (we will perform additional tests in the near future to examine the effects of temperature and gas composition). The primary importance of these measurements is that they aided our development of a detailed model for the spark ignition process.

Via this ARES project, we developed the most complete model of the spark ignition process ever devised. The elements in this model include 1) the dynamic response of the ignition circuit, 2) a chemical kinetics mechanism that is suitable for the reactions that occur in the plasma, 3) conventional flame propagation kinetics, and 4) a multi-dimensional formulation so that bulk flow through the spark gap can be incorporated.

The dynamics of the ignition circuit are important because the dynamic response of the ignition circuit dictates the rate of electrical energy deposition to the gases within the spark gap. Our ignition circuit model necessarily includes a submodel for the gases within the spark gap as an equivalent electronic system. Our circuit model incorporates models for breakdown voltage, arc voltage, and glow voltage and, perhaps most importantly, the arc-to-glow transition. Most prior investigators have marked the arc-to-glow transition as occurring when the current reaches some threshold value. In fact, the transition current is a function of the electrode material. Our model for the arc-to-glow transition is an extension of a prior model that can be used to predict the current at the end of the arc regime given the cathode (ground electrode) area, the cathode fall voltage (15 V), and the cathode surface temperature. Our research team recommends using the melting temperature of the cathode material as the cathode surface temperature due to evidence that the arc-to-glow transition occurs when the melt can no longer be sustained.

Our model for the spark ignition process also incorporates a chemical kinetics mechanism that is suitable not only for flame propagation but also the reactions occurring within the plasma. Here, it must be noted that our ignition model is the first model ever developed that includes plasma reactions. The inclusion of plasma kinetics is important because these reactions are endothermic during breakdown and the early stages of arc but are a new route to thermal energy release as the plasma cools below 6000 K. As the plasma cools, the energy liberation due to recombination reactions involving the ionized species that were generated at very high temperature is an additional route to thermal energy liberation. This occurs on times scales when the young spark kernel is still very “fragile” and prior to significant energy release by flame propagation reactions. That is, as the plasma cools to below 6000 K, the plasma reactions must be accounted for because the recombination

reactions help maintain a high temperature prior to the onset of the flame propagation reactions.

We developed our ignition model using the Flux Corrected Transport technique so that we could include the "blast wave" that emanates away from the spark gap due to the very high rate of energy deposition during breakdown. Although this blast wave has been included in some prior models of the ignition process, it was not clear whether or not the blast wave plays an important role in the physics of ignition. We found that the blast wave is important because it is a major sink (along with the endothermic plasma reactions) for the energy deposition from the ignition circuit. However, it is only important during the breakdown phase of the ignition process and extremely early in the arc phase (it has almost completely dissipated by 5 μs for the conditions simulated in our study). Another reason the blast wave is important is that rapid expansion behind the blast wave results in the pressure in the region of the spark gap rapidly decreasing to less than that of the unburned gas. In turn, this results in the inflow of "cold" unburned gas adjacent to the insulator and electrodes.

The conclusions from our model of the conventional spark ignition process included 1) vortices form near the corners of the electrodes (and, thus, a multi-dimensional formulation is important) and 2) because heat transfer is a "slow" process relative to the electrical-to-thermal energy conversion process, heat losses to the electrodes are negligible during breakdown and the early stages of arc (10s of μs).

The various elements of this model were developed over the duration of this project by several graduate students. Before graduating, the final PhD student on this project, Ozgur Eciki, will assemble all of these elements into a single Fortran code. Once completed, this version of the model (i.e., a Fortran code that can be used as a subroutine within an engine modeling code such as KIVA) can be obtained from Prof. Ron Matthews at rdmatt@mail.utexas.edu or Prof. DK Ezekoye at dezekoye@mail.utexas.edu.

Fundamental experiments, engine experiments, and modeling tasks were used to help develop the railplug as a new ignitor for large bore natural gas engines. Most importantly, it was found that the sharp discontinuity between the initiation gap and the rails in a prior railplug design prevented the arc from moving downstream and had to be eliminated. This was accomplished by tapering the rails from a small rail spacing at the initiation gap to a larger rail spacing at the exit end of the railplug. We also found that this taper angle should be as small as practical. As a result of these experimental and numerical studies, we developed a railplug that could extend the Lean Stability Limit (LSL) of an engine operating at full load on natural gas from $\phi = 0.59$ for operation on spark plugs down to $\phi = 0.53$ using railplugs with the same delivered energy (0.7 J). However, this delivered energy would rapidly wear out the spark plug. For a conventional delivered energy (<0.05 J), the LSL is $\phi = 0.63$ for a spark plug. Further, using a permanent magnet to aid the plasma movement, the LSL was extended to $\phi = 0.54$ for a railplug with a delivered energy of only 0.15 J/shot, a typical discharge energy for commercial capacitive discharge ignition systems. Here, it should be noted that railplugs and the associated ignition circuit should not cost much more than a conventional spark ignition system. Additionally, it is believed that the railplug performance can be further improved via continued research and development.

1. INTRODUCTION

The US Department of Energy established the Advanced Reciprocating Engine Systems (ARES) program to improve large-bore stationary natural gas engines. The goals of the ARES program are to increase fuel efficiency to 50%, decrease emissions of the oxides of nitrogen (NOx) by a factor of 10, and decrease the cost of power by 10% which implies a corresponding decrease in maintenance costs.

Driven to pursue better fuel efficiency and lower emissions, engine researchers have been investigating IC engine operation with higher boost pressures and even leaner or more dilute (e.g., with EGR) mixtures. Both place greater demands on the ignition system. Increased boost pressure requires higher breakdown voltage. Also, the minimum ignition energy increases and the burning rate decreases as the mixture becomes more dilute, such that the slow burn, partial burn, and misfire limits are encountered when sufficiently lean or dilute mixtures are used. In turn, these result in decreased brake thermal efficiency and increased hydrocarbon emissions. This is a very challenging problem for stationary large-bore natural gas engines, and a potential barrier to use in the distributed power generation market. The ignition systems currently in use are derived from automotive applications and are not designed or optimized for the lower speed, higher load, and leaner conditions of large-bore natural gas engines. There is, therefore, an acute need for a more robust ignition system for large-bore natural gas engines offering longer ignitor life and better ignition characteristics.

With that motivation, engine researchers have been exploring a variety of new ignition systems, such as laser-induced ignition (Ronney, 1994; McMillian et al., 2004), and pilot-fuel ignition (Saito et al., 2001). Although laser-induced ignition and pilot-fuel ignition systems have some potential benefits, because of the high demands on the components and intrinsic difficulties such as optical window fouling for laser ignition and misfire at idle and part-load for pilot-fuel ignition, such novel systems still face barriers before they become practical.

Via the ARES program, DOE funded a project at The University of Texas (UT) that consisted of two simultaneous tasks: 1) development of an improved understanding and an improved model for the spark ignition process, and 2) development of the railplug as a new ignitor for large bore natural gas engines. Extension of the spark ignition model as an aid to railplug design and development was included as a task under the railplug development objective.

In the following two subsections, the physics governing railplug operation are reviewed and implications about railplug durability that can be extracted from knowledge about spark plug wear are discussed. Subsection 1.3 is a guide to the organization of the remainder of this report.

1.1. Railplug Physics

Due to the limitations of the alternative ignition sources discussed above, other types of advanced ignitors are of interest. The railplug is a miniaturized railgun that has been developed as an ignitor for internal combustion engines (Hall et al., 1991; Matthews et al., 1992; Gao et al., 2004a, 2004b, 2005a, 2005b; Hari et al., 2005). When a sufficiently high voltage is applied across the rails to electrically breakdown the gap between them, an arc jumps across the rails. The current loop that is attained by the electrical current flowing down one rail, across the arc, and back up the other rail produces an electromagnetic field. An

electromagnetic force, or Lorentz force, is thereby created as a consequence of the interaction of the self-induced magnetic field with the ions in the plasma arc. This Lorentz force accelerates the plasma moving along the electrodes, as illustrated in Figure 1.

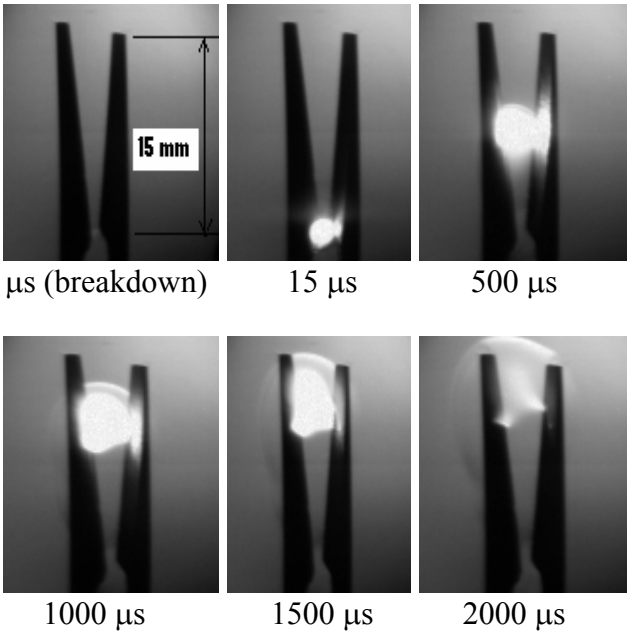

Figure 1. Images of arc moving down the rails of a "parallel" railplug. Rail length = 15 mm, initiation gap = 0.8 mm, capacitance = 600 μF, and capacitor charge voltage = 210 V, discharge duration 1.6 ms, and energy 3 J/shot. High-speed photography rate 70,000 frames/s at a shutter speed 2 μs.

It is known that ignitability and flame propagation near the plug gap of an operating engine are significantly affected by many factors such as the local composition of the mixture, spark plug gap size, electrode size, duration of energy deposition, method of energy deposition, and flow environment (Gao et al., 2004a). The discharge energy can be deposited at one fixed point with a spark plug, or the energy can be deposited over a relatively large area, as with a railplug. The high-speed arc motion results in a fast burning rate and the ability to burn leaner mixtures than might ordinarily be possible (Hall et al., 1991). The high-speed plasma movement also helps to improve the railplug durability since the energy is deposited over a much larger electrode surface area and the duration of the arc at any specific point decreases. Thus, any method that helps arc motion improves both the ignitability and the durability of a railplug.

In Figure 1, the direction of the self-induced magnetic field is perpendicular to the plane of the paper. As just noted, the electron flow is up one rail, across the arc, and down the other rail. This current loop results in the Lorentz force (Hall et al., 1991):

$$F = J \times B \tag{1}$$

where J is the current flow per unit area and B is the strength of the local magnetic field. If a constant current (i) is supplied to parallel rails, the Lorentz force is:

$$F = \frac{1}{2} L' i^2 \quad (2)$$

where L' is the inductance per unit length of the rails. For cylindrical conductors of radius r that are removed from an external conducting boundary, the inductance per unit length is:

$$L' = 0.4 \times 10^{-6} \left[\ln(d/r) + (1/4) - (1/R_a) \right] \quad (3)$$

in μH/m, where d is the separation distance between the centroids of each rail and R_a is the aspect ratio, which is the rail length divided by the rail separation.

It can be seen from Equations 1-3 that the Lorentz force is affected by the deposited energy (current and voltage), the local magnetic field strength, and the geometry of the rails (rail size, gap size, and rail length). Generally, there are two types of railplug designs: parallel electrodes and coaxial electrodes. Parallel railplugs have better performance [Gao et al., 2004a, 2004b] since they have a higher inductance gradient (L') than coaxial railplugs. Therefore, this research focused on parallel railplug design and optimization.

1.2. Implications from Studies of Spark Plug Wear

For spark plugs, numerous studies have been performed on the effects of the rate and duration over which energy is delivered to the spark, attempting to determine the optimum spark power, energy, and duration (e.g., Anderson and Lim, 1985; Anderson, 1987; Maly et al., 1983; Pischinger and Heywood, 1988; Cho et al., 1992). However, the results from different researchers are not all consistent. Generally, high power, short duration ignition systems, such as breakdown systems, can enhance the initial kernel growth under low turbulence conditions (e.g., low engine speeds). With very lean mixtures and high turbulence levels, long duration discharges may become more effective than a high power short discharge. A long duration system appears to provide a large enough ignition window to partially mask the effects of cycle-to-cycle variations, which is more important for the operating engine when the mixture becomes leaner or more dilute. It should be noted that none of these engine studies used methane or natural gas as the test fuel. Because of the unique ignition characteristics of natural gas, such as the long "ignition delay" and slow laminar burning speed relative to gasoline (Karim et al., 1989), the effects of the duration of energy deposition on the ignitability are unknown.

Another issue that needs to be considered for railplug design is the thermal load of railplug electrodes. For large-bore natural gas engines, in-cylinder pressures and mixture temperatures are very high (relative to light-duty gasoline engines) at the time of ignition (42 bars and 973 K) due to the high boost pressure. Hot spots may exist on the electrodes of the ignitor, causing pre-ignition problems. High electrode temperatures can also reduce railplug durability. The wear of spark plug electrodes is classified as "sparking wear" caused by spark discharge, and "oxidation wear" caused by high electrode temperature (Hori et al., 2003). Wear caused by spark discharge is attributed to the arc and glow discharge phases of ignition. During the arc discharge phase, the electrodes are heated to a few thousand degrees Celsius locally and wear because the material melts and some of the melt is ejected from the surface. Compared with the arc phase, electrodes experience lower wear rates during the glow phase (Maly, 1984). Therefore, it is necessary to use a material with a higher melting point to improve the resistance to spark wear. To reduce electrode oxidation wear, besides using materials resistant to oxidation, it is necessary to decrease the electrode thermal load as much as possible.

In the present study, the electrode temperature was measured in both a constant volume bomb and in an operating natural gas engine. A heat transfer model was developed to aid railplug design. The heat transfer analysis will be discussed in Section 2.2.C.

1.3. Organization of the Remainder of this Report

The experimental measurements and results are discussed in Section 2. The numerical models and predictions are discussed in Section 3. Section 4 provides the conclusions that can be drawn from the results of this project.

2. EXPERIMENTAL METHODS AND RESULTS

To design the railplug as a new ignitor to meet the ignition challenges of large-bore natural gas engines (e.g., low-speed, high load, high boost pressure, and very lean mixtures), it is necessary to improve and optimize both the geometry and the electronic circuit designs. In addition to the geometric and circuit optimizations, the effects of deposited energy and current shape on ignition performance were investigated.

Section 2.1 is a discussion of our fundamental experiments of the spark discharge process. Section 2.2 covers the experiments that were performed to optimize railplug performance, both with respect to the electronic circuit and the geometry of railplugs. The engine experiments that we performed are discussed in Section 2.3.

2.1. Fundamental Studies of the Spark Discharge Process

A thorough investigation of the literature revealed a lack of published information regarding measurements of spark discharge currents, voltage, and energy deposition. In addition, conditions for arc and glow discharges are vague in the literature. Because of this, we initiated a study of these phenomena.

Time-resolved current and voltage measurements for an inductive automotive spark system were made, as well as measurements of the total energy delivered to the spark gap. The measurements were made in air for a range of pressures from 1-18 bar, at ambient temperature (~298 K). The measured voltage and current characteristics were found to be functions of many ignition parameters; including spark gap size, internal resistance of the spark plug and high tension wire, and gas pressure. The voltages were measured either at the top of the spark plug or at the spark gap. The measurements were made at different time resolutions to more accurately resolve the voltage and current behavior throughout the discharge process. This was necessary because the breakdown event occurs on a time scale much shorter than the arc and glow phases. The breakdown, arc, and glow voltages were found to be functions of spark plug resistance, gas density, and spark plug gap. Spark duration was found to decrease as either pressure or gap was increased. The transition from the arc to glow phase is usually distinguished by a sudden rise in the voltage across the gap. At pressures above ~7 bar, this arc-to-glow transition was not observed, suggesting that a glow phase was not present. Energy delivered to the gap increased with increasing pressure. The effective resistance of the spark gap during discharge was about twice as large for the glow phase as the arc phase.

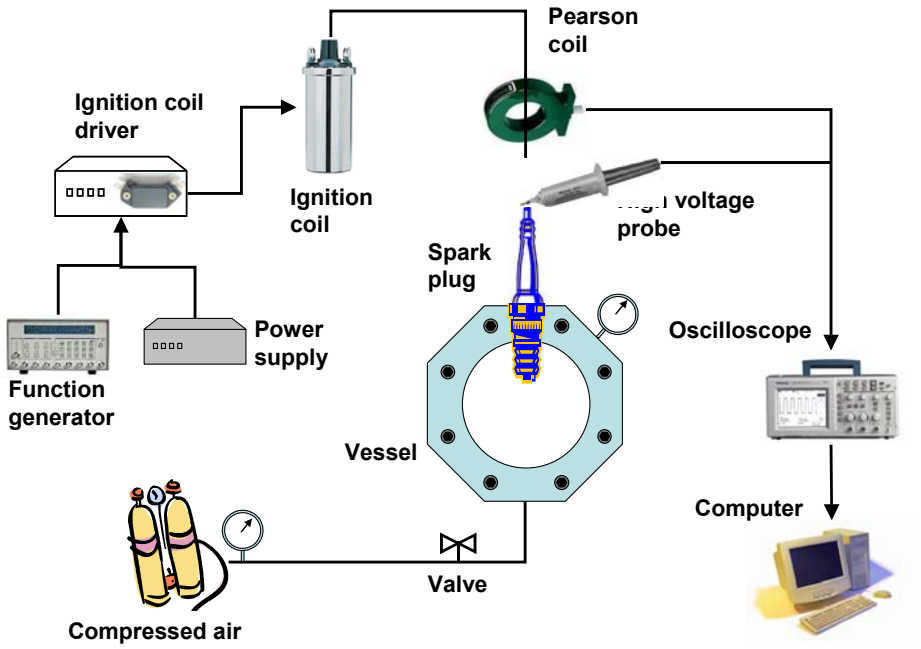

Figure 2. Schematic of the experimental setup for the fundamental studies of spark discharge.

The measurements were performed using standard automotive ignition components. As shown in Figure 2, the setup consisted of an ignition coil (MSD Model 8207) triggered by a NAPA Model TP45 ignition module. The ignition module was triggered by a TTL pulse from a function generator. That signal was electrically isolated by an opto-isolator and boosted by a transistor circuit before connecting to the ignition module. An 11 kΩ high-tension ignition wire was used for most of the measurements; a solid copper conductor was substituted for some measurements investigating effects associated with spark plug and ignition wire resistance. No attempt was made to maximize the resonant efficiency of the system by considering L-C factors. A variety of new and used off-the-shelf 14 mm automotive spark plugs were examined. The internal resistances of the spark plugs ranged from 0-25 kΩ.

2.1.A. *Effects of the Resistance of the High Tension Wire and Spark Plug*

The cumulative spark energy delivered to the spark plug was calculated by integrating the measured voltage at the top of the spark plug and the current over the duration of the discharge. The measurements at the "top" of the spark plug have one upstream resistance (the high tension wire) and two downstream resistances: the internal resistance of the spark plug and the effective resistance of the gas within the spark gap. The measurements at the gap end of the spark plug have both hardware resistances (high tension wire and spark plug) upstream and only the gas phase resistance downstream.

The spark duration was found to be a decreasing function of the spark plug resistance. Figure 3 shows the measured mean spark duration versus the series resistance of the high-

tension lead (11 kΩ) or solid copper conductor (near zero kΩ) and the spark plug at a pressure of ~1 bar. As shown in Figure 3, the spark duration decreases quickly as the series resistance increases from near zero. The spark duration then continues to decrease, but very slowly as the series resistance increases to values above a few kohm.

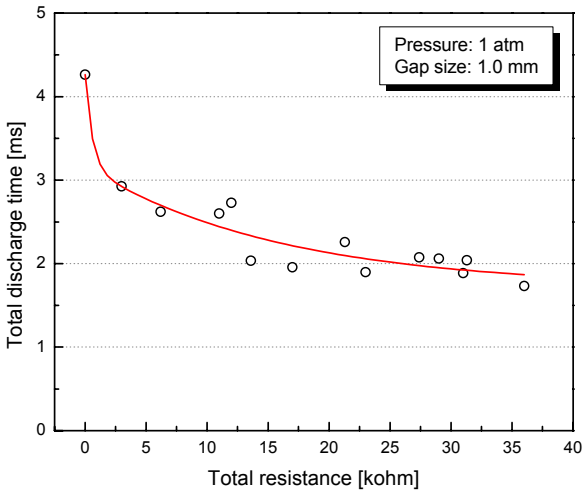

Figure 3. Spark duration versus series resistance of the high-tension wire and of the spark plug.

Figure 4 shows that the rate at which the energy is delivered to the spark plug tends to increase with an increase in the series resistance (high tension wire and spark plug). The rate of energy delivered is also faster at the higher pressure, as shown in Figure 3. The total energy delivered to the spark plug was greater for higher series resistances, where some of that energy was dissipated. All of the voltage measurements presented in the rest of this report were made at the gap to eliminate the effect of the internal resistance of the spark plug.

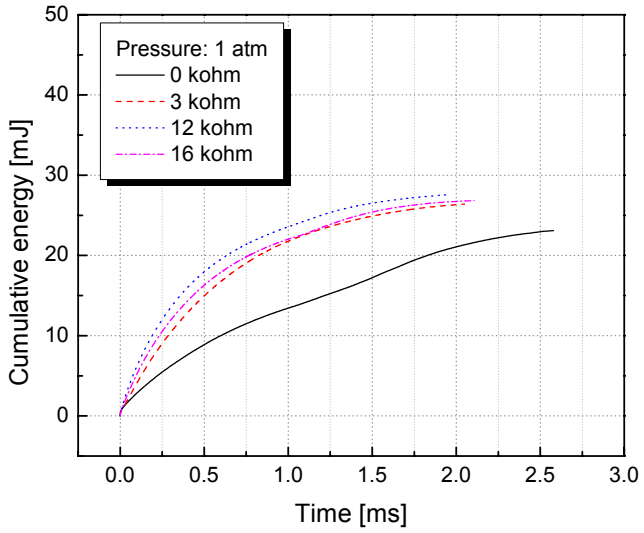

a

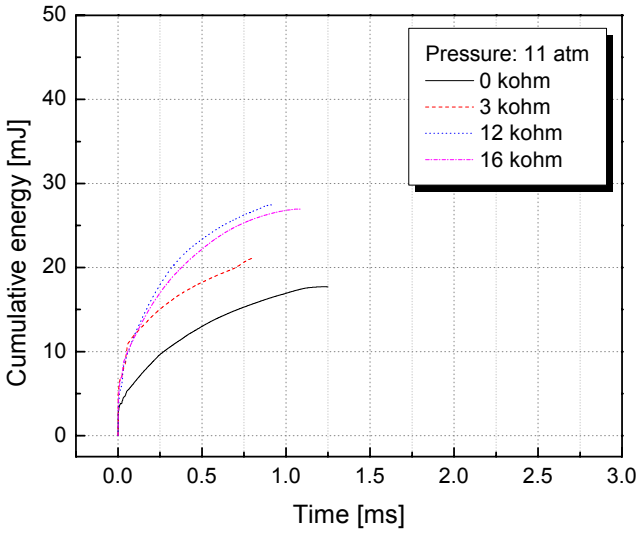

b

Figure 4. Cumulative energy to the spark plug versus time for a range of the series resistances of the high-tension wire and spark plug; a) 1 bar, b) 11 bar.

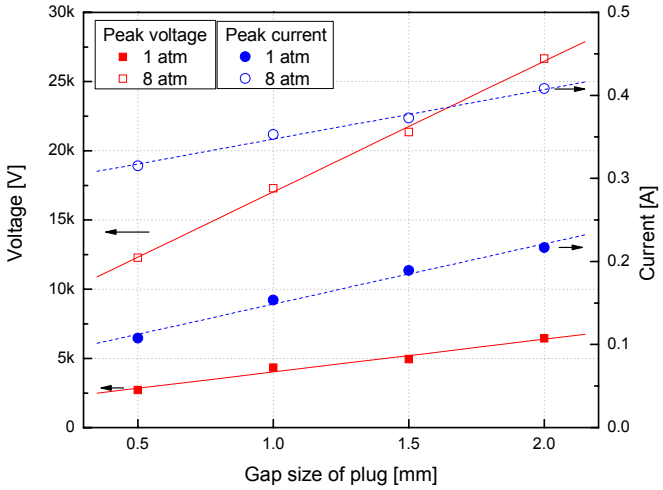

Figure 5. The effects of spark gap size on the peak voltage and current during breakdown.

2.1.B. *Effects of the Spark Gap Size*

The effects of electrode gap size on the discharge characteristics were investigated for spark gaps from 0.5–2.0 mm at pressures of 1 bar and 8 bar. A pressure of 8 bar was about as high as we could reliably produce a spark with a gap as large as 2.0 mm. The effects of the gap on the peak voltage and peak current during breakdown are shown in Figure 5. The data show that at both pressures, both the breakdown voltage and current (this peak is somewhat delayed and occurs shortly after the voltage peaks) increase approximately linearly with gap size. For an increase in spark gap size by a factor of 4, the breakdown voltage increased by a factor of 2.4 at a pressure of 1 bar, and 2.2 at 8 bar. Increases in peak current with gap size changing from 0.5-2.0 mm were smaller. Specifically, increasing the gap by a factor of 4 increased the peak current during breakdown by a factor of 2.0 at 1 bar but by only a factor of 1.3 at 8 bar.

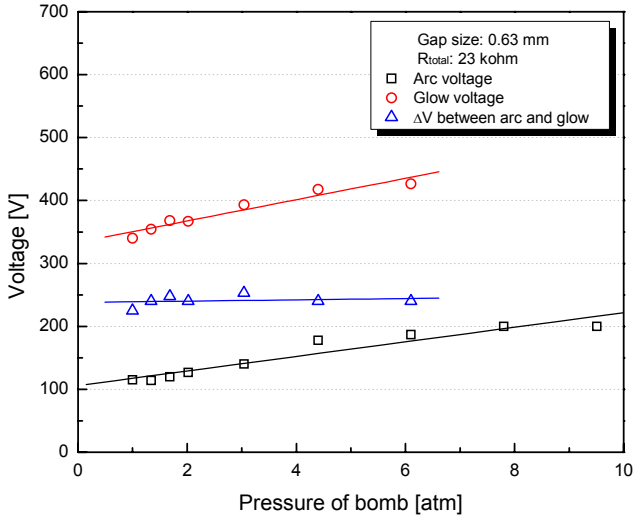

Figure 6 Effect of pressure on arc and glow voltage.

2.1.C. *Effects of Pressure*

Figure 6 shows the variation in arc and glow voltage levels as the pressure of the gas within the gap increases. A glow phase was only observed up to pressures of about 7 bar. Both arc and glow voltage increase approximately linearly with increasing pressure. Because of the linear dependence, the difference between the arc and glow voltages is constant, at ~240 V, over the pressure range that was examined.

The effect of pressure on the total energy delivered to the gap is shown in Figure 7. The total energy delivered to the gap was calculated by integrating the current and the voltage measured at the gap over the duration of the discharge. The total energy is seen to increase with increasing pressure, but not strongly. Total energy deposition increased from about 12.5 mJ at 1 bar to about 16 mJ at 18 bar.

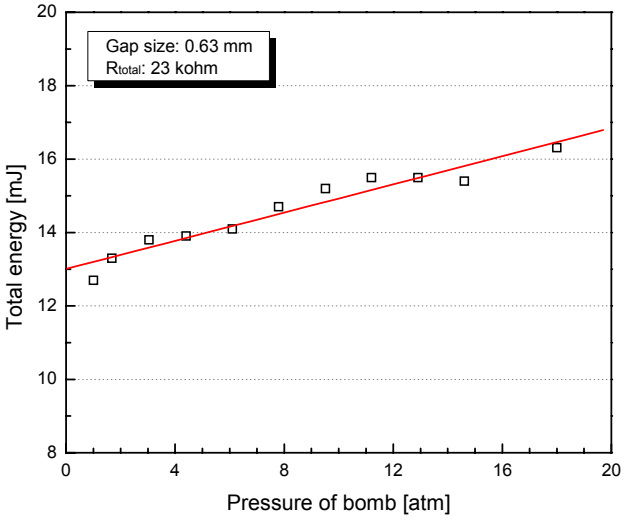

Figure 7. The effect of pressure on the total energy deposition at the spark gap.

It was also found that the fraction of the total discharge spent in the glow regime decreased while the fraction of time in the arc phase increased as the pressure increased as illustrated in Figure 8. At a pressure of 1 bar, about one-half of the total discharge time is in the glow phase. The time spent in glow decreases as the pressure increases until the glow phase is absent above a pressure of about 7 bar.

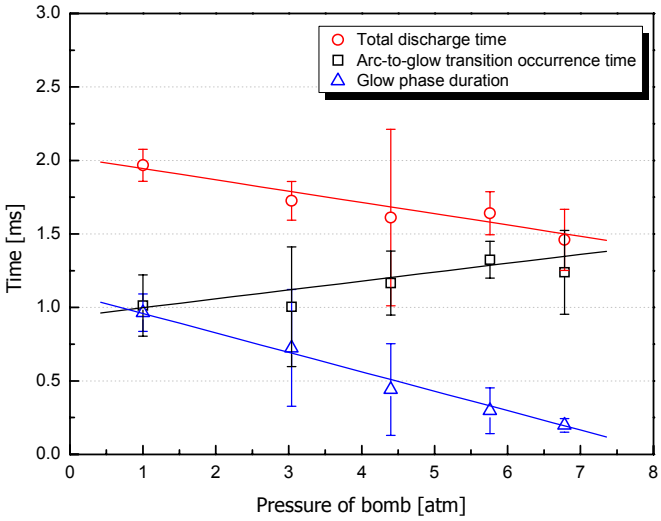

Figure 8. Effects of pressure on the time spent in the glow phase, the arc-to-glow transition time, and the total spark duration.

2.2. Railplug Design Studies

As discussed in Section 1, railplugs use a Lorentz force to move the plasma along the railplug rails. Fast plasma movement not only increases the ignitability but also improves railplug durability. Because the Lorentz force is strongly influenced by the current, a novel electronics system is used to fire the railplug. As shown in Figure 9, this system consists of a breakdown circuit and a "follow-on" circuit. The conventional breakdown circuit was a standard inductive ignition circuit that provided the high voltage required for breakdown and produced low currents (on the order of 100 mA). The follow-on circuit consists of a capacitor that was charged (in this case, using a Variac and bridge rectifier). This part of the circuit provides a high current (on the order of 100 A) after breakdown for accelerating the plasma down the rails. Isolation is necessary between the breakdown and follow-on segments. This isolation is achieved using a high-voltage diode D1 and a high-voltage blocking capacitor C1 between the ignition coil and follow-on circuit.

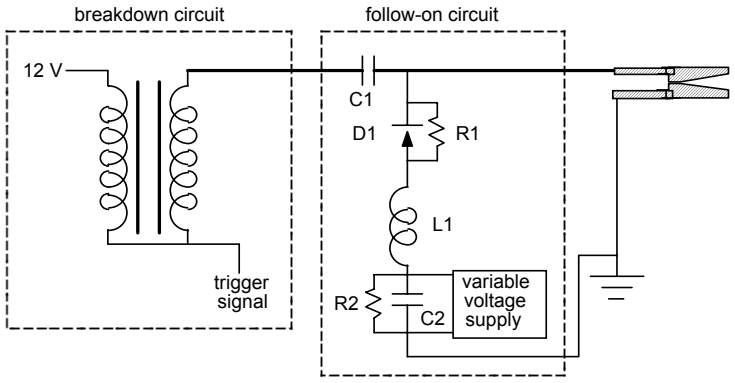

Figure 9. Schematic of the railplug electronic circuit.

It is well known that the energy stored in a charged capacitor (C2 in Figure 9) is ½ CV^2. Thus, changing the capacitance and charge voltage changes both the stored energy and the discharge energy delivered to the railplug. The discharge energy E_J was calculated by integrating discharge voltage and current:

$$E_j = \int Vidt \tag{4}$$

where V is the voltage measured at the railplug gap end. The capacitance values used in the present study ranged from 100 to 400 μF and charge voltages ranged from 100-200 V. The capacitor discharge circuit in Figure 9 can be simplified to represent a simple RC circuit. To study the effects of discharge duration on railplug performance, an adjustable power resistor with a full-scale resistance of 1 Ω was serially connected to the circuit just before the railplug to change the discharge time constant (not shown in Figure 9).

High-speed photography was used to study the effects of railplug parameters on arc movement. A framing rate of 50,000 f/s and a shutter speed of 1.1 μs were used. Plasma travel distance was obtained by processing the high-speed images, from which the plasma velocity was derived using the central difference approximation.

The railplug parameters that were examined can be categorized as those related to the electronics circuit and those that are related to the geometry of the railplug. These are the subjects of the following two subsections.

2.2.A. *Circuit Parameters*

The circuit parameters that were investigated included the inductance, polarity, and capacitance/charge voltage, as discussed below.

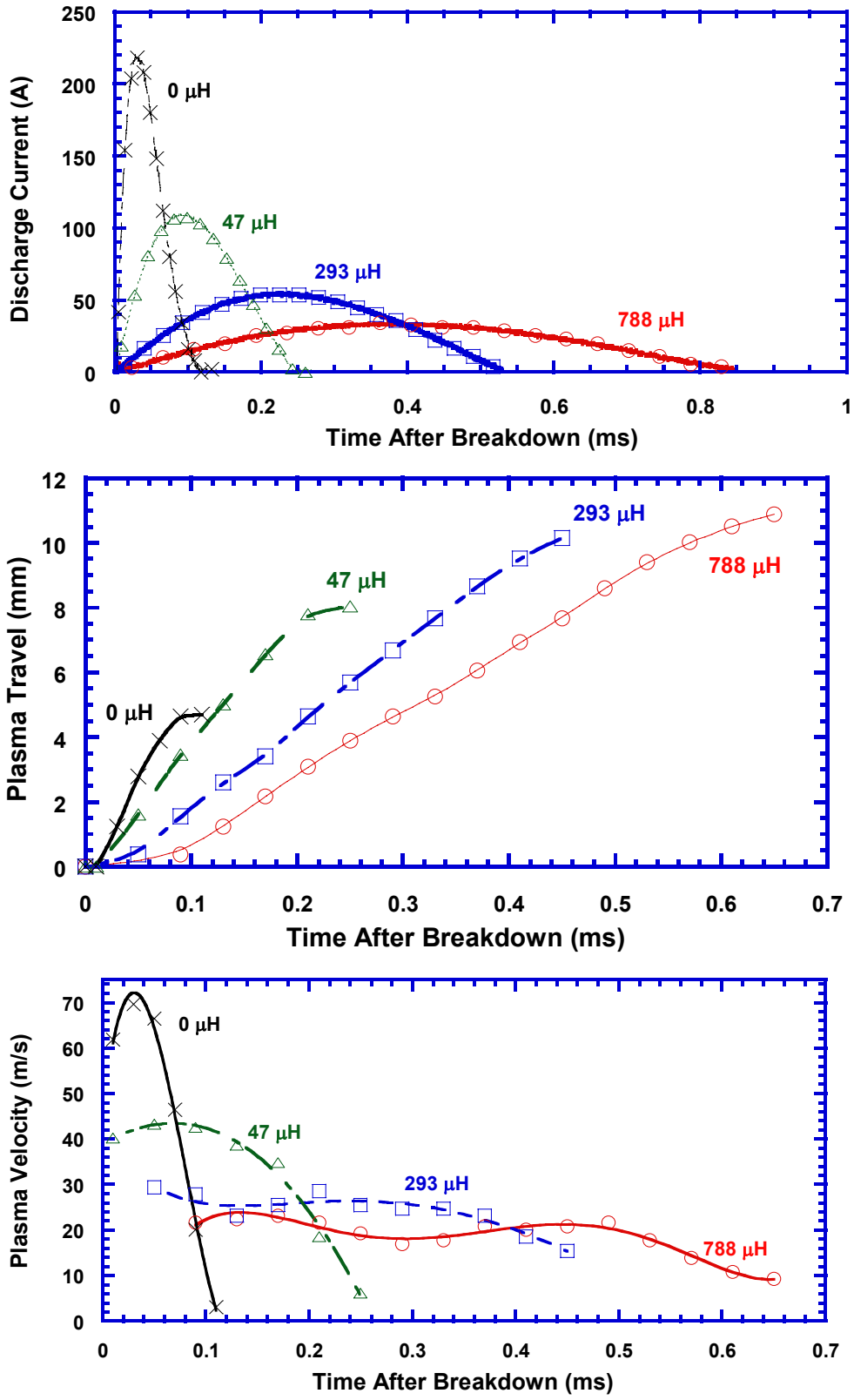

Figure 10. Effects of shaping inductor on discharge current, plasma travel distance, and plasma velocity for a magnet-enhanced railplug with a delivered energy E_d =0.7 J/shot.

Figure 10a shows that the peak discharge current decreases and the discharge duration increases as the inductance of the shaping inductor increases. Specifically, the discharge duration increases from 0.15 ms to 0.85 ms as the inductance increases from 0 to 788 μH. Additionally, as shown in Figure 10b, the plasma travel distance increases from 5 mm to 11 mm However, as shown in Figure 10c, the peak plasma velocity decreases from 70 m/s to 25 m/s as the inductance increases from 0 to 788 μH. From Equation 2, high current produces a high Lorentz force and, thereby, high acceleration, leading to a high peak velocity. On the other hand, plasma movement suffers because of high viscous forces that occur as the velocity increases. Therefore, increased inductance benefits plasma travel but penalizes arc velocity with the same discharge energy.

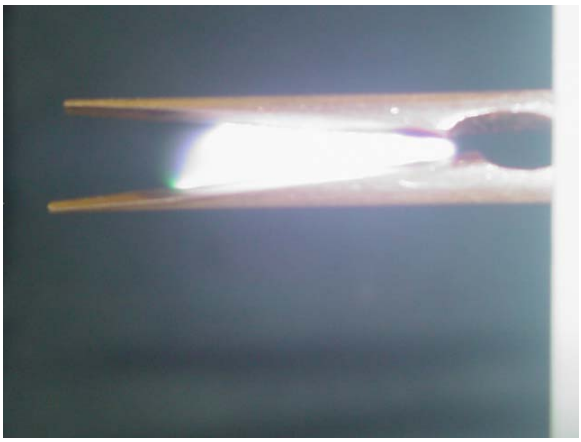

Bottom electrode grounded

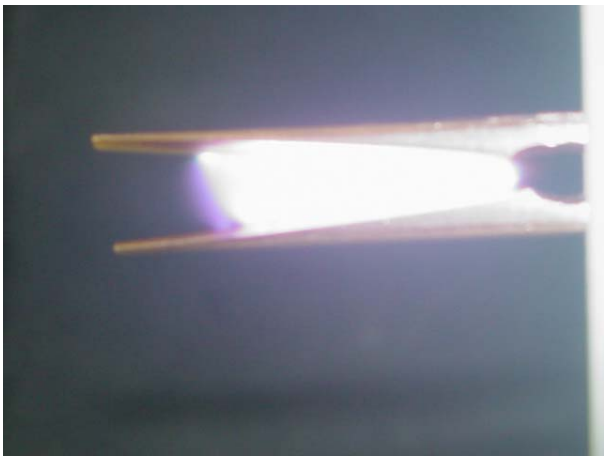

Top Electrode Grounded

Figure 11. Effect of electrical polarity on arc propagation.

An interesting effect of electrical polarity on arc propagation was observed. It was noticed (Figure 11) that the arc tended to propagate slightly further along the rail that was grounded. The reason for this difference in propagation distance is not understood, but may be a consequence of spatial variations in the strength of the induced magnetic field.

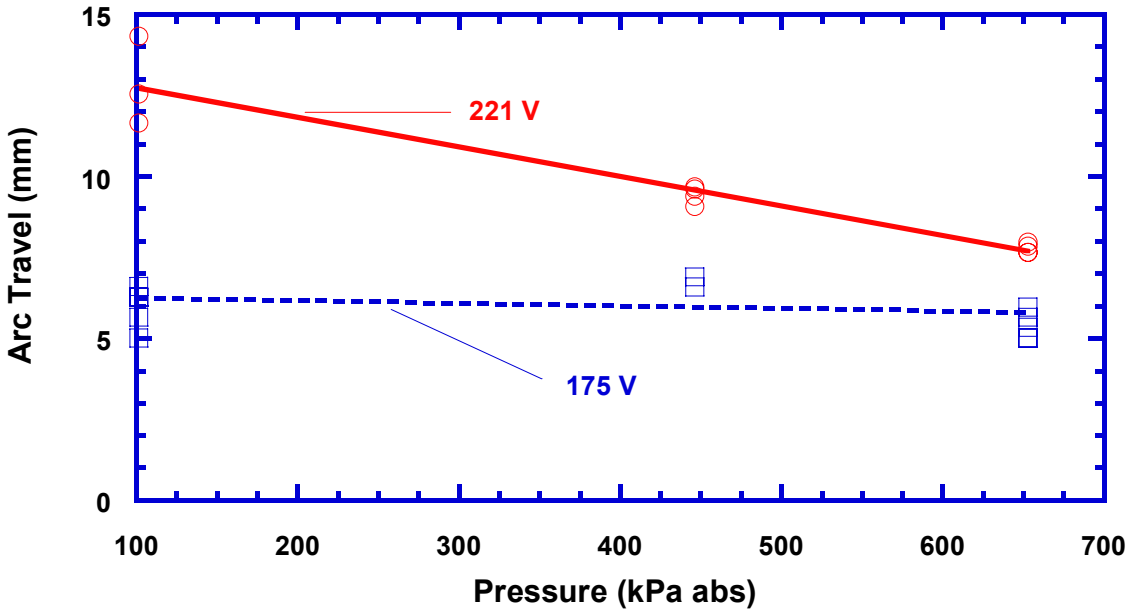

Figure 12. Arc travel versus pressure for a round cross-section parallel railplug for two different capacitor charge voltages.

The effect of charge voltage is illustrated in Figure 12 for a railplug with round electrodes, an initiation gap of 1.19 mm, and a divergence angle between the rails of 8^{O}. Arc travel is higher for the higher charge voltage. Because the capacitance was the same for the tests illustrated in Figure 12, the higher charge voltage also means higher stored and delivered energy.

The effects of delivered energy are shown in Figure 13 for the same railplug discussed with reference to Figure 12. Arc travel increases with increasing delivered energy, as expected.

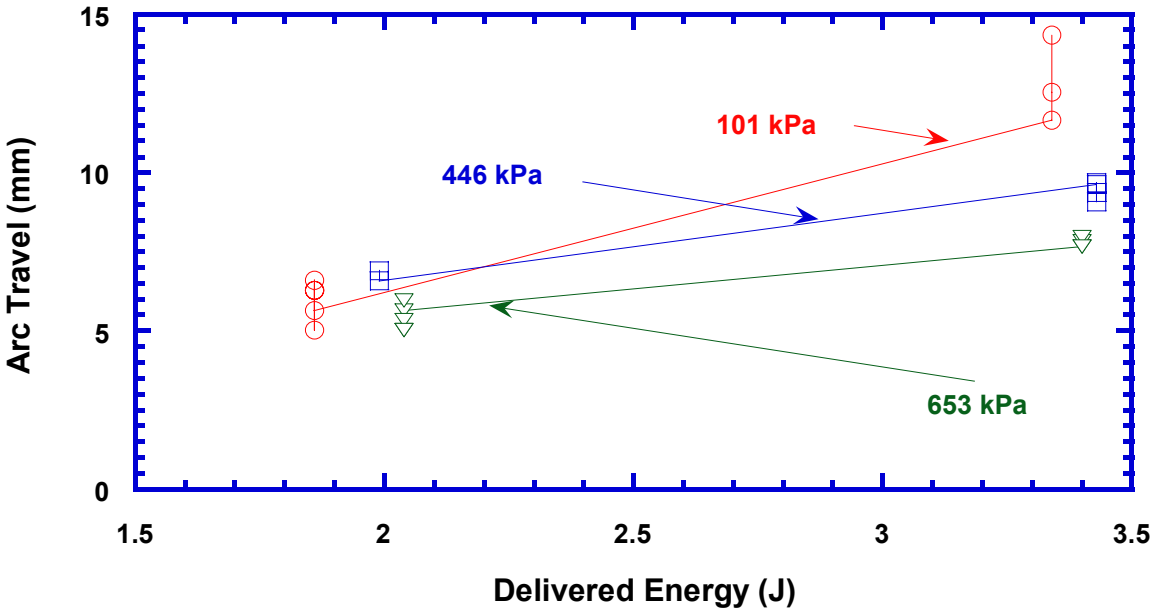

Figure 13. Effects of delivered energy on arc travel.

2.2.B. *Railplug Geometry*

The geometric factors that were studied include the angle between the rails, rail cross-sectional size and shape, rail divergence angle, initiation gap size, rail enclosure, and the addition of a permanent magnet to enhance the Lorentz force. Each of these factors is discussed below. Arc travel distance was measured as a function of pressure from 100 kPa to 1800 kPa for delivered energies from 0.5 to 3.4 J. The effect of an externally applied magnetic field on arc travel was also investigated.

In our previous study of railplugs, we focused on coaxial railplugs because the intended application was light-duty engines, which use 14 mm ignitors. In this case, parallel railplugs were impractical due to the limited cross-sectional area. However, parallel rails have a higher inductance gradient, which produces a larger Lorentz force. Thus, our present study has focused on parallel railplugs. For the coaxial railplugs, the outer rail had an "initiation gap", which was an area where the rails were closely spaced to ensure that the spark jumped the gap near the breech of the rails. There was a sharp discontinuity at the outlet end of the initiation gap. Because the inductance gradient increases strongly across this discontinuity, we expected that the arc would move completely down the rails. This discontinuity is illustrated, for a parallel railplug, in Figure 14. We discovered that, in fact, the arc hung up at the discontinuity. Elimination of the sharp transition between the initiation gap and the rails greatly increased arc travel distance. The gradual transition is shown in Figure 15. Here, it is still essential to force the arc to jump the gap near the breech end of the railplug; otherwise the arc has nowhere to propagate. Thus, a taper angle between the rails is required, as illustrated in Figure 15.

.

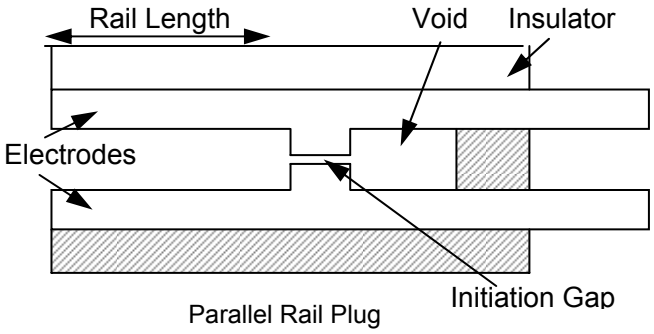

Figure 14. Schematic of original geometry of parallel electrode railplugs.

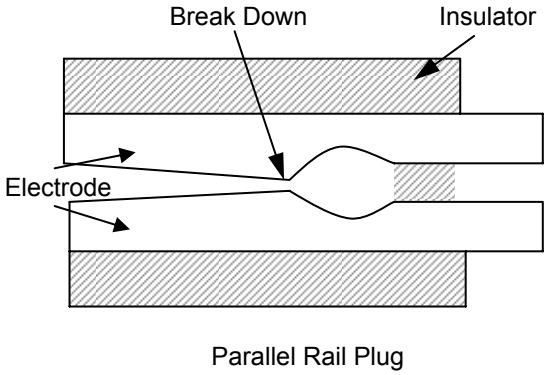

Figure 15. Schematic of a parallel electrode railplug having tapered rails.

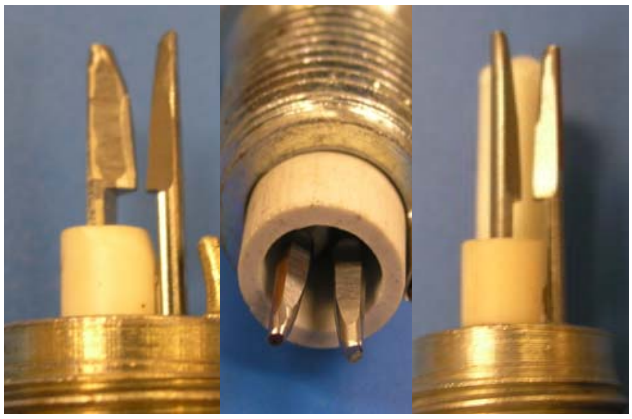

Figure 16. Examples of railplugs: A: open rails; B: partially enclosed rails; C: magnet enhanced railplug.

Figure 16 shows three parallel railplugs that were tested in this study. Railplug A is an open rail "parallel" railplug. As seen from these pictures, the rails were tapered to remove the gap area discontinuity that caused wear and performance problems during an earlier railplug study. The taper from a small rail spacing at the breech (initiation) end (to allow for a

reasonable breakdown voltage) to a larger rail spacing (which produces a larger inductance gradient and thus a larger Lorentz force) helps the arc to move rapidly away from the upstream (initiation) region of the initiation gap. The rails were also machined to form ridges along the center-plane such that a muzzle end view has a shape similar to a slice of pie. The plasma streamer along the ridged rails is thinner and more concentrated so it has higher density and lower heat loss, which promotes arc movement. That is, the fast arc motion along ridged rails results in decreased rail wear compared to round rails. The only difference between railplugs B and A is that the rails in B are partially enclosed. The arc moves farther for the partially enclosed rails than for the open rails because thermal expansion aids arc motion. Railplug C is the same as A except C uses a small permanent magnet (Alnico 8) to aid arc motion. The magnet is held in a ceramic tube behind the rails in Figure 16. The magnetic strength at the rail surface is about 4.5 Gauss when no current flows through the railplug. As seen from Equation 1, increasing the local magnetic field strength B can effectively increase the Lorentz force F, resulting in higher arc velocity.

2.2.B.1. Effects of Rail Cross-Sectional Size and Shape

Figure 17 shows the effects of electrode cross-sectional size on the distance the plasma travels and on the arc velocity. As the electrode diameter decreases, plasma velocity increases and the arc moves further. It can be seen from Equation 3 that the inductance gradient of the railplug is a function of electrode size. A simple calculation can be used to show that the inductance gradient L' increases about 20 percent as the electrode diameter decreases from 3.2 mm to 1.5 mm if all other dimensions remain unchanged. Thinner electrodes also decrease the plasma heat losses, which benefits plasma motion.

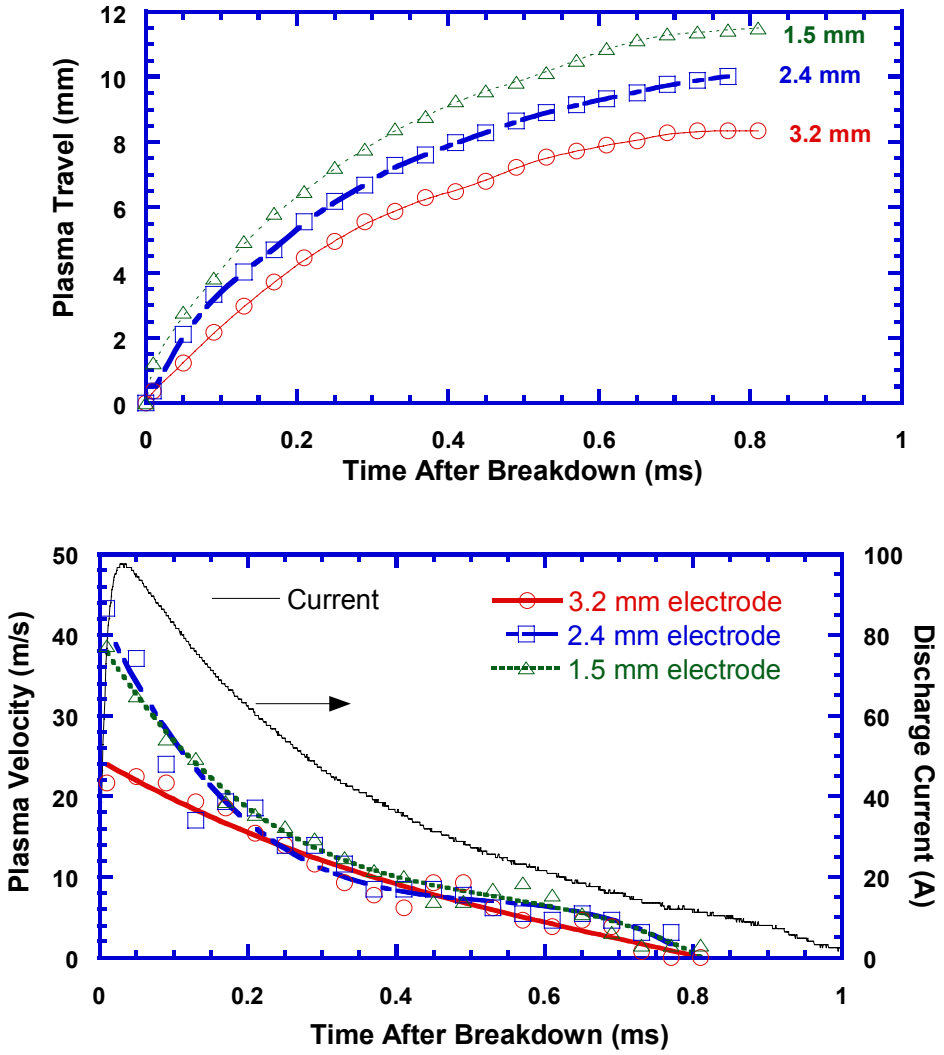

Figure 17. Effects of electrode size on plasma travel distance and velocity (non-magnet enhanced railplugs with a delivered energy of 1.5 J/shot and a duration of 1 ms).

Railplugs having four cross-sectional shape combinations were studied: flat rails, ridged rails, round rails, and a combination of one round and one ridged rail. The rail cross-sectional shapes are shown in Figure 18. For all of the railplugs, the rail material was copper. Copper was chosen because of its high electrical conductivity and ease of machining. The diameter of the copper rod from which the railplugs were constructed was 0.318 cm (0.125 in.). The rail length from the initiation gap to the muzzle end was between 2.3 and 2.8 cm for most of the railplugs. The rails were held in place by inserting them into holes drilled through a machinable ceramic (Macor) block that provided electrical insulation. Except where noted, the rails were unenclosed, eliminating thermodynamic expansion effects that might enhance arc movement.

Different rail cross-sectional geometries were studied because of the arc behavior that we observed using the flat electrode geometry, which was the first geometry we examined. We observed that the arc, rather than traveling along the rail axis or centerline would, instead, travel along the outer edge of the rails, traveling along one side or the other. This was

believed to happen because the electric field tends to concentrate along sharp edges. It is not clear that this is bad and may enhance rail durability by spreading the arc over more surface area; however, it did result in a shorter arc propagation distance.

In an attempt to keep the arc along the rail centerline, the ridged geometry was conceived. This geometry did indeed produce arc propagation along the ridge down the centerline of the railplug. In addition the arc propagation distance was greater since the arc did not spill out of the sides of the railplug. After this discovery, the flat geometry was no longer investigated. While the ridged electrodes were successful at keeping the arc along the rail axis it took time to machine this design, so railplugs having a circular cross-section, that required no machining, were also studied. While the circular cross-section railplugs had no sharp edges to concentrate the electric field they also tended to generate an arc that propagated along either side of the rails rather than down the rail axis where the rail separation was a minimum. The reason for this behavior is uncertain, but it is thought that viscous forces may retard the arc along the rail axis making propagation easier away from the axis where the plasma is less confined.

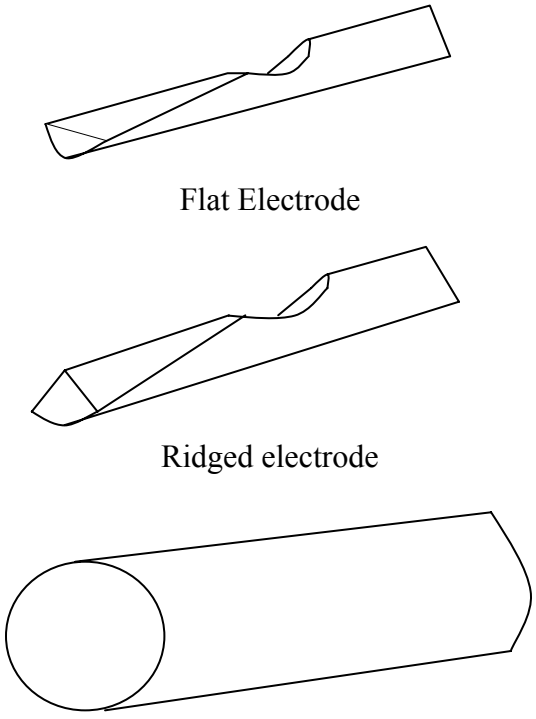

Figure 18. Views of the three rail cross-sectional geometries studied.

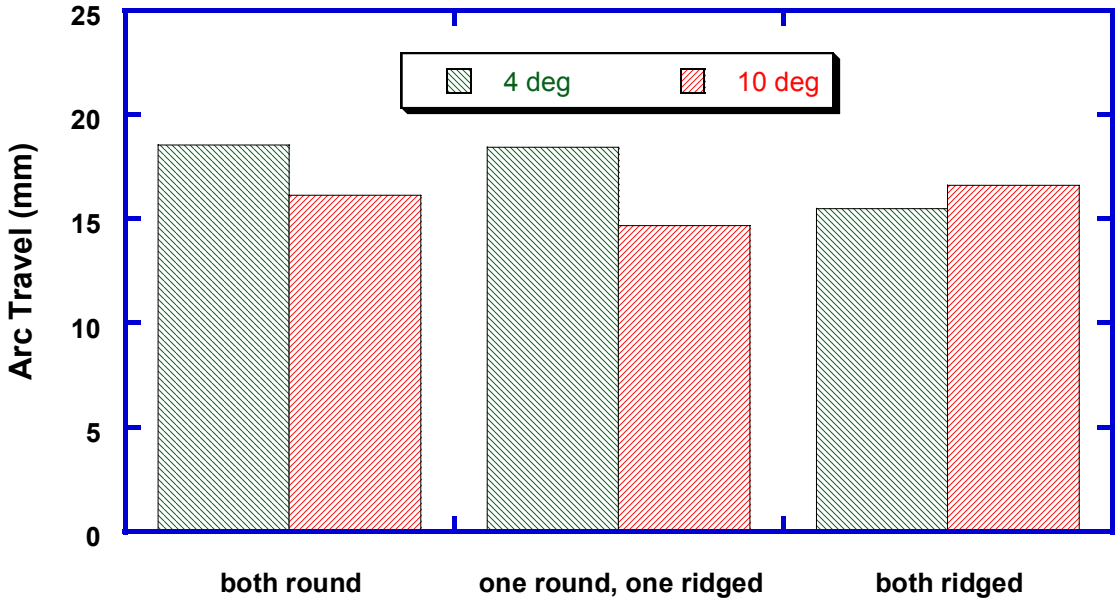

Figure 19. Effect of electrode shape on arc travel.

Figure 19 illustrates the effect of electrode shape on arc travel for two divergence angles between the rails. With a 4^{o} angle, having ridges on both rails produces the shortest arc travel while having both electrodes round produces essentially the same arc travel as a railplug with one round electrode and the other ridged. However, with a 10^{o} angle, having ridges along both rails produces the greatest arc travel, although it is only slightly better than the railplug with both electrodes having a circular cross-section.

The effects of divergence angle are explored in more detail in the following subsection.

2.2.B.2. Effects of Rail Divergence Angle

The arc travel distance tends to decrease gradually with increasing rail divergence angle. Figure 20 shows a sequence of images captured using high-speed Schlieren that shows the arc propagation. In these images the distance from the initiation gap to the end of the rails is about 25 mm.

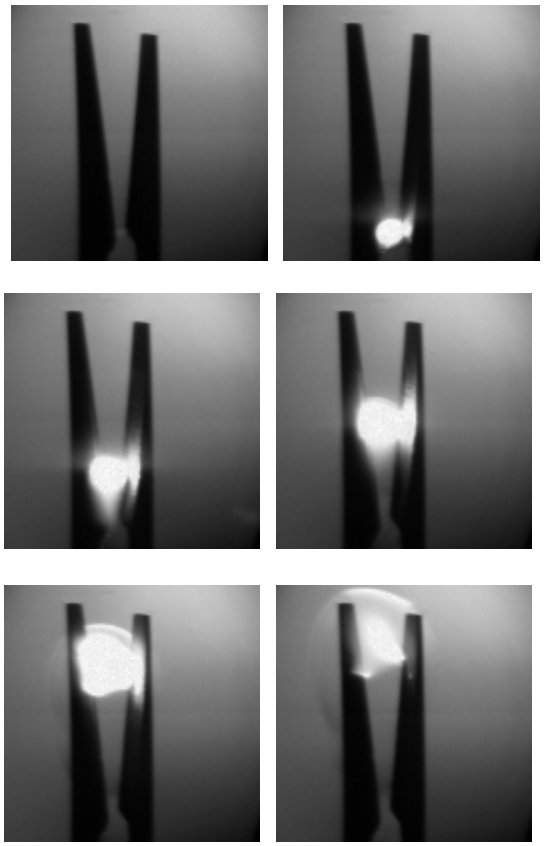

Figure 20. High speed Schlieren images of arc propagation along a ridged cross-section railplug, 0, 15, 189, 454, 1088, and 1842 μs after breakdown, respectively.

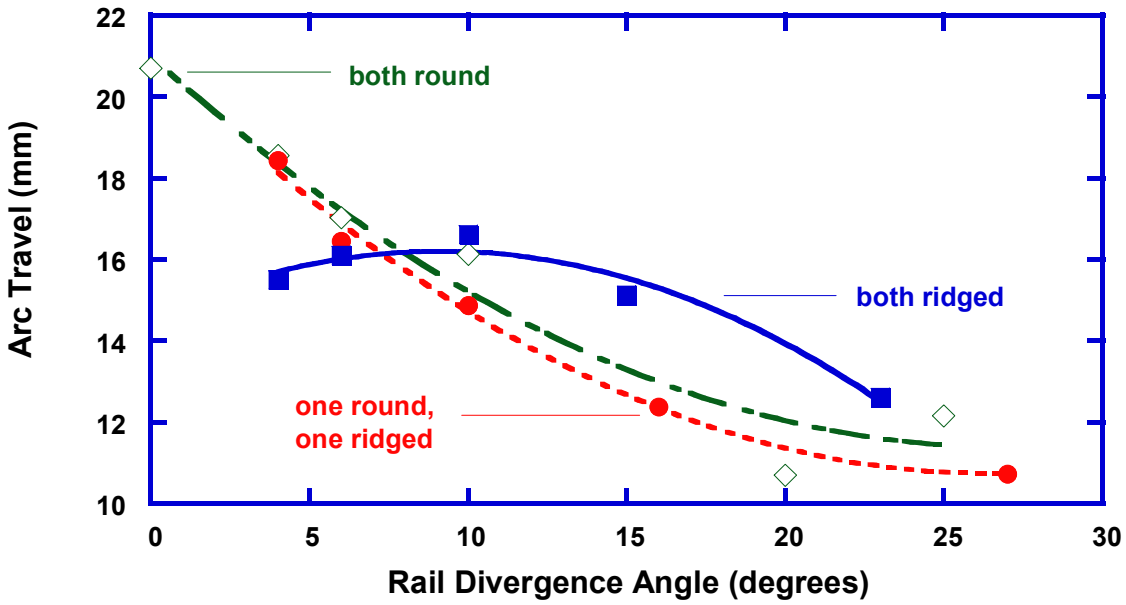

Figure 21. Effect of rail divergence angle on arc travel for three rail shapes.

The data presented in Figure 21 were taken at a pressure of 1 bar with a delivered energy of 3.4 J. At this energy level there is substantial movement of the arc from the initiation point (a gap of 1.07 mm) for all three rail geometries. The arc travel distances were measured from time-integrated digital images of the discharge, and each data point shown is an average of 4 to 7 shots taken at each condition. These large arc movements are in contrast to the short travel associated with railplugs having the older rail designs with a sharp transition from the initiation gap to the rail.

In general, arc propagation distance tends to decrease as the rail divergence angle is increased. For the ridged geometry railplug, however, a slight increase in rail propagation distance was observed with increasing angle for small angles. It can be seen that for the three different rail cross-sectional combinations studied, the arc travel distance was not greatly different; all were about 15 mm with a 10^{o} divergence angle.

2.2.B.3. Effects of Initiation Gap Size

The effect of distance across the initiation point (gap) on arc propagation distance was one of the parameters studied. Spark plug gaps in large bore natural gas engines are often as small as 0.4 mm to keep breakdown voltages low enough to avoid spark leakage. We found that very small initiation gaps and rail spacing inhibit arc movement. For railplugs with both rails having a circular cross-section and 3.4 J of delivered energy, arc movement was inhibited for a gap of 0.46 mm but, for gaps in the range of about 1.0 mm to 1.3 mm, arc movement was essentially independent of initiation gap size.

2.2.B.4. Effects of Rail Enclosure

We also investigated the effect of rail enclosure on arc travel distance. We found that, in some cases, arc movement was reduced by enclosing the rails of the railplug. One of the railplugs was studied with different degrees of enclosure to examine whether thermodynamic expansion of the gases within the railplug would enhance the velocity of the arc and the distance that it traveled down the rails. Time-integrated images of the arc travel were used to assess the effects.

These images are shown in Figure 22. A railplug was used with a delivered energy of 3.4 J. Figure 22a shows the discharge of the railplug when fully enclosed between two flat glass plates. Figure 22b is with the railplug fully enclosed within a circular cross-section glass tube. In Figure 22c, only a short portion at the rear of the plug is contained in a section of glass tube. The unconfined railplug was tested, but is not shown. We were surprised by the results that showed the arc travel distance was greater for the unconfined railplug than for either of the two fully confined configurations. The arc travel distance for the partially confined configuration was slightly greater than the unconfined configuration.

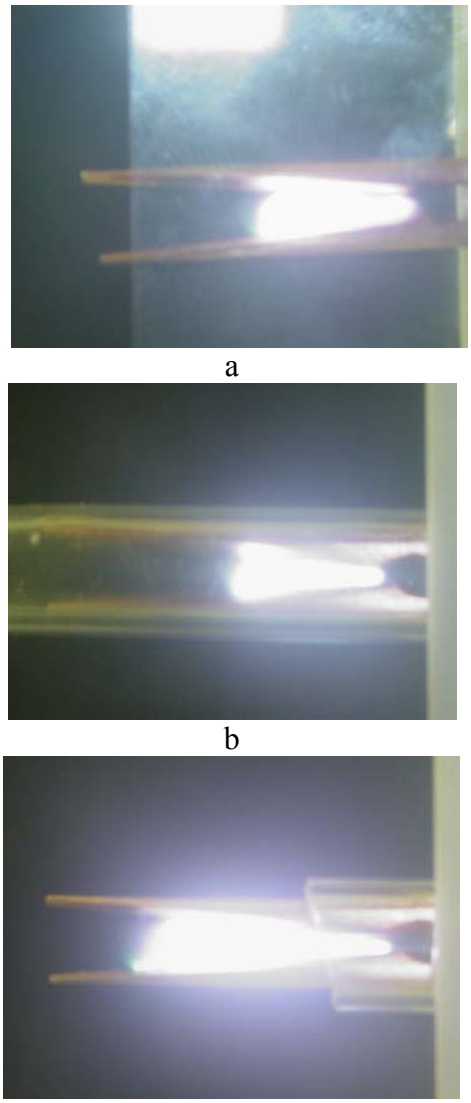

Figure 22. Effect of railplug enclosure on arc propagation, flat railplug, high energy a) fully enclosed between flat glass. b) fully enclosed within tube, c) partially enclosed in tube.

The mean arc travel distances for the different configurations were 11 mm for the two fully enclosed railplugs, 19 mm for the partially enclosed railplug, and 16 mm for the unenclosed railplug. These results were very puzzling initially. The process was investigated using a numerical model for railplug discharge developed within our research group. The results of the numerical model suggested that for the fully confined configurations the plasma created by the arc maintains its high temperature longer, maintaining its electrical conductivity longer. The result is a larger conducting volume of gas that decreases the arc current density which significantly reduces the strength of the induced magnetic field. If this is correct it suggests that the partially confined configuration allows more rapid cooling of the current conducting channel.

2.2.B.5. Effects of an External Permanent Magnet

As discussed above, increasing the local magnetic field strength B can effectively increase the Lorentz force F, resulting in higher arc velocity and a longer plasma travel distance. This effect is reflected in the experimental data shown in Figure 23, which compares the performance of two railplugs, one with and one without a permanent magnet to increase the Lorentz force. In the magnetically-enhanced cases a 30 mm X 20 mm rectangular magnet was located along one side of the railplug at a distance of 4 mm from one of the rails. At this distance the magnet had a measured field strength of 90 Gauss.

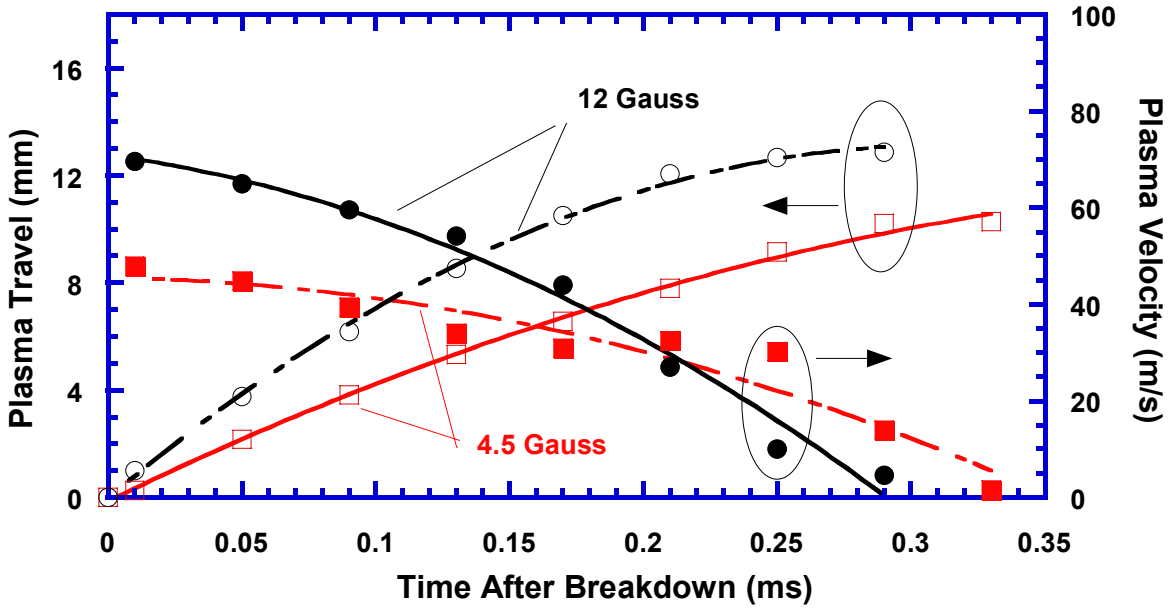

Figure 23. Effects of permanent magnet strength on plasma travel distance and velocity. Delivered energy E_d =0.7 J/shot and duration = 0.5 ms.

Additional results showing arc travel distance versus pressure for different levels of energy and with and without the use of a permanent magnet to enhance the local magnetic field are shown in Figure 24.

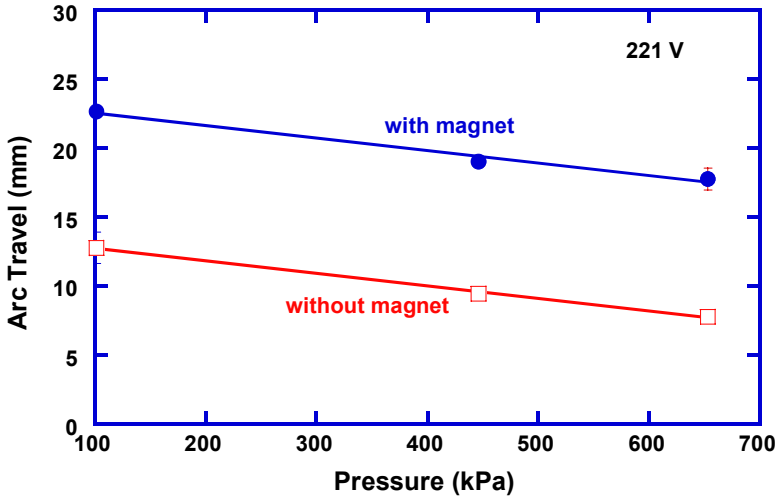

a

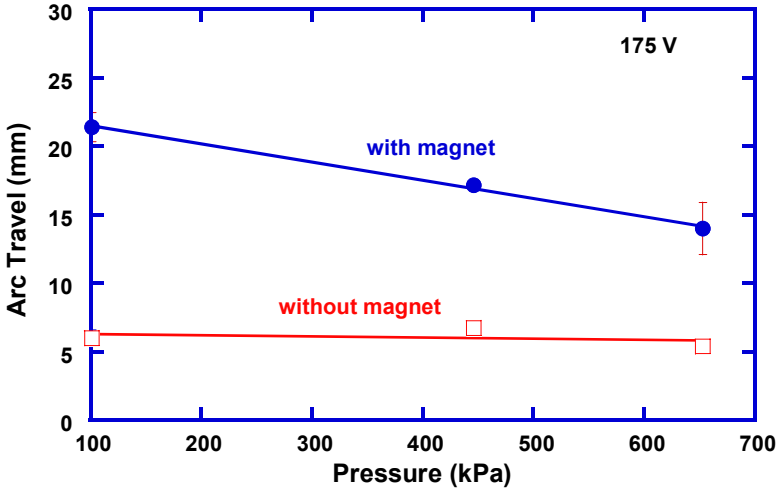

b

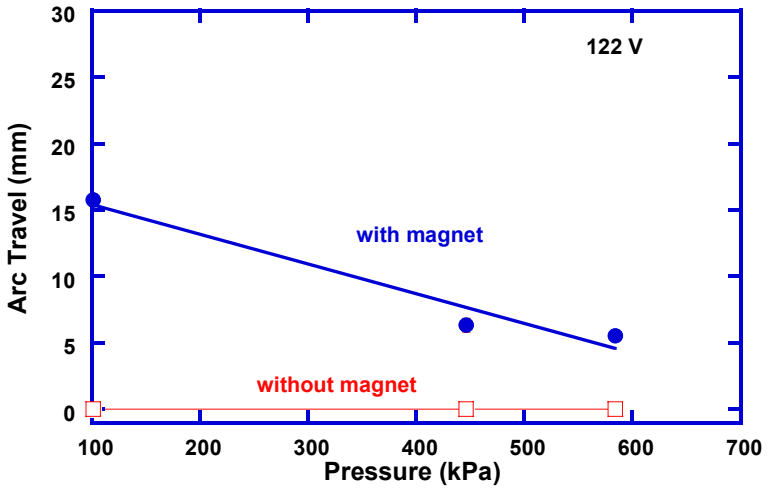

c

Figure 24. Arc distance versus pressure for a round cross-section railplug, with and without magnetic assist, gap size of 1.19 mm, angle of 8°, for capacitor charge a) 221 Volts, b) 175 Volts, c) 122 Volts.

Figure 24a displays the high energy results with a capacitor charge voltage of 221 V. This corresponded to a delivered energy of about 3.4 J. The delivered energy was slightly different with and without the magnet. Figure 24 shows that, without the magnetic assist, the arc travel distance decreases with increasing pressure from about 13 mm at 100 kPa pressure to about 7 mm at a pressure of about 650 kPa. The enhancement in arc travel by the permanent magnet is evident. With the magnet the arc traveled 23 mm at ~1 bar pressure, dropping to about 18 mm at a pressure 450 kPa, and still traveling about 17 mm at a pressure of 650 kPa.

For the medium energy case with a capacitor charge voltage of 175 V (about 1.8 – 2.0 J) the arc movement with the magnet was only slightly less than at the higher energy. However, the arc movement without the magnet was about half the distance as at the higher energy (Figure 24b)

For the low energy case (Figure 24c) the capacitor charge voltage was 122 V (about 0.4 – 0.8 J). For this case there was negligible arc movement without the magnet over the entire pressure range. With the magnet, however, the arc travel was 15 mm at 100 kPa and about 5 mm at a pressure of 600 kPa.

The important conclusion from these results is that, with a magnetic assist, a railplug can have significant arc movement at high pressure even for relatively low delivered energies.

2.2.C. *Future Work on Railplug and Circuit Design*

We are currently working on quantifying rail erosion so that we can assess the durability of our railplugs for various operating conditions. We are adapting a profilometer used for surface roughness measurements to measure the surface profile of railplug rail when new and after use. This comparison will allow us to quantify how much metal has been eroded way along a rail surface and how the contour of the rail as changed, but along the axis of the rail and perpendicular to the rail axis.

2.3. Engine Tests and Results

Because the University of Texas does not own a large bore natural gas engine, or a dyno large enough to test one, we tested a 4-cylinder, 2-valve gasoline engine that was modified to operate on natural gas. Table 1 provides the important engine parameters. Natural gas was provided from a 20.6 MPa (3,000 psig) natural gas tank through a high-pressure regulator, a low-pressure regulator, and a mixer. Cylinder 4 was instrumented to assess the performance of railplugs and spark plugs. The original engine used 14 mm spark plugs, so the spark plug hole for this cylinder was machined to accept 18 mm ignitors due to the present interest in large bore engines.

The engine was connected to a Super Flow SF-901 water-brake dynamometer. The ignition timing was controlled via a Motec M4 programmable engine controller.

A Kistler quartz piezoelectric pressure transducer (model 603B1) was installed in cylinder 4 to acquire cylinder pressure data. A Kistler model 5010 charge amplifier was used to condition the pressure signal. Potential pressure transducer signal drift was compensated for in software by referencing ("pegging") to the known intake manifold pressure at BDC near the end of the intake process.

Table 1. Engine Parameters.

No. of cylinders	4
Displacement	2.2 liter
Bore	89 mm
Stroke	88 mm
Compression ratio	8.85
Test speed	1200 rpm

The cylinder pressure data were acquired using a DSP Technology combustion event analyzer with DSPT model 4325 real time processor. This data acquisition system allowed automatic determination of the indicated mean effective pressure (IMEP), location of peak pressure (LPP), mass burned fraction profiles, percent misfiring cycles, and coefficient of variability (the standard deviation normalized by the mean) of the IMEP (COV of IMEP). The COV of IMEP is routinely used as a measure of cyclic variability or combustion stability. All results were averaged over 500 cycles.

For each experiment, the air/fuel ratio was determined from the exhaust gas using a Horiba wide-range lambda sensor (Model LD-700). The output from this instrument was automatically logged by the DSP data acquisition system and averages were taken over the same 500 cycles as were the other data.

All the engine data in this report were acquired at wide open throttle (WOT). The ignition timing was set to MBT (minimum advance for best torque) since the best combustion stability (minimum COV of IMEP) generally takes place at MBT spark timing (Ozdor et al., 1994).

Figure 25 shows the effects of the equivalence ratio, ignition energy, and spark duration on the COV of IMEP for a spark plug. A conventional spark plug (Champion RF14LC) with a 1.0 mm (0.040'') gap was tested with both a conventional ignition system and the higher energy from the railplug circuit. The LSL (lean stability limit; the fuel/air equivalence ratio at which the COV of IMEP = 10%) of the spark plug with a conventional ignition system was $\phi = 0.63$, whereas the spark plug with a delivered energy of 0.7 J/shot extends the LSL to ~0.59. For light-duty SI engines, this baseline LSL for spark plugs is typical. As one example, Edwards and coworkers (1983) tested two spark plugs in a CFR engine operating on propane. At test conditions of 1000 rpm, 8:1 CR, MBT timing, and WOT, they found that the LSL of the Champion D-16 spark plug was ϕ=0.69 while the Motorcraft λGP22 extended electrode spark plug (with a 9.14 mm penetration of the electrodes into the combustion chamber) with a spark gap of 1.27 mm produced a Lean Stability Limit of $\phi = 0.64$. Similarly, using certification gasoline Zheng and coworkers (1993) found an LSL of $\phi = 0.66$ at 1300 rpm and 390 kPa IMEP with a Champion N12YC with a 0.9 mm (0.035'') gap and $\phi = 0.62$ with a 1.8 mm (0.070'') gap. Additionally, as illustrated in Figure 25, increasing the delivered energy from the typical 0.02 J/shot up to 0.7 J/shot extends the LSL but not much. The overall ignition performance for lean mixtures improved as the spark duration increased.

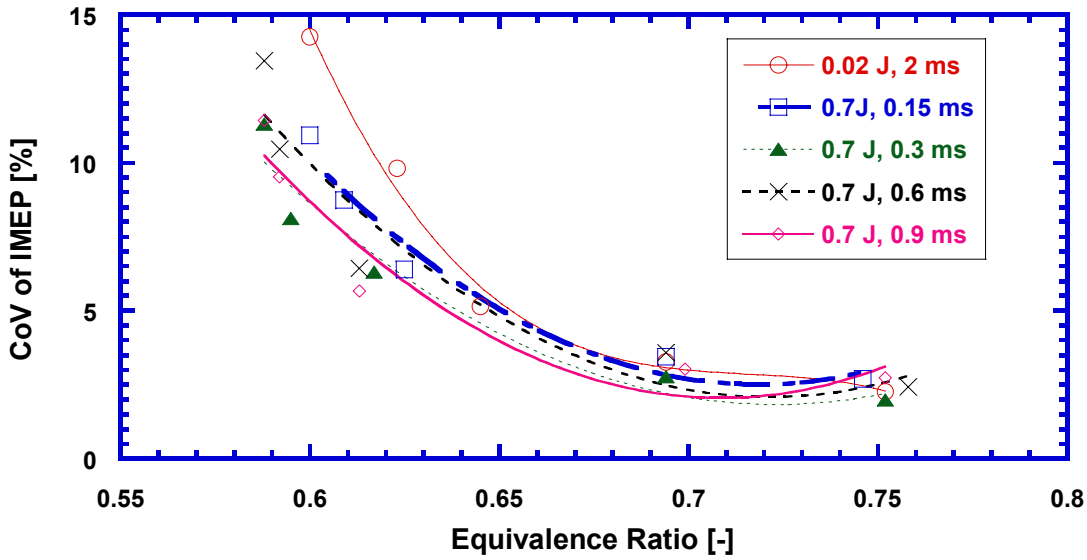

Figure 25. Effects of the equivalence ratio on the combustion stability for a spark plug (1200 rpm, WOT, MBT timing).

Figure 26 provides the mass fraction burned histories, depicting three of the phases of combustion (kernel formation: 0-2% burned; early flame growth: 2-10% burned; and fully-developed turbulent combustion: 10-90% burned). The duration of combustion is normally defined as the crank angle interval for 0-90% burned. The spark plug with 0.7 J of energy had a shorter duration of combustion, and an especially short kernel formation phase, compared to the spark plug with 0.02 J.

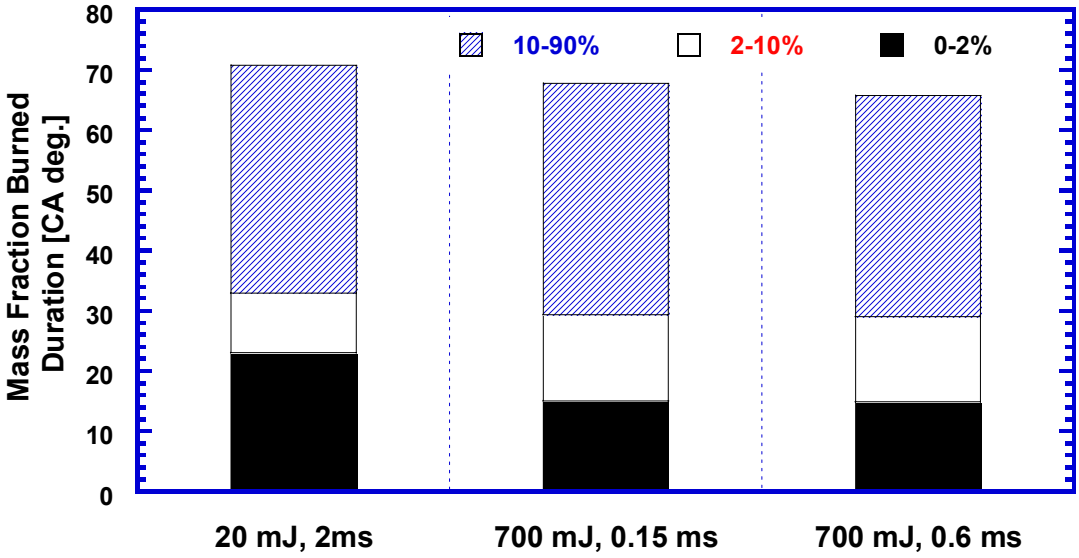

Figure 26. Effects of discharge energy and duration on the mass burning rates for a conventional spark plug operating at WOT, MBT, and $\phi = 0.69$.

Figure 27 shows the effect of spark duration on the performance of a railplug. It shares very similar trends with the spark plug. Specifically, the ignition performance improves as the spark duration increases because a longer discharge duration benefits plasma motion, as discussed previously. For the same discharge energy as the spark plug, the railplug extends the LSL from $\phi = 0.59$ to 0.54. The high-speed arc motion results in a fast burning rate and the ability to burn leaner mixtures than might ordinarily be possible. This also can be seen in Figures 28 and 29. The LSL was extended to as low as $\phi = 0.53$. As the mixture becomes leaner, this trend becomes more obvious, as shown in Figure 30. It must be noted that as the mixture became leaner, it became harder to quantify the duration of the 0-2% mass burned fraction accurately. One of the reasons was that ignition noise became stronger since the breakdown voltage increased for leaner mixtures. Therefore, no 0-2% mass burned fractions are shown in Figure 30.

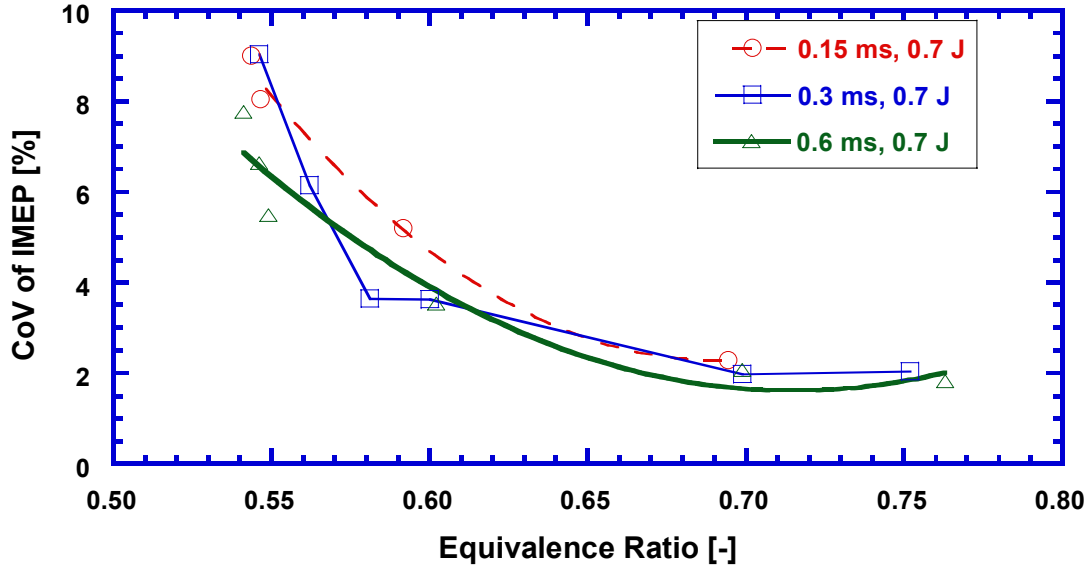

Figure 27. Effects of the spark duration on the combustion stability for the magnet-enhanced railplug.

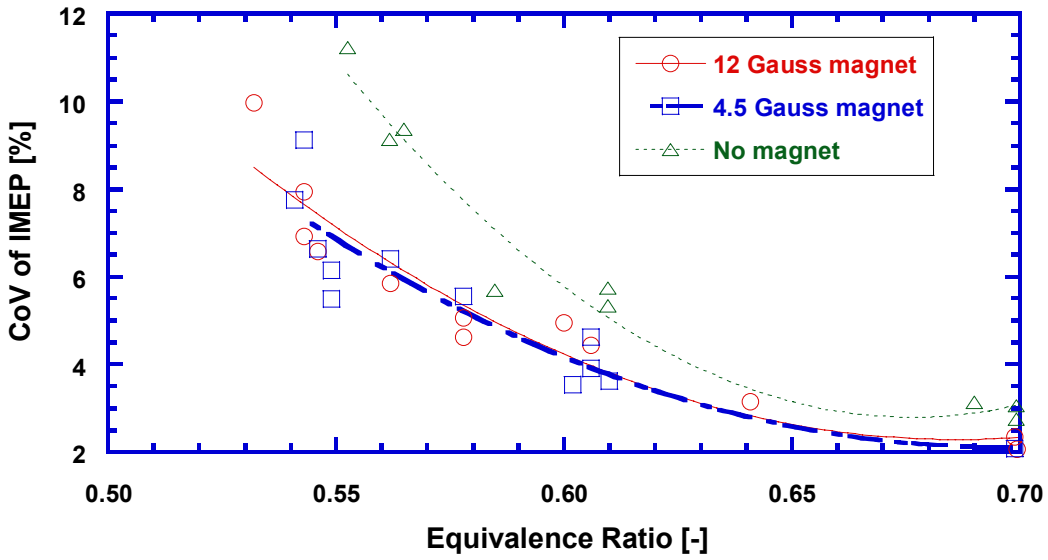

Figure 28. Effects of magnetic strength on railplug performance for a delivered energy of 0.7 J/shot with a spark duration of 0.6 ms.

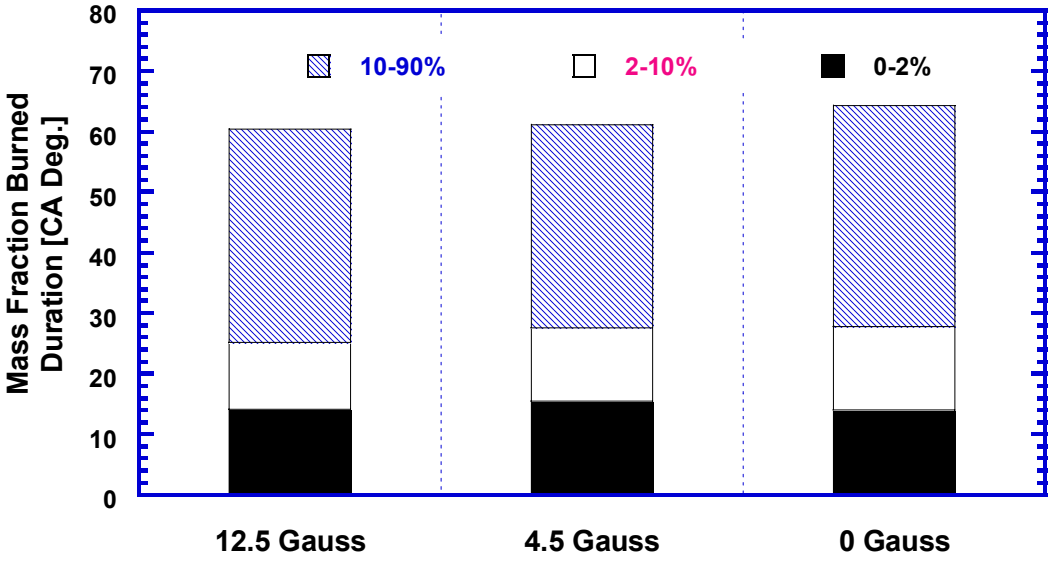

Figure 29. Effects of magnetic strength on railplug mass burning rates for a delivered energy of 0.7 J/shot, a spark duration of 0.6 ms, and ϕ=0.69.

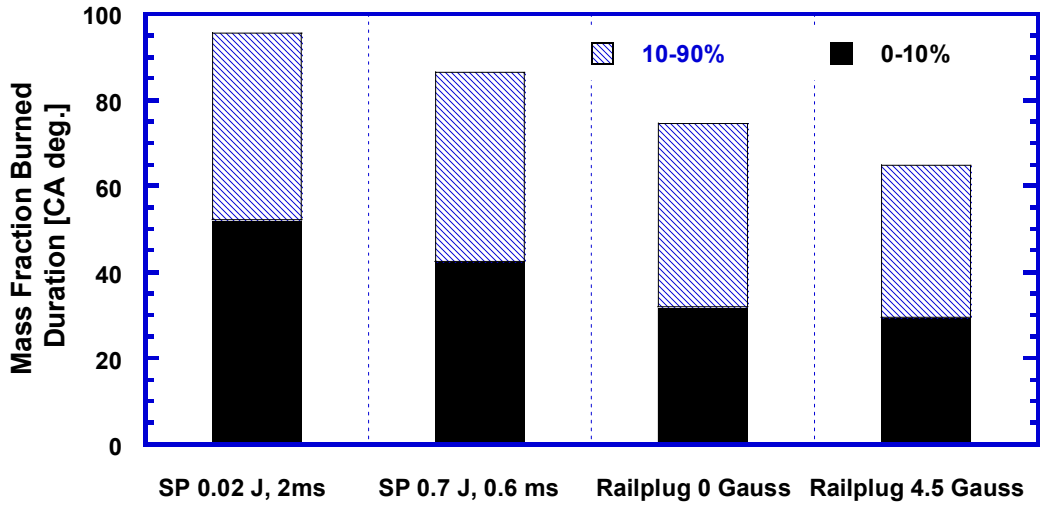

Figure 30. Comparison of the mass burning rates for spark plugs and railplugs at ϕ=0.61 (for the railplugs, discharge energy of 0.7 J/shot and duration 0.6 ms; SP=spark plug).

The results of repeatability tests are shown in Figure 31. Four tests were run on different days using the same magnet-enhanced railplug. It can be seen that the results are quite reproducible.

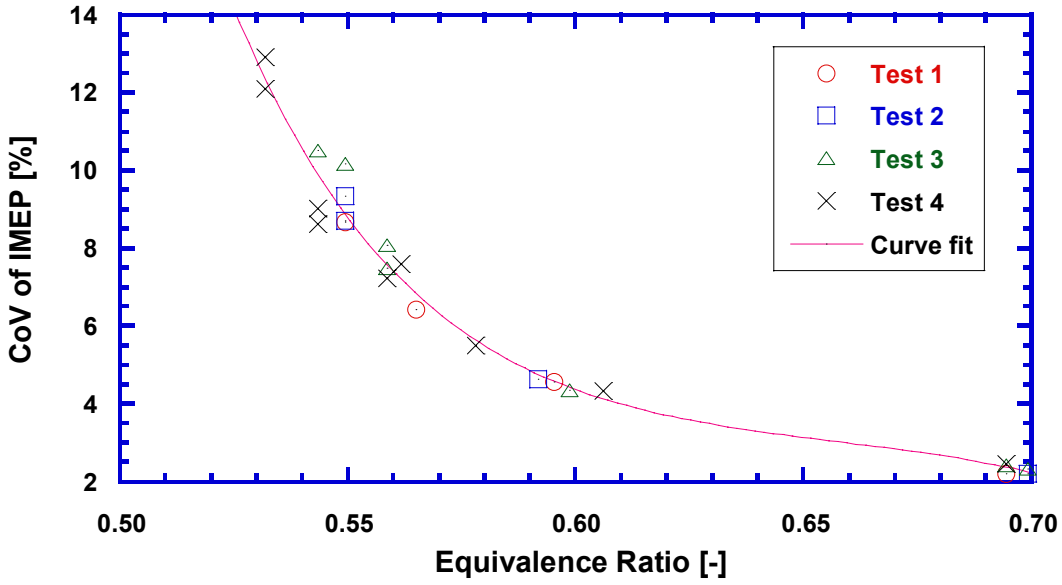

Figure 31. Results from the railplug repeatability tests (magnet-enhanced railplug with a discharge energy of 1.5 J/shot and a discharge duration of 0.8 ms.

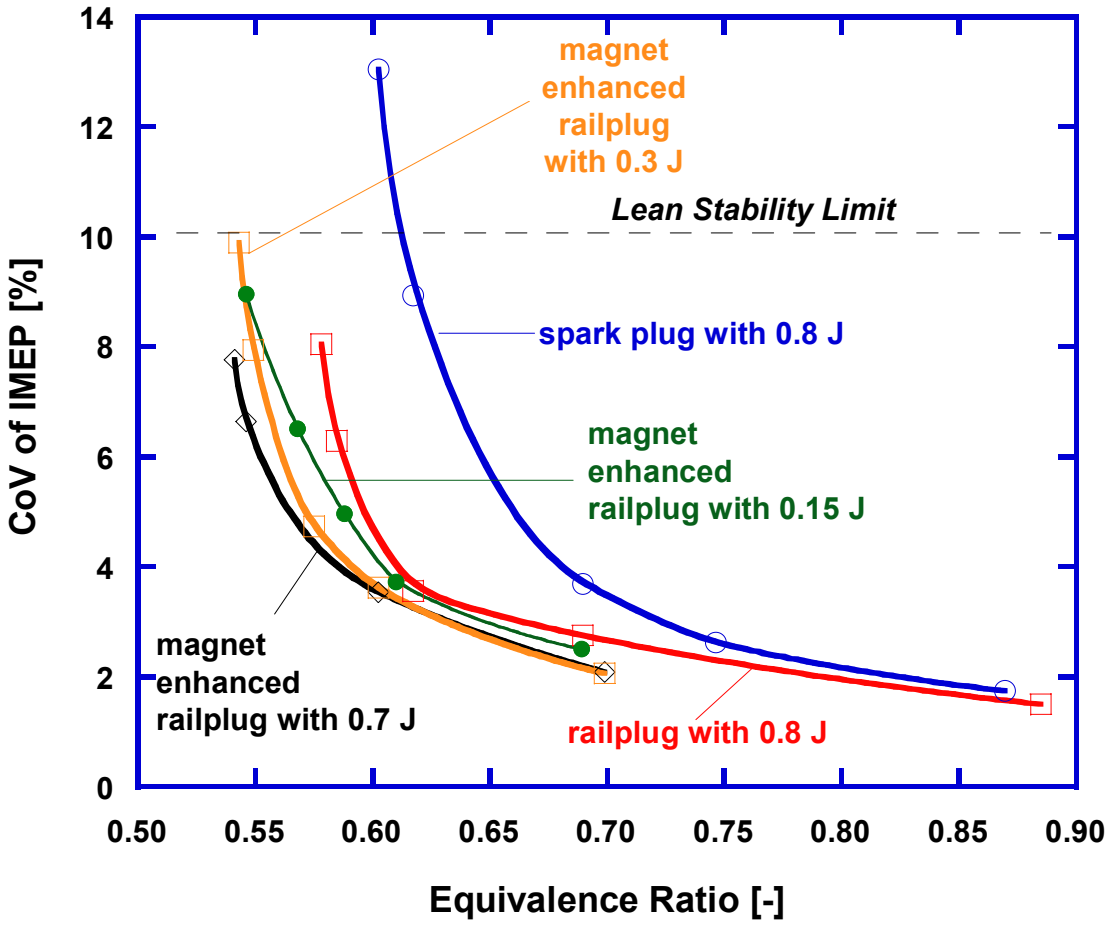

Figure 32. The effects of discharge energy on combustion stability for the magnet-enhanced railplug compared to a spark plug and a conventional railplug.

Figure 32 shows that railplugs can provide good ignitability with as little as 0.15 J/shot of discharge energy, which is typical of the discharge energy for commercial capacitor discharge ignition systems. Lower discharge energies result in better durability, which is always welcomed for large-bore natural gas engines. However, for the magnetic-enhanced railplug, there is little effect of energy on combustion stability, especially near the Lean Stability Limit.

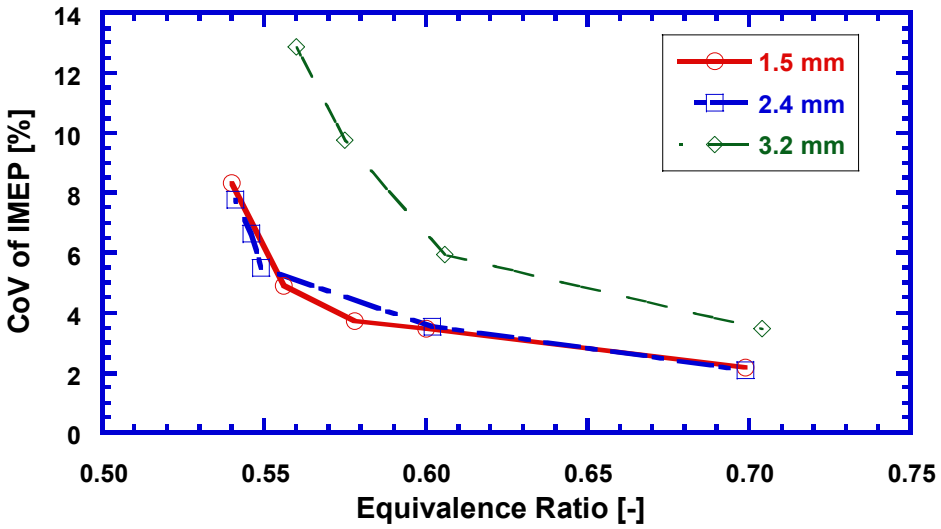

Figure 33. The effects of electrode size on railplug ignitability for magnet-enhanced railplugs with a discharge energy of 0.7 J/shot and duration of 0.6 ms.

The effects of electrode size on railplug ignitability are illustrated in Figure 33. The railplugs with smaller electrodes had better ignition performance because small electrodes enhance plasma movement, as discussed in the prior section. Small electrodes also decrease the flame kernel heat loss to the electrodes and thereby improve ignitability (Borman and Nishiwaki, 1987). Optimizing the cross-sectional size of the rails requires consideration of competing factors, however. Small electrodes absorb less heat from the ignited mixture through convection heat transfer. They also dissipate less heat by conduction. A simple analysis was used to clarify the tradeoffs involved.

In this model, the electrode for both spark plug and railplug geometries is approximated by a cylindrical pin fin attached to a base at temperature, T_B. The fin approximation is valid for small Biot number (Bi<<1) and a large length-to-diameter ratio (L/D>>1). These limits are satisfied for the conditions of interest in this work. For simplicity, assuming steady heat transfer and neglecting source terms for Joule heating and plasma heating, the conduction loss balances the convective heating.

$$kA_c \frac{d^2T}{dx^2} - h_c p(T - T_g) = 0 \tag{5}$$

where A_C is the cross-sectional area and p is the perimeter of the electrode. Using an insulated tip boundary condition yields the solution:

$$T^* = \frac{T\text{-}T_g}{T_B\text{-}T_g} = \frac{\cosh \beta(L - x)}{\cosh \beta L} \tag{6a}$$

where, T_g is the in-cylinder gas temperature, T_B is the temperature of the plug base; and:

$$\beta = \left(\frac{h_C P}{kA_C} \right)^{1/2} \tag{6b}$$

The convective heat transfer coefficient h_c can be obtained from Eichelberg's formula (Borman and Nishiwaki, 1987):

$$h_c = 7.67(C_m)^{1/3}(PT_g)^{1/2} \quad W/(m^2\text{-}K) \tag{7}$$

where C_m is the mean-piston-speed in m/s and P is the pressure in MPa.

The predicted effect of rail diameter on the non-dimensional temperature T^* is shown in Figure 34. As the electrode size decreases, the tip temperature increases. Cases that yield a tip temperature that can trigger ignition (≥1000 K) must be avoided.

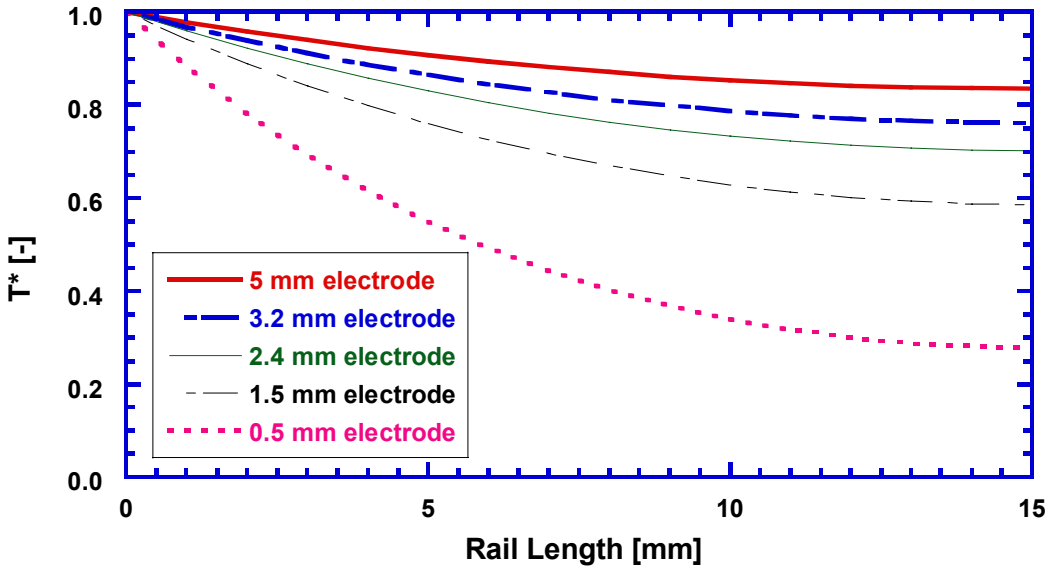

Figure 34. Predicted electrode temperature distributions for railplugs.

3. NUMERICAL METHODS AND RESULTS

One of the goals of this project was to develop an improved model for the spark ignition process. Specifically, we developed a multidimensional simulation of spark ignition to predict spark physics from basic principles. The challenges of multiple-scale, multi-physics modeling are well known and the details will not be covered here in detail. The fundamental issue is that a self-consistent modeling framework must be developed to smoothly transfer appropriate data/information between adjacent, varying-coarseness models. Resolution effects in time and length scales must be rationally modeled to answer the questions of interest:

1. What critical properties of a flame kernel are required to initiate a self sustaining flame?
2. How does the energy deposition process (rate of power input) affect the critical kernel properties?
3. Can ignition circuit parameters be used to tune the energy deposition process in a way to affect the transition of a kernel to a self-sustaining flame?
4. What physics control railplug arc development?
5. Can geometrical features of railplugs and spark plugs be analyzed by CFD?

In our attempts to answer these questions, we used a suite of three numerical simulation codes. For ease of portability, we used three well-documented codes: PSPICE, FCT, and Fluent. For some simple analyses, we have also written stand-alone codes to investigate specific parts of these problems. The problem of interest is a spark discharge where the global circuit parameters are, for-the-most-part, well specified by a circuit simulation tool like PSPICE. The critical approximations that must be closed in the PSPICE simulation are the spark gap physics. We use the term "spark gap" to refer to either the gap in a spark plug or in a railplug. The time-dependent circuit history relies on some approximate form of the spark gap physics in order to advance in the time domain. The spark discharge process occurs on time scales starting at approximately 10 ns and proceeding through millisecond characteristic times. The time scale ratio is on the order of 10^5. The early electric arc length scales are on the order of nanometers and evolve to several millimeters. No single simulation tool is appropriate to proceed over these ranges of time and length scales. The early time (< 100 microsecond) physics relies on accurately simulating the blast wave development and the electrical energy deposition processes. At later times, the chemical reactions and flame growth processes are best described using low Mach number approximations for the flow. Because of this, we have tailored our choice of tools to best address the different parts of this problem. The early spark processes are simulated using the Flux Corrected Transport (FCT) algorithm that has been developed to accurately simulate fast flows with shocks. While it is computationally infeasible to convert our two-dimensional FCT code into a three-dimensional form, we have used the code to explore how different current profiles affect the early-time physics of the spark discharge process. The influence of high temperature thermal properties and high temperature chemistry are incorporated into the code to accurately simulate these early times. We have explored the role of chemistry and transport on accurate models of the early spark process. We have detailed how representative chemistry, which has the effects of the various plasma steps, can be used to simulate the most important characteristics of the plasma evolution. We have evaluated transport properties

from the literature to properly account for the role of these parameters in the early discharge events. We have then used as initial conditions the output of the FCT code as an input into fully three-dimensional Fluent calculations where hydrocarbon chemistry (flame related chemistry) is prescribed. With the Fluent calculations, we are able to explore how bulk parameters, such as flow in the spark gap, affect the transition to full self-sustained flame cases. From the two flow-based solvers, we extract a simplified model for spark gap physics and place this into the PSPICE solver to close the loop in assessing the impact of circuit and spark plug parameters on engine performance measures.

The PSPICE circuit analysis, including our development of an electronic equivalent of the spark gap, is discussed in Section 3.1. Our development of a chemical kinetics mechanism for methane, including plasma chemistry, is discussed in Section 3.2. We developed three different models for ignition and flame propagation from a spark plug, including a three-dimensional model. These models are discussed in Section 3.3. Section 3.4 is a discussion of our model for spark evolution from a railplug.

3.1. Global Circuit Analysis

The spark can be divided into 4 basic phases: Pre-breakdown, Breakdown, Arc, and Glow. The timing and duration of each phase is dictated by the characteristics of the ignition circuit (including the igniter). Pre-breakdown is the time period when the voltage of the coil is building until it is either large enough that a spark can jump the gap or, if the required breakdown voltage exceeds the capacity of the coil, a misfire occurs. Typically, this phase lasts for ~ 1 nanosecond. There is no energy deposition as there is no current flowing through the spark gap. As soon as enough ionizing electrons are produced to make the discharge self-sustaining, "breakdown" occurs. At breakdown, a highly conductive streamer (passage for electrons) is initiated, which leads to a sharp rise in current and sudden fall in voltage across the gap (Raether, 1964). This phase lasts for approximately 10 nanoseconds. There is very little energy deposition because of the short duration of this phase. Typically, between 0.3 and 1 mJ of energy, is deposited during breakdown. Breakdown may be perceived as a barrier that needs to be crossed to obtain a spark. Once breakdown occurs, the next phase, arc, begins. Arc is caused by the thermionic emission of electrons from the cathode (ground strap or ground electrode for negative ground systems) surface (Loeb, 1939). The voltage drops rapidly to a low value (of around 50 V). The current starts to fall and the voltage stays at a constant value throughout the arc phase. The cathode surface temperature rises to ~3000 K, which is above the melting temperature of the cathode material. The arc is caused by the thermionic emission of electrons from a molten spot on the surface of the cathode (Sze, 1969). Once the melting point of the metal has been reached, the cathode can then emit electrons. The arc cannot be sustained without these melted spots, which also lead to a loss of electrode material through evaporation. For this reason, the majority of the cathode erosion takes place during the arc phase. The electrons emitted from these pools are required to sustain the arc. The arc phase typically lasts for ~10 microseconds and energy deposition is of the order of 1 mJ. The voltage during arc is around 50 V at 1 bar in air with a 1 mm gap, split into 15 V in cathode fall, 25 V in anode fall, and 10 V in arc plasma (Maly, 1984). The cathode fall voltage is a function of the cathode material. Glow is the final phase of the spark. During glow, the mechanism of the emission of electrons from the cathode surface changes. The glow phase begins when the dominance of the thermionic emission of electrons ends because the pool of melted metal is no longer available. Glow discharges are similar to arc discharges

but exist with a "cold" cathode. That is, arc ends and glow begins when the cathode surface temperature falls below the melting point. During the glow phase, the bombardment of positive ions on the electrode surface becomes the dominant mechanism (Meek and Craggs, 1953). Since this mechanism has a very low efficiency, the current decays to a low value (less than 1 A). The voltage, on the other hand, rises to a higher value (around 500 V). The glow phase is, thus, characterized by low currents and high voltages (relative to the arc phase). The voltage splits into the following typical components: 400 V for the cathode fall, 25 V for the anode fall, and 100 V/mm for the positive column (Maly, 1984). For an inductive ignition system, the glow phase lasts for about 3 ms. During this period, 30-100 mJ of energy is typically deposited, which is far more than for the other three phases. This is mainly due to the fact that the duration of glow is longer. The glow ends when the current in the gap decays to near zero. Each of these phases was modeled.

A circuit-solving software package, PSPICE, was the heart of our model for our initial exploration of the role of the ignition circuit. PSPICE automatically accounts for the dynamic response of all types of conventional electronic components, such as capacitors, resistors, and inductors. However, the spark gap is not a conventional electronic component. Thus, the focus of our effort was modeling the spark gap for each of the phases of ignition. Schroeder's inductive ignition circuit model (Schroeder, 2002) was downloaded from the internet and modified for the present study. Each modification is listed below.

1. The model was altered to match the experimental ignition system used for validation.
2. The breakdown voltage was modeled as a function of spark gap size, gas pressure, and gas temperature.
3. The voltage during arc was modeled as a function of spark gap.
4. The voltage during glow was modeled as a function of spark gap.
5. The current at which the arc-to-glow transition occurs was modeled.

The static breakdown voltage can be obtained from Paschen's Law, which defines the breakdown voltage for different gases as a function of gap size, temperature, and pressure for quiescent conditions and clean electrodes. Paschen's Law applies when the product of pressure times spark gap is less than 13.33 bar-mm (Bazelyan and Raizer, 1998), which is sufficient for the time of ignition in most light-duty engines and is close to the appropriate conditions for boosted large bore natural gas engines. For air, the static breakdown voltage is:

$$V_{BD} = 24.22x + 6.08\sqrt{x} \quad [\mathrm{kV}] \tag{8}$$

where

$$x = \frac{293}{T}\frac{P}{1.013}\frac{g}{10} \quad [-] \tag{9}$$

where gas temperature T is in K, the gas absolute pressure P is in bar, and the gap, g, is in mm. Although Paschen's Law does not strictly apply to breakdown for spark plugs in engines, it is sufficient for the present purpose, which is to model the ignition process. So little energy is deposited during breakdown that the model needs only what the actual breakdown process provides – a trigger allowing the circuit to provide arc and glow.

The arc voltage consists of 3 basic components: the cathode fall (15 V), the anode fall (25 V), and the positive column (10 V/mm). The cathode and anode "falls" are narrow regions near the electrodes, where a sharp drop in potential occurs. The cathode fall is

required for sustaining numerous cathode hot spots. The arc voltage can be defined as (Maly, 1984):

$$V_{arc} = 40 + 10g \quad [V] \tag{10}$$

The effects of pressure, temperature, and composition are discussed after the glow voltage model is introduced.

The glow voltage consists of the same three elements as the arc voltage: a positive column plus cathode and anode falls. However, the cathode fall voltage is very high during glow.

$$V_{glow} = 425 + 100g \quad [V] \tag{11}$$

The equations for arc and glow voltage will be different for different gases. However, since the gas encountered in engines is predominantly air, these equations should be accurate for all in-cylinder gas mixtures. Equations 10 and 11 are valid for all practical gap lengths and pressures because the anode and cathode fall form a very small portion of the gap length. When the gap is altered, only the length of the positive column changes appreciably and the anode and cathode fall regions remain unaltered (von Engel, 1965). Also, the cathode and anode fall voltages are not significantly affected by pressure (Howatson, 1976). The voltage of the positive column is independent of temperature and is a weak function of pressure. Therefore, it is reasonable to assume that the arc and glow voltage relations hold for all temperatures, pressures, and mixture compositions encountered inside an engine.

Most investigators mark the arc-to-glow transition when the current falls below some current threshold [e.g., 100 mA was used by Maly (1984) and 60 mA was used by Kim and Anderson (1995)] without a physical justification for the threshold chosen. It has been assumed that by the time the current has dropped to some low current, the thermionic electron emissions (which are characteristic of the arc phase) have ended. Our research team found (Gao, 2005) that the luminosity changes at the transition point, indicating some change in physical mechanism. We also found that the transition point varies from shot to shot, possibly due to differences in cathode cooling rate, and the current at the time of the arc-to-glow transition was as low as 20 mA. The mechanism of electron emission from the cathode changes to bombardment of the positive ions and the transition to the glow phase starts.

However, there are some unanswered questions related to the transition. The current in the gap is due to electron emissions from the cathode. This electron emission is governed by two basic mechanisms: 1) thermionic emissions and 2) bombardment of positive ions on the cathode. The total current can be found as a function of temperature by equating the energy transfer to the cathode and the radiated heat loss (Loeb, 1939). Consequently, the total current i is:

$$i = \frac{f\sigma T_c^4}{V_c} \quad [A] \tag{12}$$

where f is the cathode area in m^2, σ is the Stefan-Boltzmann constant [5.67E-8 $W\text{-}m^{-2}K^{-4}$], T_c is the cathode surface temperature in K, and V_C is the cathode fall voltage. The thermionic emissions are a surface phenomenon on the cathode and the thermionic current is given by the expression (Loeb, 1939):

$$i_t = fAT_c^2 \exp(-B / T_c) \quad [A] \tag{13}$$

where A and B are Richardson Constants (Sze, 1969). The Richardson Constant B is

$$B = q\phi / k \quad [K] \tag{14}$$

where q is the charge on an electron [1.602E-19 A-s/electron], ϕ is the work function of the metal [eV], and k is Boltzmann's constant [1.380E-23 J/K]. The value of the constant B was easy to find as the work functions of most metals are readily available (e.g., Sze, 1969). For metals, Richardson Constant A can be found from:

$$A \approx A^* = \frac{4\pi q m k^2}{h^3} \tag{15a}$$

where m is the effective mass and h is Planck's constant (6.63E-34 J-s). The effective mass depends upon the direction of current travel for semiconductors but is essentially the mass of a free electron for metals (Sze, 1969). Thus, for metals:

$$A \approx 1.2 \cdot 10^6 \quad [A/(m^2\text{-}K^2)] \tag{15b}$$

This leaves the cathode temperature as an unknown in Equations 12 and 13. Taking the ratio of the total current to the thermionic current (i.e. dividing Equation 12 by Equation 13) yields:

$$i / i_t = \frac{\sigma T_c^2}{A V_c \exp(-B / T_c)} \quad [-] \tag{16}$$

The unknowns in Equation 16 are the current ratio and the cathode surface temperature. An experiment conducted by Druyvesteyen (1939) was used to find the current ratio. Druyvesteyen found a thermionic current of 0.1 mA with a cathode diameter of 1.8 mm at a temperature of 2000 K (± 50 K). The cathode material used by Druyvesteyen was tungsten. Using a work function for tungsten of 4.4 eV yields B = 51078 K. Then from Equation 13, A = 121 A/cm^2-K^2, which agrees closely with Equation 15b. Inserting all values into the right hand side of Equation 16 yields $i/i_T \sim 1500$. If it is assumed that the thermionic current is 1500 times smaller than the total current at the time of the arc-to-glow transition, Equation 16 can be used to determine the cathode surface temperature at the time of this transition. Equation 12 can then be solved for the current at the time of the arc-to-glow transition (given the cathode fall voltage of 15 V). This procedure yields a current at the time of arc-to-glow transition that depends upon the cathode material. As examples, for a 2.8 mm cathode (typical for light-duty spark plugs), the transition current for nickel (ϕ = 4.50 eV) is 0.41 A and for platinum (ϕ = 4.72 eV) it is 0.51 A. The corresponding cathode temperatures (2053 K and 2162 K, respectively) are higher than the melting points for these two materials (1728 K and 2045 K, respectively). This corresponds with the fact that electrode erosion occurs during the arc phase; during glow the surface temperature is too low to sustain a melted surface. However, this technique involves the assumption that the thermionic current is 1500 times smaller than the total current. If, instead, one simply uses the melting temperatures of the metals in Equation 12, the transition currents are calculated to be 0.21 A for nickel and 0.41 A for platinum. Furthermore, substituting the work function for each metal into Equation 14 and then using this value for B for each material along with the melting temperature for that metal in Equation 16 yields a value for i/i_t that depends upon the material and is not 1500 (except for tungsten). Therefore, we recommend the use of Equation 12 to find the current at the time of arc-to-glow transition using the melting temperature of the cathode material.

Initial model validation was performed using an inductive ignition system with the specifications shown in Table 2. The gap voltage was measured using a Tektronix P6015 voltage probe. This probe has an attenuation of 100. This was tested with a standard high voltage supply. This probe was inserted (clipped on) at the point where the spark plug wire connects to the spark plug. It effectively measures the voltage of the gap. This probe has

high resistance and low capacitance so that it does not interfere significantly with the measured values. However, the time response of the voltage probe was insufficient to capture breakdown or arc. Thus, the model has only been validated for the glow phase at this time. The current in the spark plug wire was measured using a Pierson coil ("current loop").

Table 2. Description of the Experimental Ignition Circuit.

Parameter	Value
Turns ratio of coil	104
Resistance of primary windings	1.43 Ω
Resistance of secondary windings	14,000 Ω
Leakage Inductance of the coil	0.36 mH
Core inductance	6 mH
Resistance of the spark plug wire	8,000 Ω
Inductance of the spark plug wire	250 μH
Inductance of the spark plug	10 nH
Capacitance of spark plug and probe	70 pF

Figure 35 is an example comparison between the predicted and measured voltage histories. Breakdown and arc are not obvious on this graph due to the scaling. The agreement is very good except that the duration of the simulated glow is slightly shorter than the experimental value. The turns ratio of the coil, the resistance of the primary windings, and the core resistance strongly affect the spark duration. However, the turns ratio and the primary resistance were accurately determined. Therefore, it appears that the discrepancy in the spark duration is because the value of the core inductance supplied by the manufacturer was not accurate. If the core inductance is changed from 6 mH, to 8 mH, the spark duration for all cases examined also agrees well.

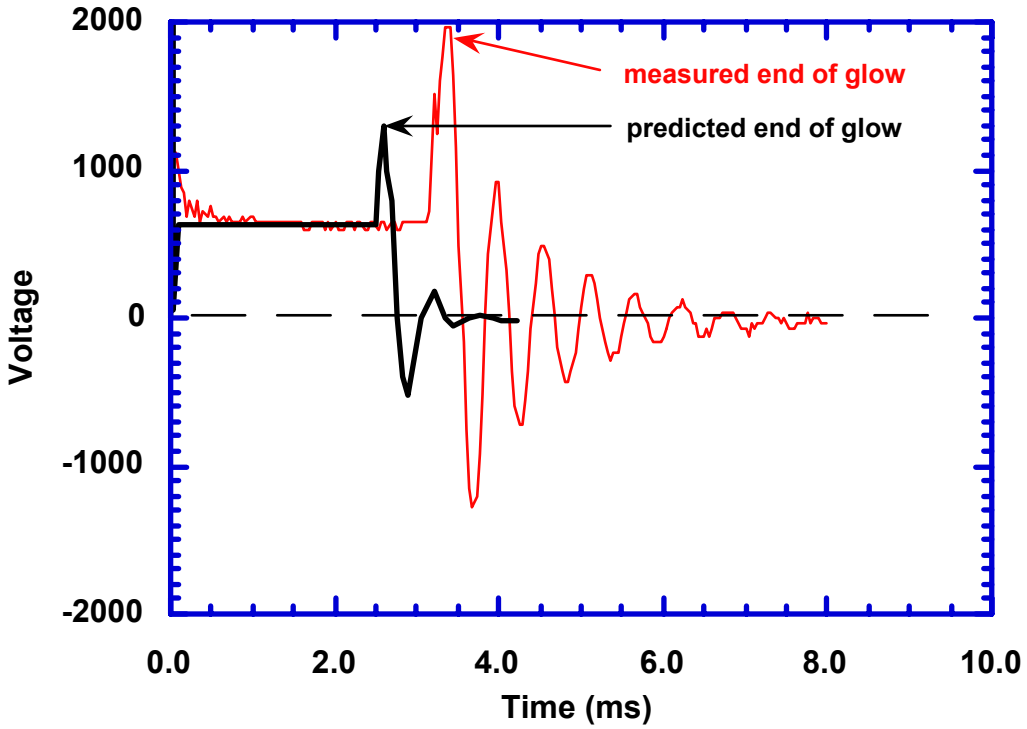

Figure 35. Comparison of predicted and measured voltage histories for a 2 mm spark gap at 1 bar, 298 K.

Table 3 shows the close agreement obtained between the model predictions and experimental data for the voltage during glow. Again, the agreement is quite good.

Table 3. Comparison Between the Experimental and Predicted Voltage during Glow.

Spark Gap (mm)	Predicted Voltage	Observed Voltage	Error (%)
0.7	495	500	1.00
1.0	525	540	2.78
1.5	575	620	7.26
2.0	625	620	0.81
3.0	725	740	2.03

Figure 36 is a comparison between the measured and predicted current histories. The model predicted that the current versus time profile is the same for all resistance values and gap lengths during the glow phase. This concurred with what was observed in the experiments. As shown in Figure 36, the current waveforms agree reasonably well given the significant noise in the signal.

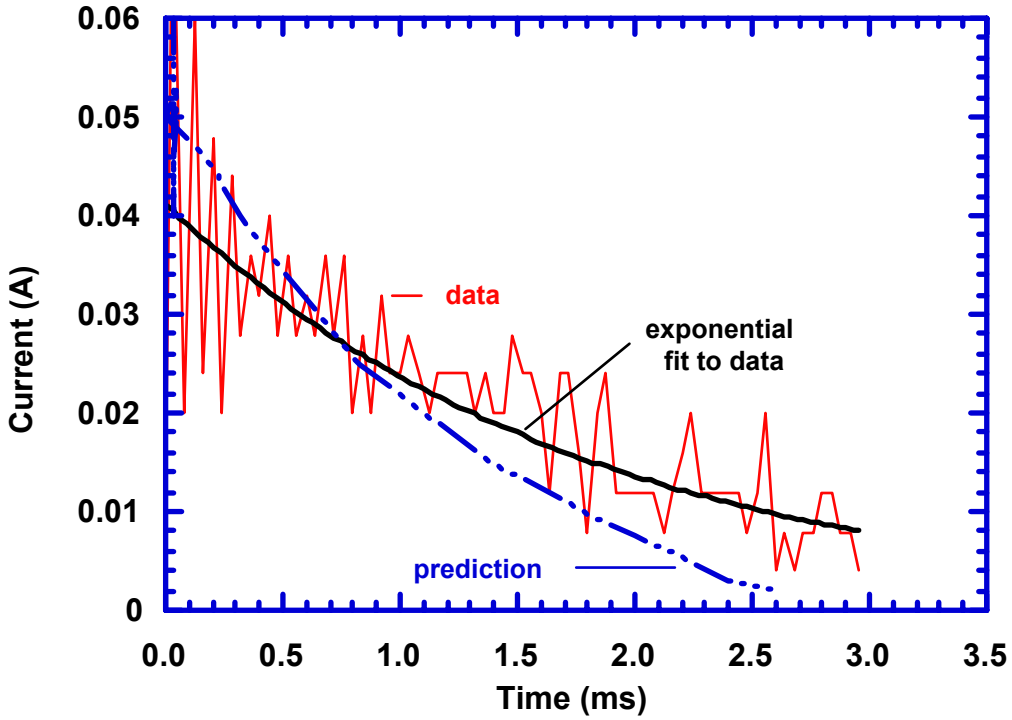

Figure 36. Comparison between experimental and predicted current histories.

The model was exercised to examine the effects of various circuit parameters on the ignition circuit dynamics for an inductive ignition system. Energy deposition during the glow phase dominates energy deposition for an inductive ignition system. Recall that the model has been validated for glow. The conclusions drawn regarding energy deposition during the glow phase are summarized in Table 4. The other circuit parameters, such as inductances and capacitances of the spark plug and spark plug wire, do not significantly affect the energy deposition for an inductive ignition system. We generated a paper covering the circuit model for an inductive ignition system (Bhat et al., 2003a).

Table 4. Effects of Circuit Parameters for an Inductive Ignition System on Energy Deposition.

Parameter (increasing)	Energy Deposited	Time to Deposit Energy	Extent of Impact
Turns ratio	increases	increases	significant
Primary resistance	decreases	decreases	significant
Core inductance	increases	increases	significant
Secondary resistance	decreases	decreases	weak
Spark plug wire resistance	decreases	decreases	weak

The railplug circuit model is a simple extension to the model for an inductive ignition system. As shown earlier in Figure 9, the driver electronics for a railplug consists of an inductive ignition system – to provide breakdown – and a "follow-on circuit" that dumps its energy once a path is established by breakdown. The follow-on circuit provides the high

current that is necessary to generate a Lorentz force to move the arc down the railplug muzzle. The primary components of the follow-on circuit are a capacitor (C2) that can be charged to an arbitrary voltage, and an inductor (L1). Both the capacitor and the inductor can be used to shape the current profile. The follow-on circuit also includes a diode (D1) to prevent the breakdown current from flowing into the follow-on circuit, a resistor (R2) in parallel with the diode to discharge any remaining voltage after the arc has ceased, and a blocking capacitor (C1) to prevent the current from the follow-on circuit from flowing backward through the coil.

The railplug circuit model was validated by performing experiments with a parallel railplug at 1 bar and 298 K. The spark gap at the breech was 1 mm and the parallel rails were 2 mm apart and 10 mm long. The current flowing through the railplug was used for validating the model. Experimental data was taken with various follow-on capacitors and a range of initial charge on the capacitor. Figure 37 illustrates the comparisons between the predictions and the experiments. Table 5 compares the peak current measured during the experiments and the model predictions. The agreement is quite good.

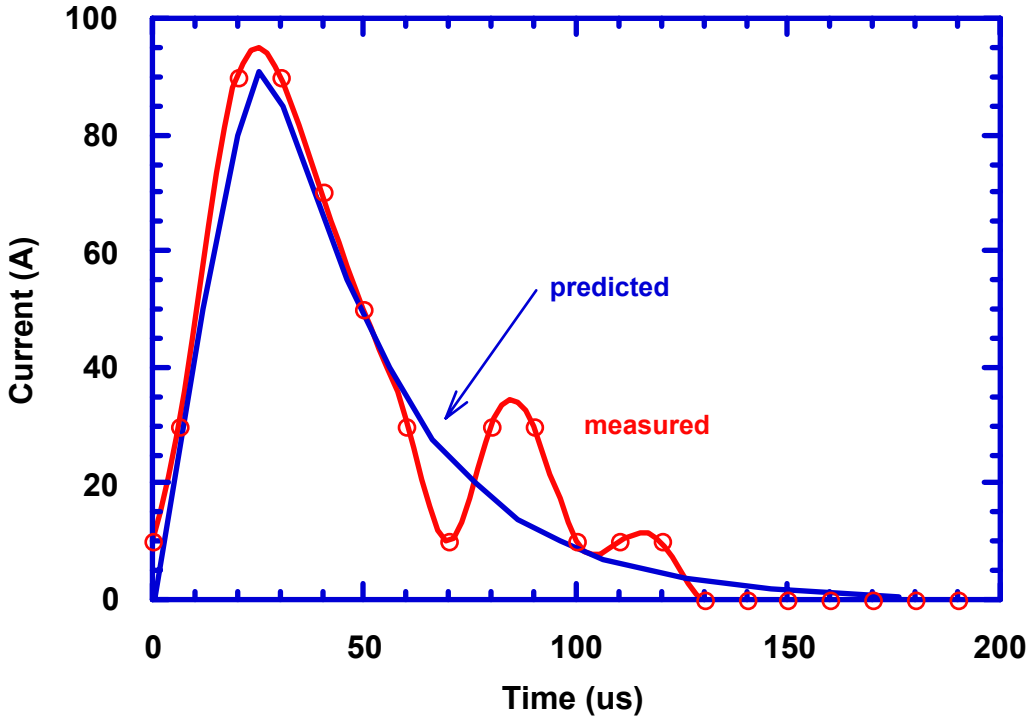

Figure 37. Comparison between model predictions and experimental current profile for a capacitance of 33 μF charged to 100 V.

Table 5. Comparison Between Measured and Predicted Peak Currents.

Capacitance (mF)	**Charging Voltage** (V)	**Predicted Peak Current** (A)	**Measured Peak Current** (A)	**Error** (%)
33	100	91	92	1.1
47	100	79	75	5.3
130	100	87	93	6.5
330	115	103	102	0.9
330	95	90	90	0.0

After validating the model for the railplug circuit, the model was used to explore the effects of the various circuit parameters. Figure 38 illustrates the effects of the capacitance (C2). For a fixed charge of 100 V, increasing the capacitance increases both the stored energy and the energy delivered to the railplug gap, and also increases the duration of the arc. As another example, Figure 39 shows that the inductance (L1) can be used to stretch out the current duration without having a significant effect on the delivered energy. Table 6 shows the overall results of this exploration. Circuit parameters not noted in this table did not have a significant effect on either the energy delivered or its duration. It is concluded that 1) the resistor in parallel with capacitor C1 should be as large as possible, 2) the combination of capacitance C1 and charging voltage should be no larger than required to assure ignition, and 3) inductor L1 should be used to shape the current profile. Our team submitted a technical paper that was subsequently published and covered the railplug ignition circuit model (Bhat et al., 2003b). However, the tradeoff between inductance and peak current must also be considered, as illustrated in Figure 40. Also, the peak current decreases as the charging voltage decreases, as shown in Figure 41. The peak current and rate of current rise are important because they affect how rapidly the arc moves away from its position at breakdown.

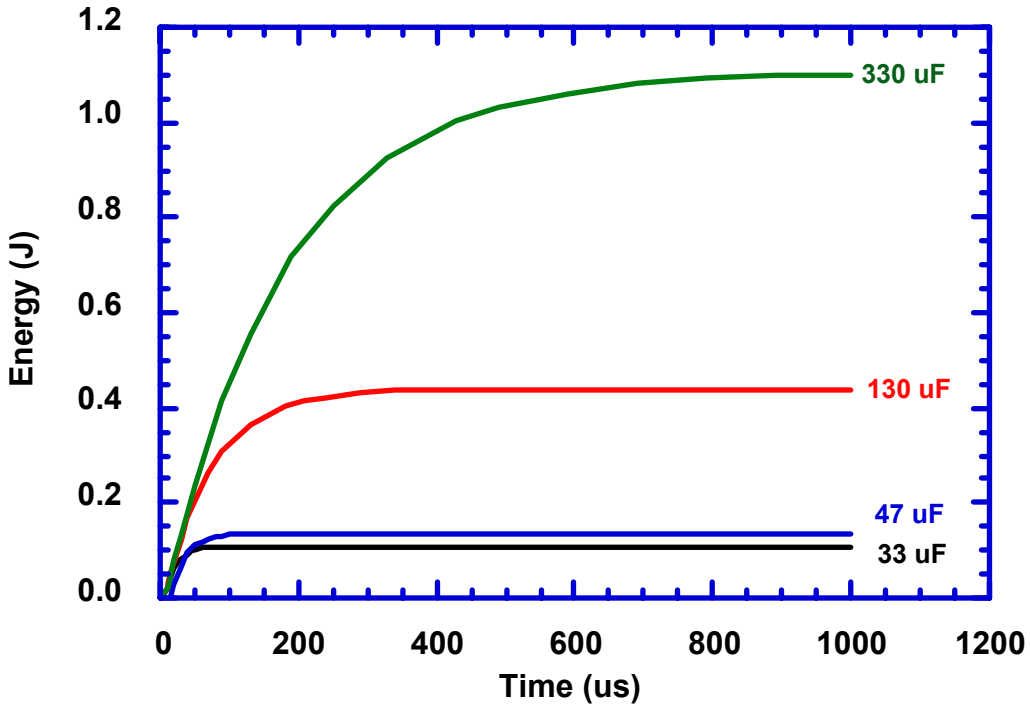

Figure 38. Effect of follow-on circuit capacitance on energy delivery for an initial charge of 100 V.

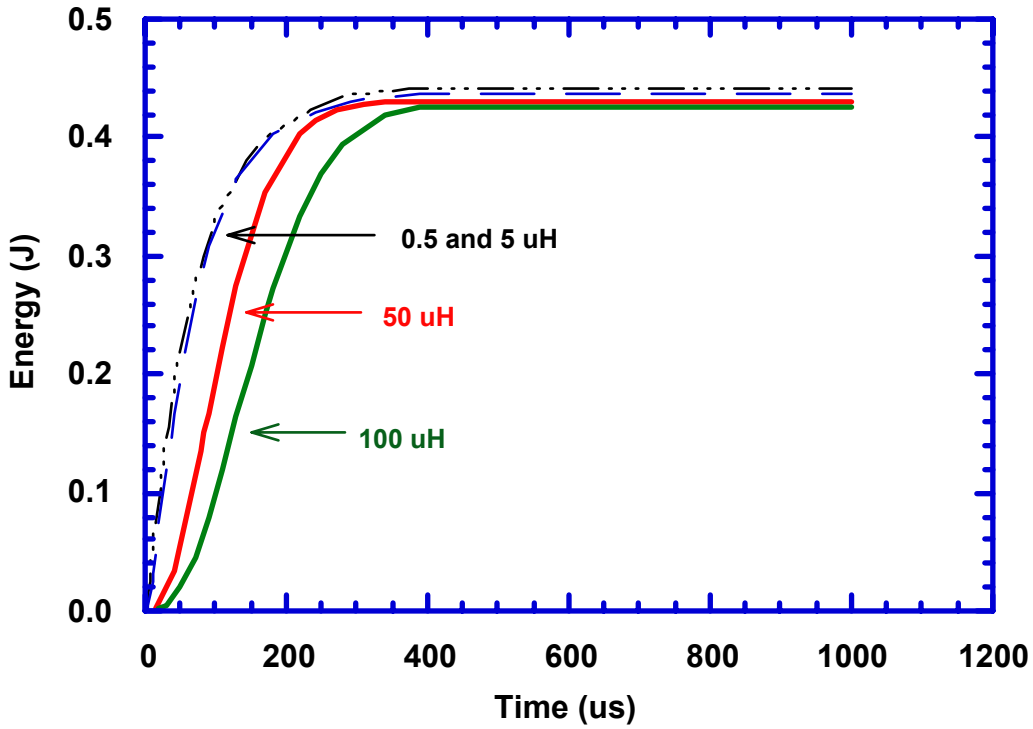

Figure 39. Effect of follow-on circuit inductance on energy delivery for a capacitance of 130 μF and an initial charge of 100 V.

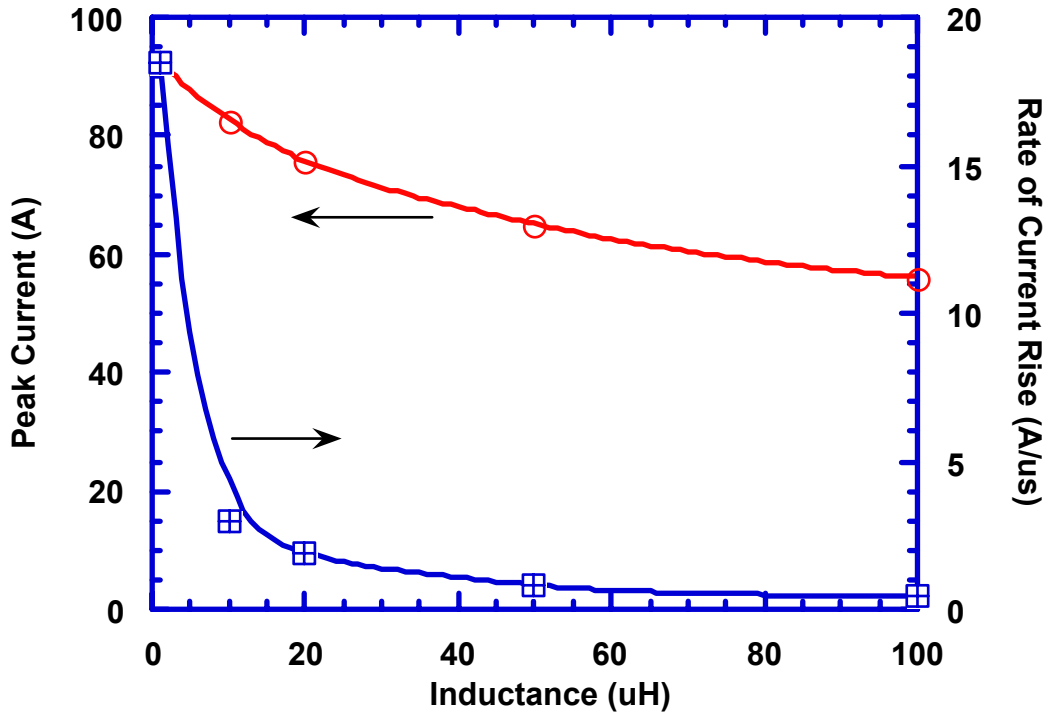

Figure 40. Increasing the inductance stretches out the current delivery but also decreases the peak current and the rate of current rise.

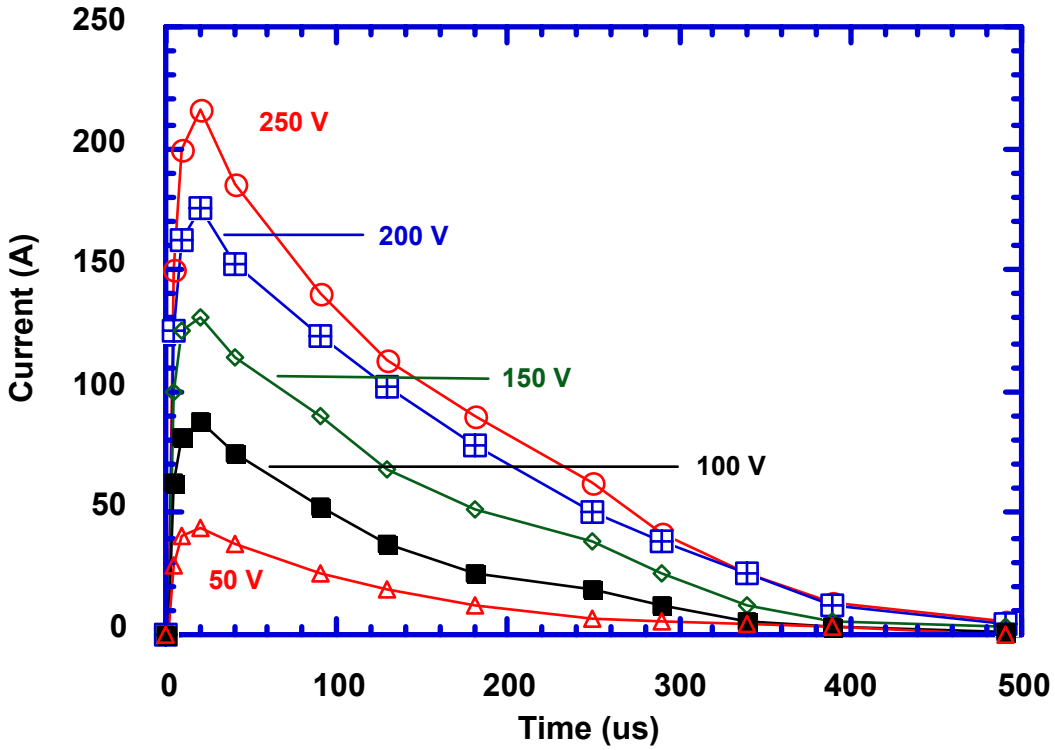

Figure 41. The charging voltage affects the peak current but not the rate of current rise.

Table 6. Effects of Circuit Parameters for Railplug Ignition System on Energy Deposition

Parameter (increasing)	Energy Deposited	Time to Deposit Energy	Impact on Energy	Impact on Duration
Capacitance C2	increases	increases	significant	significant
Charging voltage	increases	no effect	significant	no effect
Inductance L1	no effect	increases	weak	significant
Parallel resistance R2	increases	no effect	significant	no effect

The major deficiency in the initial circuit-side model relates to the detailed spark physics and the effects of energy deposition on the thermodynamic state which influences the transport properties.

3.2. Thermodynamics and Chemistry in the Spark Gap

The development of a current-carrying channel between an electrode pair involves quite complex physics. Our intent was to focus on questions of how the spark physics can influence the later flame kernel development as compared to the need to focus on the development of the conducting plasma. Said differently, we wanted to retain the essential details of the development of the current carrying channel that allow us to accurately predict the flame kernel evolution. For a short period of time, the thermal state within the spark channel post-breakdown is not in thermodynamic equilibrium. We focused our work on the evolution of states after thermal equilibrium is approximately valid. After such time it is possible to discuss a thermodynamic state for the system. As previously noted, the thermodynamic state within the gap is used to infer the transport property state of the gap, which can be coupled to the circuit-side solver (e.g., the electrical conductivity of the gap is a required parameter in the circuit-side model). As energy is deposited into the gap, the thermodynamic state evolves through chemical processes by which the composition evolves. Undoubtedly, the number of chemical species and chemical steps that are actually involved in this complex process are quite large and would prove infeasible to compute. However, the chemical evolution has certain clear effects in that the generation of certain intermediate species serve as energy storage paths which, for example, might limit the temperature increase as energy is added in some conditions (acting endothermically), and might serve to maintain the temperature through other portions of the system evolution (e.g., acting exothermically).

Below, we describe the steps required in generating the appropriate ignition kinetics. This consists of conventional methane flame chemistry and, because the gas temperature during the ignition process can exceed 6000 K, additional reactions that are important at these high temperatures (plasma reactions). The plasma reactions that are of interest are:

CH4 --> C + 4H	(RX 1)
C + O = CO	(RX 2)
O2 + M = 2O	(RX 3a)
H + O = OH	(RX 3b)
H + OH = H20	(RX 3c)
CO + OH = CO2 + H	(RX 3d)

Ionization reactions are not included because they are not important for gas temperatures below 10,000 K (Sher et al., 1992). Reactions 2-3d liberate chemical energy via a path other than via normal flame chemistry. That is, at extremely high temperatures, such as those found during electrical energy deposition in the spark gap, the fuel and molecular oxygen can become completely dissociated. When the plasma cools to 6000 K and lower, these atoms recombine exothermically into stable species like CO and OH, which can then react further to form more stable species such as CO2 and H2O, releasing even more energy. This path is not included in any other model, but is critical. However, Reactions 3a-3d are generally incorporated in conventional flame chemistry (but the sequence leading to Reactions 3b-3d is different at the lower temperatures associated with flames). Thus, the focus of this subtask was to find rates for Reactions 1 and 2.

Reaction 1 is a global reaction that incorporates a series of sequential and simultaneous reactions. The elementary reaction path and rate data are provided in Table 7. The rates for Reactions 4-8 in Table 7 were taken from results for high temperature (6,200-11,000 K) methane pyrolysis reactions (Fincke et al., 2002). Reactions 3a and 8 in Table 7 are normally included in conventional flame chemistry but the rate data are obtained for the temperature range that is appropriate for flames. Due to the present interest in plasma chemistry, the rates for Reactions 3a and 8, and also Reaction 2, were obtained from a study focused upon plasmas formed during re-entry of space vehicles (Gupta et al., 1990). Similarly, the rate for Reaction 3d in the forward direction was obtained from a study of shock-heated H2/CO/O2 mixtures (Browne et al., 1969) and the reverse rate was obtained from Kochubei, and Moin (1969). The plasma reaction set in Table 7 includes 15 species. The GRI mechanism (GRI-Mech 3.0, Smith et al. 2002) can be used to simulate the conventional flame chemistry. It includes 52 species (not including Argon), all of which also appear in Table 7. Therefore, use of elementary kinetics for modeling the ignition and flame propagation process involves a total of 52 species.

Table 7. Elementary Plasma Reactions and Corresponding Rate Data.

Reaction	A (cm, gmole, s)	m (-)	E_a (cal/gmole)	
CH4 = H + CH3	4.7*E47	-8.2	117643	(RX 4)
CH3 + M = CH2 + H + M	1.0*E16	0	90524	(RX 5)
CH2 + H = CH + H2	6.0*E12	0	-1791	(RX 6)
C + H2 = CH + H	4.0*E`4	0	23235	(RX 7)
CH + M = C + H + M	1.9*E14	0	66923	(RX 8)
C + O -> CO	7.253*E13	0	0	(RX 2f)
CO -> C + O	5.21*E12	3.0	256350	(RX 2b)
O2 + M -> 2O + M	3.61*E18	-1.0	118800	(RX 3a,f)
2O + M -> O2 + M	3.01*E15	-0.5	0	(RX 3a,b)
N2 + M -> 2N + M	1.92*E17	-0.5	226000	(RX 9f)
2N + M -> N2 + M	1.09*E16	-0.5	0	(RX 9b)
H + O = OH	5.0*E17	-1.0	0	(RX 3b)
H + OH -> H20	2.2*E22	-2.0	0	(RX 3c,f)
H2O -> H + 0H	7.42*E28	-3.0	122600	(RX 3c,b)
CO + OH -> CO2 + H	3.7*E11	0	699	(RX 3d,f)
CO2 + H -> CO + OH	1.0*E14	0	24244	(RX 3d,b)

However, because the spatial scales for these simulations are of the order of microns and the time scales are of the order of nanoseconds, simulations that involve elementary kinetics are much too consumptive of computational time. Thus, it was necessary to develop simplified chemistry for both the plasma reactions (converting Reactions 4-8 in Table 7 to the global reaction represented by Reaction 1) and the flame propagation reactions.

The simplified plasma chemistry that was developed for this project is presented in Table 8. Reaction 1 in Table 8 is a global representation of Reactions 4-8 in Table 7. A slow reverse rate was incorporated to this reaction for numerical stability. The reverse rate coefficients (e.g., RX 1b) were developed by Seers (2003), a PhD student on this project. To assure equilibrium, Reactions 2f and 2b from Table 7 were combined into a reversible reaction for the simplified mechanism in Table 8. Coefficients A and m for this reversible reaction were altered by Seers to produce the correct reaction rates for the simplified mechanism compared to the detailed mechanism. Similarly, Reactions 3c,f and 3c,b in Table 7 were changed to a reversible reaction (RX 6') for the simplified mechanism, as shown in Table 8. Reaction 5' in Table 8 is equivalent to Reaction 3b in Table 7, but Seers modified the rate coefficients to obtain better agreement with the predictions of the detailed mechanism. Reaction 1 in Table 8 reduces the number of species required to form C and H in the high temperature plasma from 7 to 3.

Table 8. Simplified Plasma Reactions and Corresponding Rate Data.

Reaction	A (cm, gmole, s)	m (-)	E_a (cal/gmole)		Ref.*
CH4 -> C + 4H	8.0*E44	-7.6	131000	(RX 1f)	1
CO = C + O	4.34*E27	0	256350	(RX 2)	2
O2 + M -> 2O + M	3.61*E18	-1.0	118800	(RX 3'f)	1
2O + M -> O2 + M	3.01*E15	-0.5	0	(RX 3'b)	1
N2 + M -> 2N + M	1.92*E17	-0.5	226000	(RX 4'f)	1
2N + M -> N2 + M	1.09*E16	-0.5	0	(RX 4'b)	1
OH = O + H	2.41*E15	0	120000	(RX 5')	3
H2O = H + 0H	7.42*E28	-3.0	122600	(RX 6')	4
CO + OH -> CO2 + H	3.7*E11	0	699	(RX 7'f)	5
CO2 + H -> CO + OH	1.0*E14	0	24244	(RX 7'b)	5

* = Rate data from: (1) Gupta et al. (1990) (2) modified by P. Seers, original coefficients from Mick et al., (1993), (3) modified by P. Seers, original coefficients from GRI-Mech 3.0, (4), GRI-Mech 3.0, (5) Browne et al., (1969).

The accuracy of the simplified mechanism is illustrated in Figures 42 and 43. Figures 42a-42d compare the predictions of the simplified plasma kinetics to those for the detailed plasma mechanism for conditions at the time typical of turbocharged large bore natural gas engines: 42 bar absolute pressure with an equivalence ratio (ϕ) of 0.6. Figures 42a and 42b are for a plasma temperature of 5000 K while Figures 42c and 42d are for 8000 K. To further illustrate the range of validity of the simplified plasma kinetics, Figures 43a-43d present similar information, but for ignition conditions that are typical for a light-duty naturally aspirated natural gas engine. Although it is difficult to see in these graphs due to the log scale, at the very earliest times, the concentrations of C and H are slightly over-predicted by the simplified mechanism. This is expected because the global fuel consumption reaction (Reaction 1 in Table 8) does not account for the C and H atoms that are bound within CH3, CH2, and CH. However, for all of these comparisons, the predictions of the simplified kinetics are quite close to those for the detailed mechanism. These comparisons provide confidence that the simplified plasma mechanism is adequate for modeling the ignition process during the high temperatures that occur during electrical energy deposition.

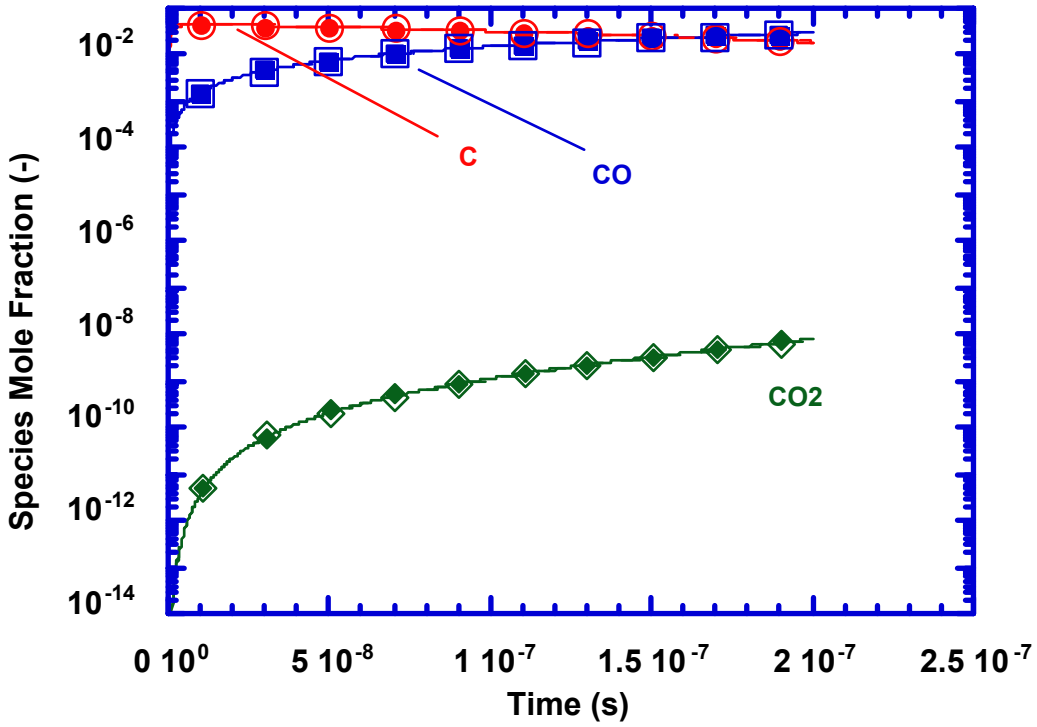

Figure 42a. Comparison of the rates of formation of C, CO, and CO2 for ϕ = 0.6, 42 bar, and 5000 K plasma temperature (filled symbols: elementary plasma kinetics; open symbols: reduced plasma kinetics).

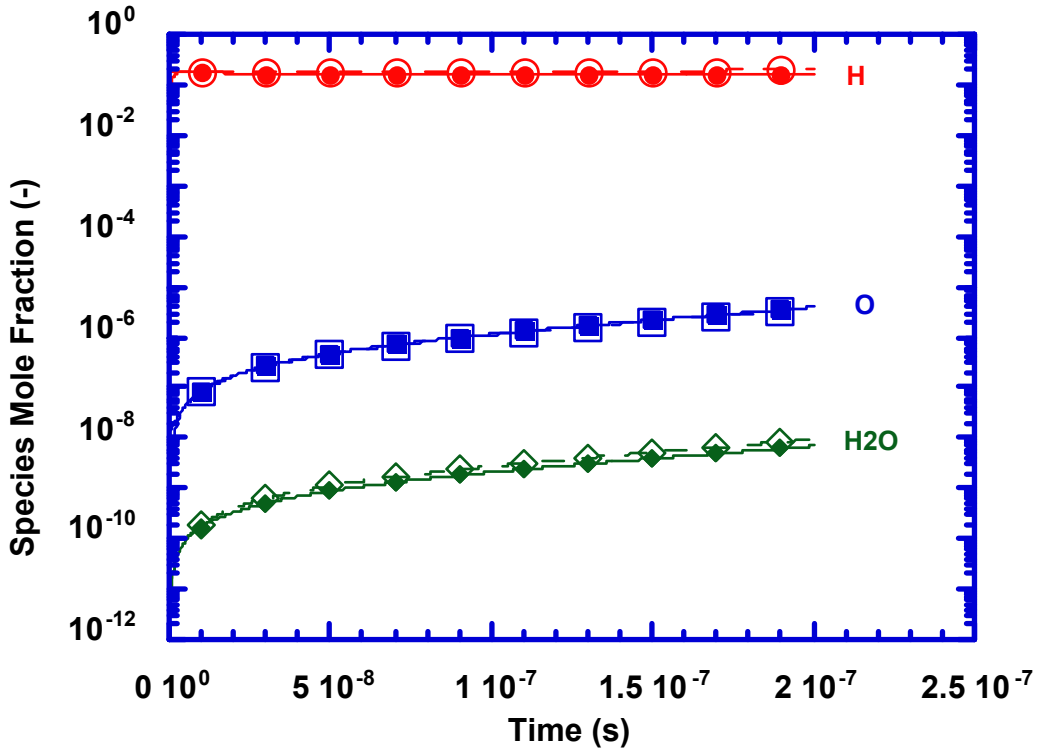

Figure 42b. Comparison of the rates of formation of H, O, and H2O for ϕ = 0.6, 42 bar, and 5000 K plasma temperature (filled symbols: elementary plasma kinetics; open symbols: reduced plasma kinetics).

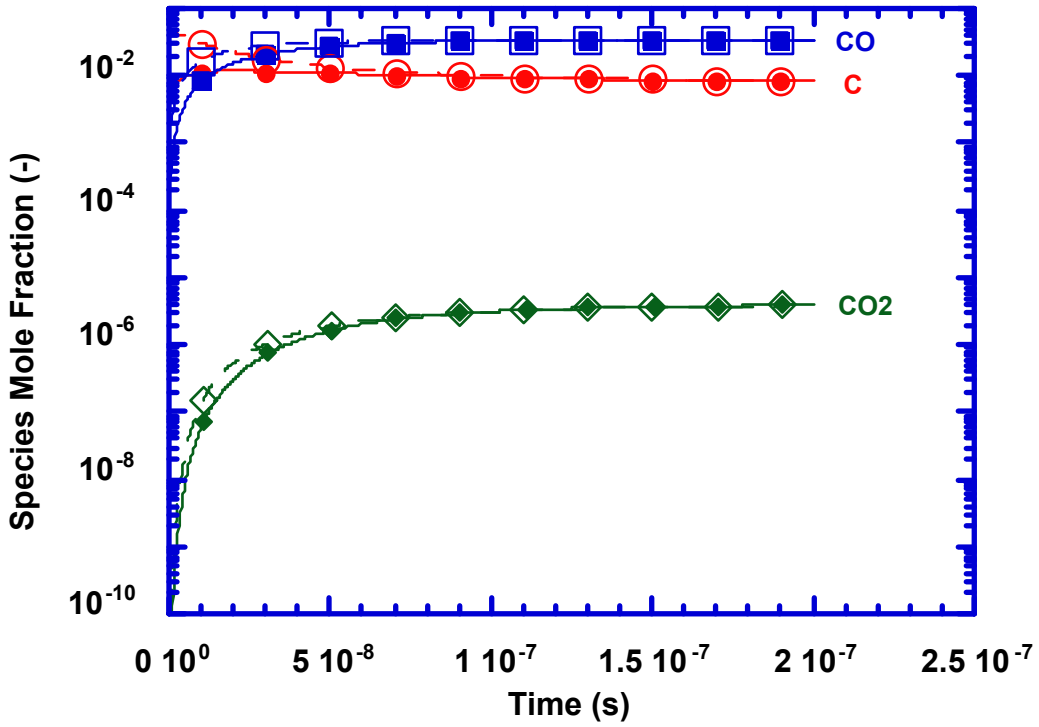

Figure 42c. Comparison of the rates of formation of C, CO, and CO2 for ϕ = 0.6, 42 bar, and 8000 K plasma temperature (filled symbols: elementary plasma kinetics; open symbols: reduced plasma kinetics).

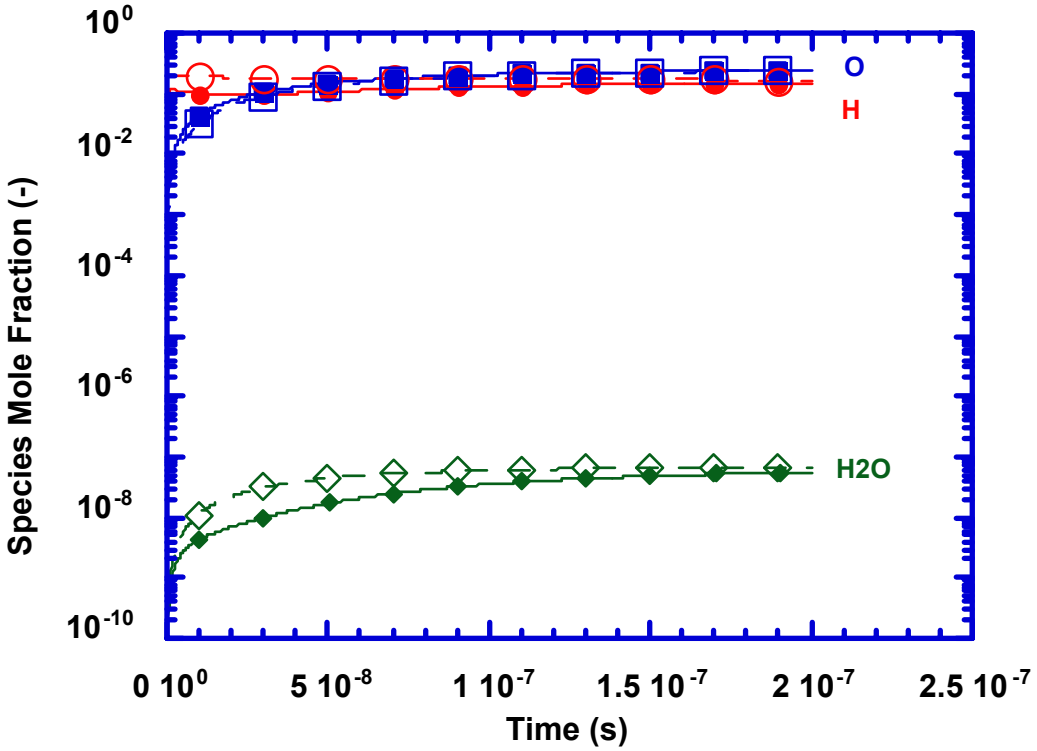

Figure 42d. Comparison of the rates of formation of H, O, and H2O for ϕ = 0.6, 42 bar, and 8000 K plasma temperature (filled symbols: elementary plasma kinetics; open symbols: reduced plasma kinetics).

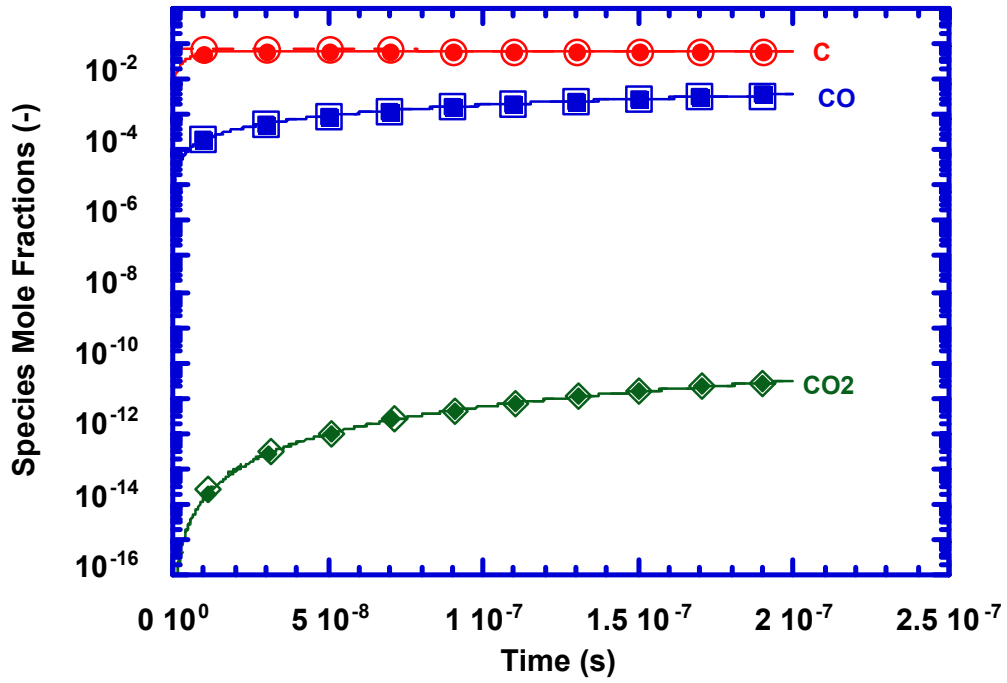

Figure 43a. Comparison of the rates of formation of C, CO, and CO2 for ϕ = 1.0, 6 bar, and 5000 K plasma temperature (filled symbols: elementary plasma kinetics; open symbols: reduced plasma kinetics).

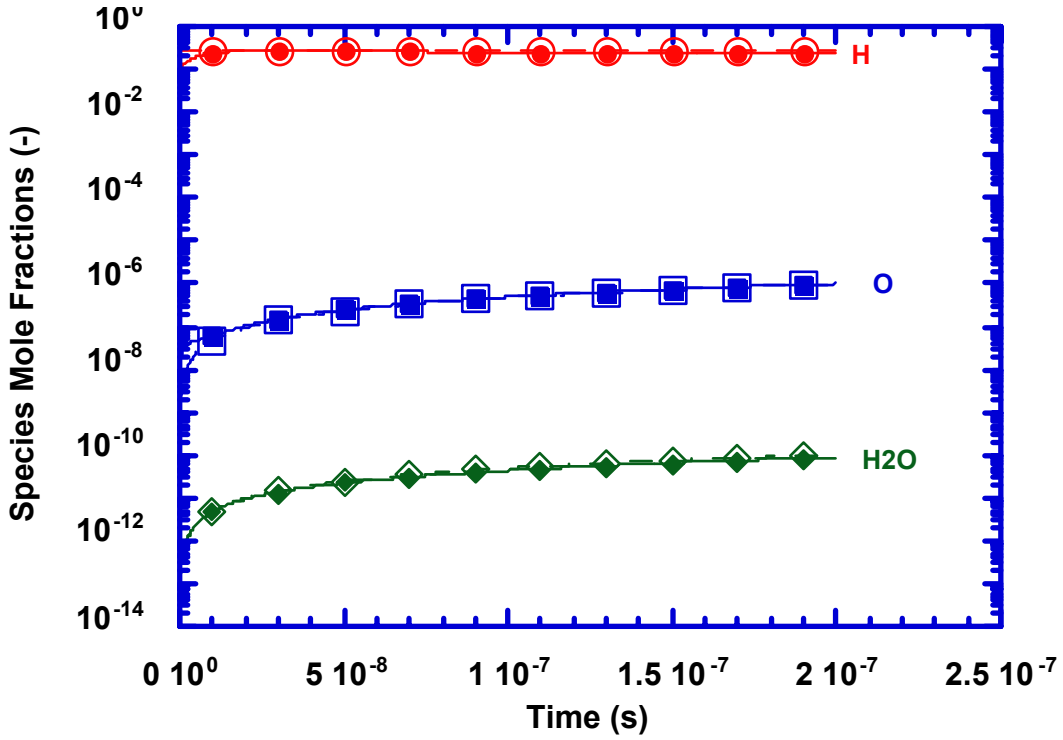

Figure 43b. Comparison of the rates of formation of H, O, and H2O for ϕ = 1.0, 6 bar, and 5000 K plasma temperature (filled symbols: elementary plasma kinetics; open symbols: reduced plasma kinetics).

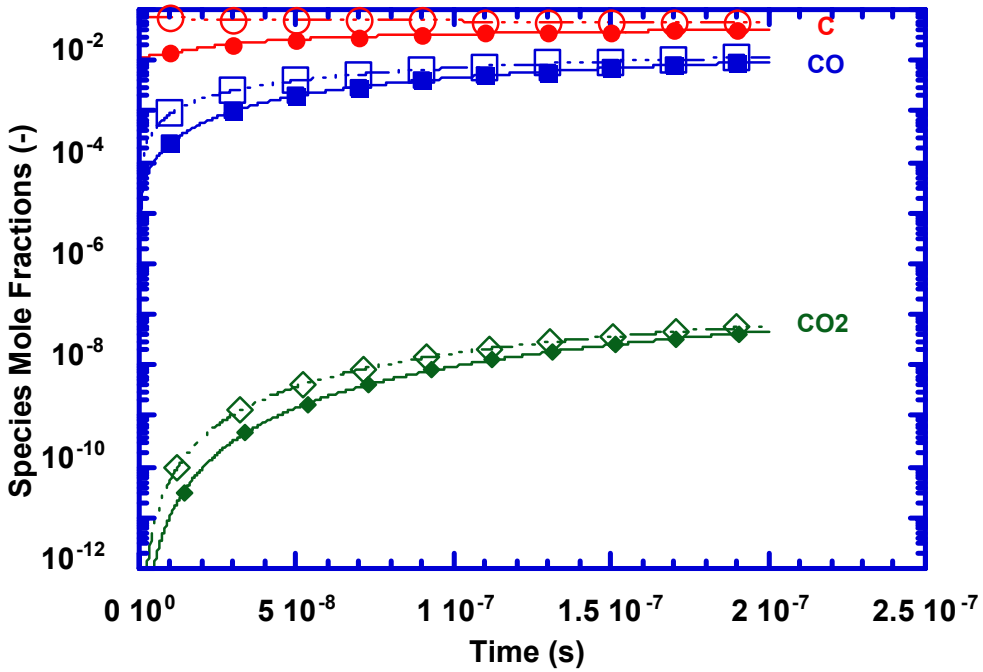

Figure 43c. Comparison of the rates of formation of C, CO, and CO2 for ϕ = 1.0, 6 bar, and 8000 K plasma temperature (filled symbols: elementary plasma kinetics; open symbols: reduced plasma kinetics).

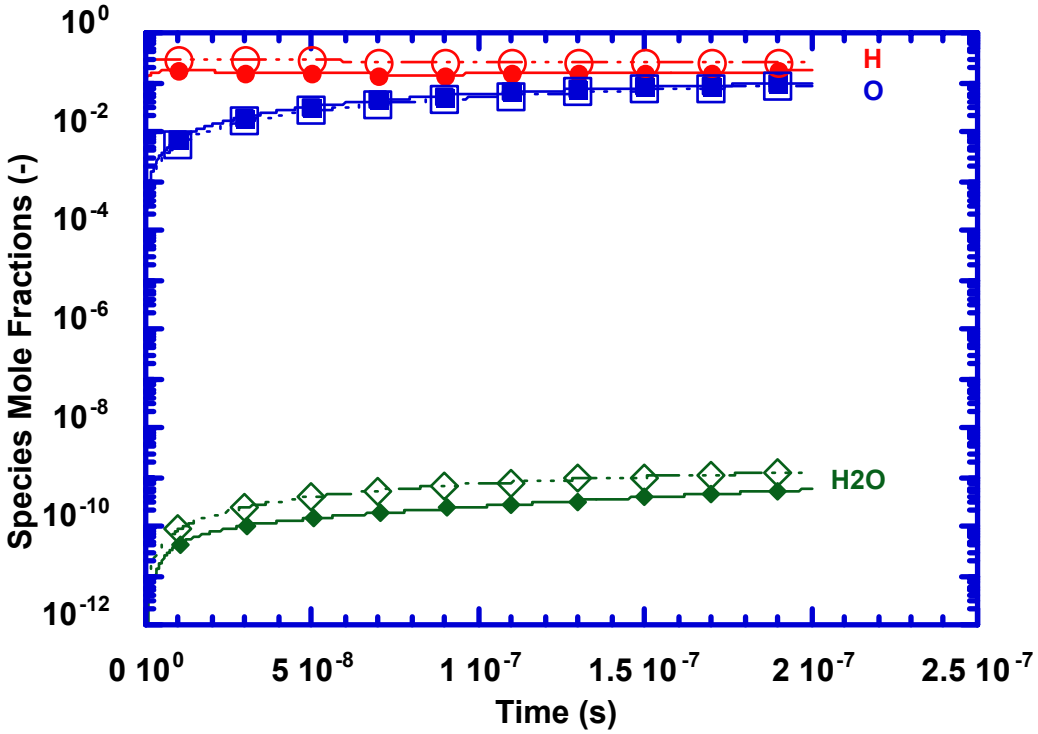

Figure 43d. Comparison of the rates of formation of H, O, and H2O for ϕ = 1.0, 6 bar, and 8000 K plasma temperature (filled symbols: elementary plasma kinetics; open symbols: reduced plasma kinetics).

Because the temperature changes rapidly during the electrical energy deposition process, there is insufficient time for the reactions to reach equilibrium. However, additional confidence in the accuracy of the simplified plasma kinetics mechanism is obtained if the reduced plasma kinetics predict the correct values at steady state, when equilibrium occurs. Figures 44a-44d compare the equilibrium mole fractions with those predicted by the reduced plasma kinetics at long times, when the concentrations have reached constant levels. For many of the cases, there is a small discrepancy at 3000 K, when the effects of flame chemistry are also important. Also, at the higher temperatures, the predictions for CO2 and H2O are not strong. However, the mole fractions for these species are small at these temperatures. Thus, this discrepancy is due to the effects that small errors in predicting species with much higher concentrations have on the predictions of species with very small concentrations, like CO2 and H2O. However, it must be noted that the errors in predicting CO2 and H2O at the higher temperatures are not expected to be important for two reasons. First, because the concentrations are very small, the energy release predictions should not be significantly affected. Second, as noted previously, the plasma reactions do not have sufficient time to reach equilibrium, so rate predictions are much more important than steady state predictions.

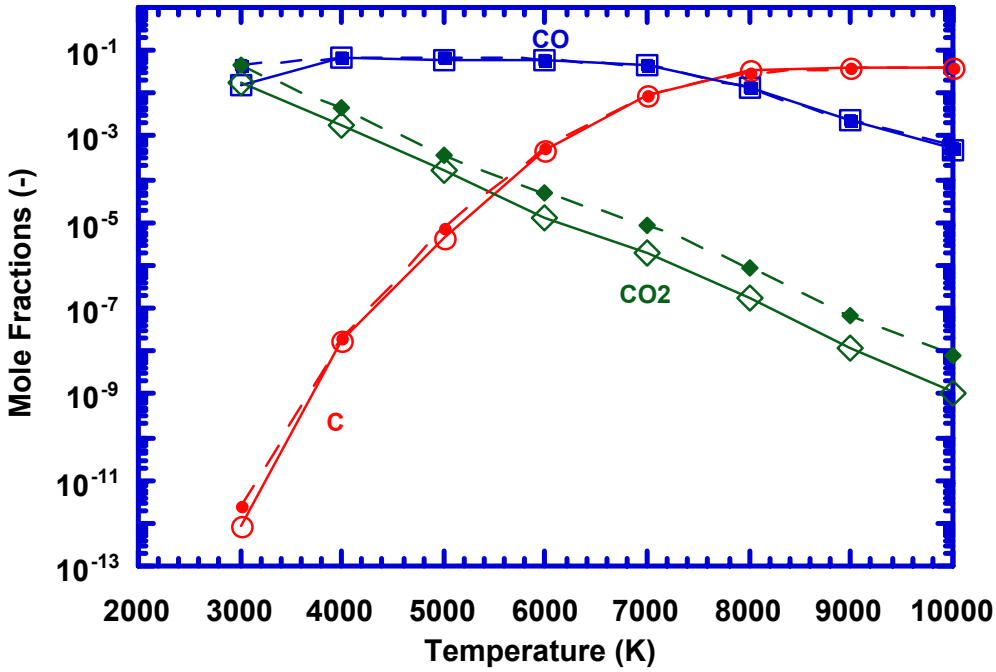

Figure 44a. Comparisons, at 6 bar, of the equilibrium mole fractions (filled symbols) with those predicted at steady state using the reduced plasma mechanism (open symbols): the important carbonaceous species.

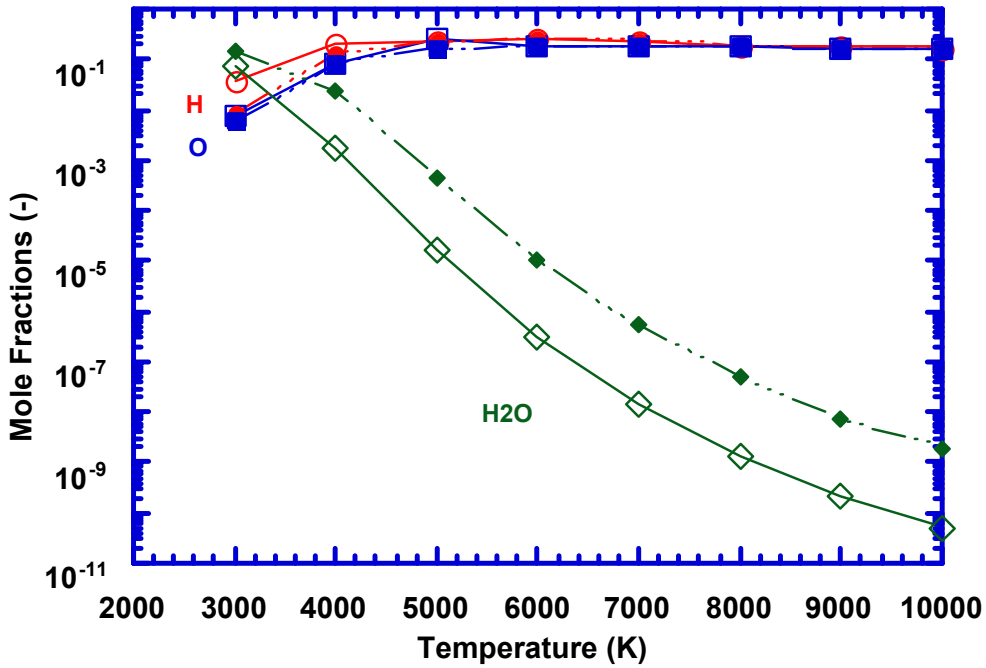

Figure 44b. Comparisons, at 6 bar, of the equilibrium mole fractions (filled symbols) with those predicted at steady state using the reduced plasma mechanism (open symbols): H, O, and H2O.

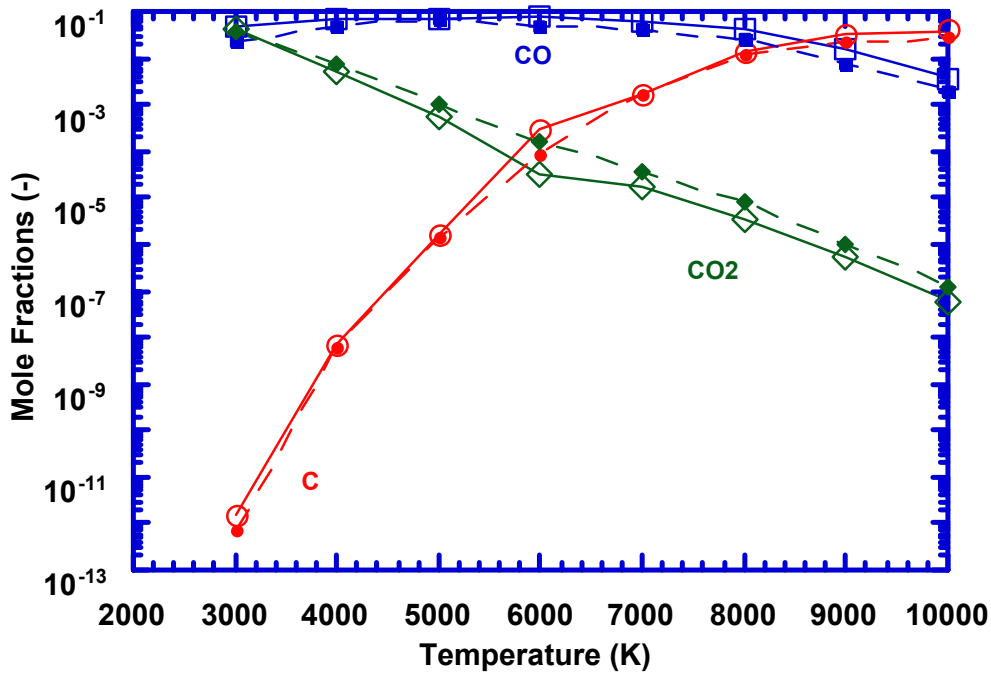

Figure 44c. Comparisons, at 42 bar, of the equilibrium mole fractions (filled symbols) with those predicted at steady state using the reduced plasma mechanism (open symbols): the important carbonaceous species.

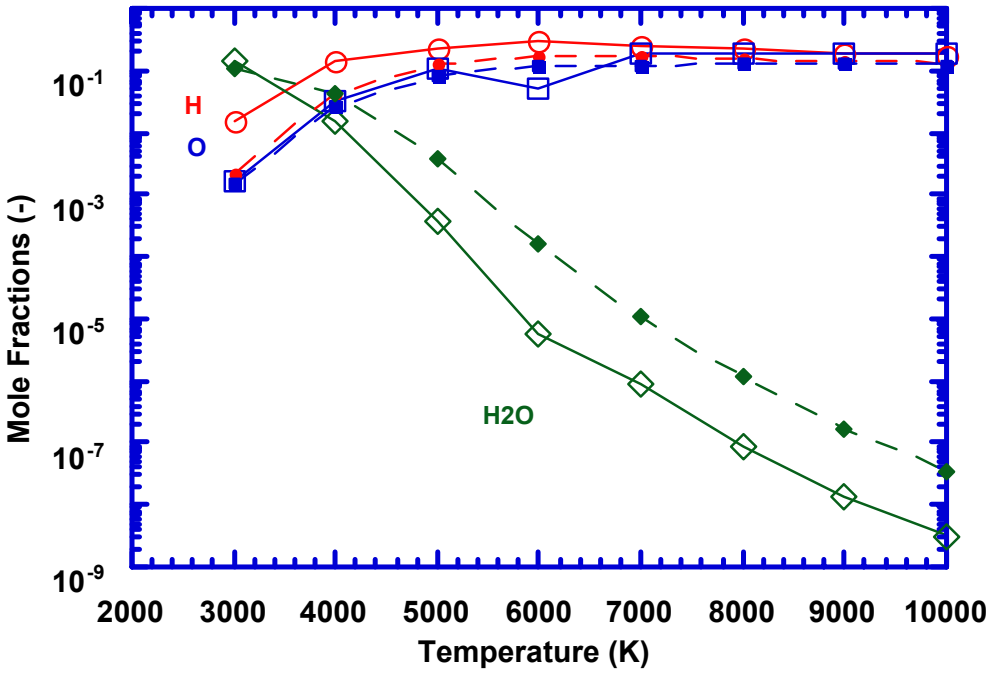

Figure 44d. Comparisons, at 42 bar, of the equilibrium mole fractions (filled symbols) with those predicted at steady state using the reduced plasma mechanism (open symbols): H, O, and H2O.

The simplified flame chemistry developed for this project is listed in Table 9. This simplified mechanism was obtained from Miyamoto and coworkers (1990) and modified by Seers to attain agreement with the detailed mechanism. For each reaction in Table 9, the reverse rate is specified independently rather than relying on the relationship between the forward rate, the reverse rate, and the equilibrium constant for the reaction. This is typical for simplified kinetics schemes, since the simplified reactions are not elementary and thus are not necessarily expected to proceed to equilibrium. The simplified flame chemistry only adds 4 species (H2, HCO, CH3, and CH2O) to those that are already accounted for via the simplified plasma chemistry. Thus, the total number of species considered is only 15 for both types of reactions combined. Because the computational time requirement typically scales with the square of the number of species in the kinetics mechanism (Westbrook and Dryer, 1984), the simplified plasma plus flame kinetics developed for this project should be about 12 times faster than would be possible using elementary kinetics.

Normally, predictions for simplified flame chemistry are validated via comparisons against experimental data for the unstretched laminar flame speed. However, no data were found in the literature for conditions typical of large bore natural gas engines (42 bar and 695 K at the time of spark, and higher pressures and reactant temperatures later during combustion). Therefore, the predictions using the simplified flame chemistry were validated via comparisons against the predictions using GRI-Mech 3.0. Here, it should be noted that the GRI mechanism was developed for flame temperatures from 1000-2500 K, equivalence ratios from 0.1-5.0, and pressures from 10 torr to 10 bar. For application to turbocharged natural gas engines, we are interested in higher pressures at the time of ignition and throughout combustion. However, the developers of GRI-Mech 3.0 were careful to fully account for the pressure fall-offs. Therefore, it is believed that the predictions using GRI Mech 3.0 for high pressures are reasonably accurate. Figure 45 shows the comparison between the predictions of GRI-Mech 3.0 and the simplified kinetics for 42 bar and a reactant temperature of 695 K. The predictions using the simplified kinetics are accurate within 4% for this range of equivalence ratios.

Table 9. Simplified Flame Reactions and Corresponding Rate Data.

Reaction	A (cm, gmole, s)	m (-)	Ea (cal/gmole)	
CH4 -> CH3 + H	1.40*E17	0.0	88400	(RX 8'f)
CH3 + H -> CH4	2.84*E11	1.0	-19510	(RX 8'b)
CH3 + O2 -> CH2O + OH	6.92*E11	0.0	4530	(RX 9'f)
CH2O + OH -> CH3 + O2	7.21*E11	0.0	58050	(RX 9'b)
CH3 + OH -> CH2O + H2	4.00*E12	0.0	0	(RX 10'f)
CH2O + H2 -> CH3 + OH	1.20*E14	0.0	71720	(RX 10'b)
CH2O + OH-> HCO + H2O	5.40*E14	0.0	6300	(RX 11'f)
HCO + H2O -> CH2O + OH	1.87*E14	0.0	36120	(RX 11'b)
HCO + OH -> CO + H2O	1.00*E14	0.0	0	(RX 12'f)
CO + H2O -> HCO + OH	2.80*E15	0.0	10510	(RX 12'b)
CO + O -> CO2	5.90*E15	0.0	4100	(RX 13'f)
CO2 -> CO + O	5.50*E21	-1.0	131800	(RX 13'b)
H + O2 -> O + OH	2.20*E14	0.0	16790	(RX 14'f)
O + OH -> H + O2	1.74*E13	0.0	677	(RX 14'b)

H + OH -> H20	2.20*E22	-2.0	0	(RX 6'f)
H2O -> H + 0H	7.42*E28	-3.0	122600	(RX 6'b)
CO + OH -> CO2 + H	3.7*E11	0	699	(RX 7'f)
CO2 + H -> CO + OH	1.0*E14	0	24244	(RX 7'b)
O2 + M -> 2O + M	3.61*E18	-1.0	118800	(RX 3'f)
2O + M -> O2 + M	3.01*E15	-0.5	0	(RX 3'b)
H + O = OH	5.0*E17	-1.0	0	(RX 5')

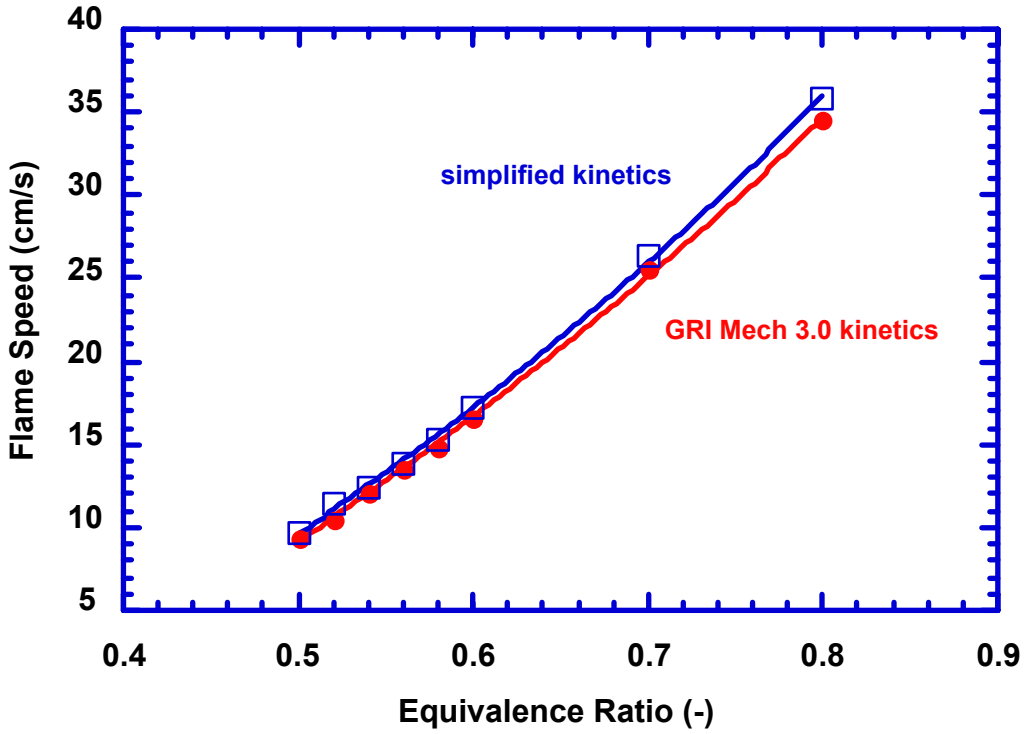

Figure 45. Comparison of predictions of the unstretched laminar flame speed at 42 bar, 695 K reactant temperature for two kinetics mechanisms as a function of equivalence ratio.

3.3. Models for Spark Evolution from a Spark Plug

Three different models for the spark ignition process were developed. Each has its own assumptions and simplifications, as discussed below. First, we developed Model 1, 'Simple Flow with Chemistry' (SFC), which simulates the effect of breakdown power/energy on spark kernel formation during the breakdown phase. This is important because the radial extent of the plasma kernel affects the subsequent flame propagation. As discussed in Subsection 3.3.A., this model was used to predict the effects of equivalence ratio and breakdown energy on the subsequent flame propagation. Subsequently, we developed Model 2, 'Complex Flow in Inert gases' (CFI), to evaluate the assumptions about the fluid mechanics in Model 1. Model 2 shows the effects of recirculation and mixing which affect the temperature distribution. The CFI model is discussed in Subsection 3.3.B. The most comprehensive model that we developed, as discussed in Subsection 3.3.C, was a 3-dimensional simulation of the spark ignition process.

Fully compressible equations that express conservation of mass, momentum, and energy can be written as:

$$\frac{\partial \rho}{\partial t} + \nabla \cdot \left(\rho \vec{V} \right) = 0 \tag{17}$$

$$\frac{\partial \left(\rho \vec{V} \right)}{\partial t} + \nabla \cdot \left(\rho \vec{V} \vec{V} \right) = -\nabla P \tag{18}$$

$$\frac{\partial E}{\partial t} + \nabla \cdot \left(E \vec{V} \right) = -\nabla \cdot \left(\vec{V} P \right) + \nabla \cdot \left(k \nabla T \right) + \dot{q}'''_{ch} + \dot{q}'''_{el} \tag{19}$$

These are the usual equations for an inviscid, heat-conducting fluid with additional terms in the energy equation for chemistry and current flow related to heat sources. The species equation is given as:

$$\frac{\partial \left(\rho Y_i \right)}{\partial t} + \nabla \cdot \left(\rho \vec{V} Y_i \right) - \nabla \cdot \left(\rho D_i \nabla Y_i \right) = \dot{\omega}_i \tag{20}$$

The total energy per unit volume in Equation 19 is defined as:

$$E = \rho \left[e + \frac{1}{2} (\vec{V} \vec{V}) \right] \tag{21}$$

Constitutive relations (thermal and caloric equations of state) are needed to close the system of equations. Therefore, with the assumption of ideal gas behavior of the plasma:

$$P = \sum \left(Y_i / M_i \right) \rho R T \tag{22}$$

$$e = \int C_v dT \tag{23}$$

3.3.A. *Model 1: Simple Flow with Chemistry*

In this one-dimensional model, spark ignition is simulated using simplified fluid mechanics with reduced chemistry for a propane-air mixture. In this case, propane was chosen to allow comparison with available ignition kernel data; as discussed later. This model is easily modified to simulate natural gas as the fuel. A blast wave is initiated in the early stages of breakdown associated with the very large electrical-to-thermal power input. Since at this time (tens of nanoseconds) the plasma in the spark channel has not expanded yet, the pressure and the temperature within the spark kernel attain values on the order of tens to hundreds of times the ambient values, depending upon the spark circuit characteristics.

To simulate the spark discharge physics correctly, it is essential to include the effect of pressure variations in the spark kernel by solving the full set of governing equations (Equations 17-23). However, modeling a blast wave in Eulerian coordinates is challenging due to the spatial resolution required to resolve the shock wave. Thus, in this simplified flow model, the similarity solution to the blast waves was modified and incorporated in the solution for Model 1. The blast wave problem originally formulated by Sedov (1959) has been investigated extensively with various solution techniques. The pressure variation as a function of time and spatial coordinate is specified as a part of the similarity solution. Accordingly, the shock wave position and properties are specified. These similarity results are used with the equation of state and the conservation equations to specify the local thermodynamic state.

In Model 1, we assumed, as have some prior researchers, that the early shock formation processes have little impact on the development of the spark kernel. Typically, it is argued that the flow pressure effects have decayed at moderate (chemical kinetic) time scales following discharge; certainly, at early times the flow is dominated by strong pressure waves.

If at later times the pressure gradients are negligible, then the velocity is mainly prescribed by electrical energy deposition, chemical heat release, and thermal diffusion effects. It would thus be reasonable to neglect the pressure gradient appearing in the momentum equation and to solve the system of equations in the Low Mach Number limit (e.g., Frendi and Sibulkin, 1990). The validity of these assumptions was examined via Model 2, as discussed in Subsection 3.3.B.

To obtain the numerical solution for Model 1, the governing equations were discretized using a control volume formulation assuming cylindrical symmetry of the spark channel. The radial distance of 2 mm was divided into 200 cells with a grid spacing of 10 μm along the radial axis (the z=0 line in Figure 46). Time-steps taken ranged from 0.01 ns for the early stages to 0.1 μs at the end of the glow discharge phase, and were sufficiently small to model chemical kinetics. For the present model, thermodynamic properties were calculated using statistical thermodynamics. The transport properties for the plasma were obtained from curve fits to plasma data presented by Sher and coworkers (1992).

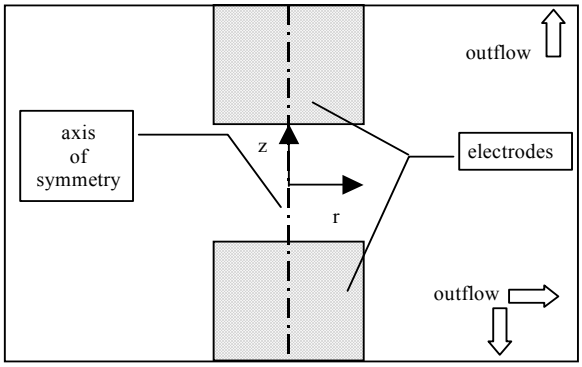

Figure 46. Computational domain and spark plug electrode geometry.

3.3.A.1. Initial and Boundary Conditions (Model 1)

In most of the computational models presented in the literature, simulations generally start just after the end of spark discharge using initial conditions that are derived from a simplified energy balance. This technique for specifying the initial conditions may result in significant errors. However, since the model presented here starts at the beginning of breakdown, the initial conditions for the present simulations are ambient (e.g., a uniform temperature of 300 K and pressure of 1 bar for the cases examined later). Boundary conditions are defined by setting the temperature and the species gradients equal to zero at the axis of symmetry and also at the outflow boundary.

3.3.A.2. Chemical Kinetics Mechanism and Ionization (Model 1)

Rather than using the simplified plasma model discussed above, at this stage of model development we used a two-step reaction mechanism for propane taken from Westbrook and Dryer (1981). As compared to the model by Kravchik et al. (1995), the reaction mechanism used is extremely simple, which provides computational simplicity and a reduced computational time burden. The reaction rate for dissociation of nitrogen was taken from Sloane (1990). The reactions for the combined three-step mechanism are:

$$C_3H_8 + 3.5O_2 \rightarrow 3CO + 4H_2O \qquad \text{(RX 1")}$$

$$CO + 0.5O_2 \leftrightarrow CO_2 \qquad \text{(RX 2")}$$

$$N2 + M <-> N + N + M \qquad \text{(RX 3")}$$

The reaction rates are given by:

$$\begin{aligned}
\dot{\omega}_1 &= 1.0E12[C_3H_8]^{0.1}[O_2]^{1.65}\exp\left(\frac{-30.0}{RT}\right) \\
\dot{\omega}_{2f} &= 4.0E14[CO][H_2O]^{0.5}[O_2]^{0.25}\exp\left(\frac{-40.0}{RT}\right) \\
\dot{\omega}_{2b} &= 5.0E8[CO_2]\exp\left(\frac{-40.0}{RT}\right) \\
\dot{\omega}_{3f} &= 1.55E18\cdot T^{0.62}[N_2]\exp\left(\frac{-226.1}{RT}\right) \\
\dot{\omega}_{3b} &= 2.0E16\cdot T^{0.64}[N]^{2.0}
\end{aligned} \qquad (24)$$

The subscripts f and b represent the forward and backward reactions, respectively, and the units are in cm-sec-mole-kcal-Kelvin.

It is necessary to include ionization to assure the correct amounts of energy absorption and release in physically realistic time scales. Ionization of atomic nitrogen is the only such reaction considered in this part of the study. The composition of N^+ for a given temperature and pressure is calculated by assuming equilibrium distributions. Consider a general reaction,

$$A_i \leftrightarrow A_{i+1} + e^- - u_i \qquad (25)$$

where A_i is the i^{th} level of ionized particle, and u_i is the ionization energy. The equilibrium constant for this reaction is given by Cambel (1963):

$$K_{i+1} = \frac{n_{i+1}n_e}{n_i} = \upsilon\left(\frac{2\pi m_e kT}{h^2}\right)^{3/2}\frac{2Z_{i+1}Z_e}{Z_i}e^{-u_i/kT} \qquad (26)$$

This equation is known as the Saha equation and the values of the partition functions (Z) are taken from Drellishak and coworkers (1965).

3.3.A.3. Results (Model 1)

In a typical calculation, a breakdown power of 200 kW is deposited into a spark channel with a diameter of around 40 μm within a time period of 20-40 ns (Maly, 1984). Power delivered during the glow phase is approximately 30 W. It should be noted that the flame radius is defined in the following results as the region where the temperature is above 1000 K. This threshold was used because high temperature kinetics (flame chemistry) begins to dominate at this temperature. The temperature distribution at different times is shown in Figure 47 for a glow power input of 28 W. Similar to Kravchik et al. (1995), the model presented here predicts temperatures ranging from 5500 K to 6500 K near the core of the plasma kernel for a time period of 10 μs to 100 μs. Higher temperatures than those computed by Kravchik et al. are shown at a time of 1 μs. This could be because of a time lag between the time specified here for this study and their study, which was initialized using experimental results. A noticeable difference occurs post-glow, after 100 μs, where they show a more pronounced temperature decay than the present model.

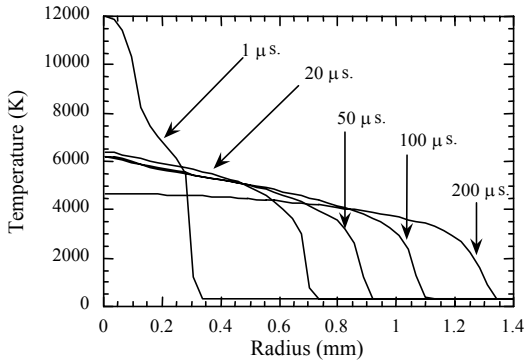

Figure 47. Temperature distribution at different times.

The distribution of nitrogenous species, considering only the first ionization, is presented in Figure 48 for the results at the end of breakdown. These results are in very good agreement with those presented by Sher et al. (1992).

In Figure 49, the flame kernel and blast wave radius curves predicted by Model 1 are compared to Maly's experimental results (Maly, 1984). The predicted result was obtained using a 200 kW breakdown/arc power maintained over a time consistent with the peak temperature attaining a value of 40,000 K. The values of the breakdown/arc time, 20 ns, and the energy deposited, 4 mJ, are consistent with Maly's values.

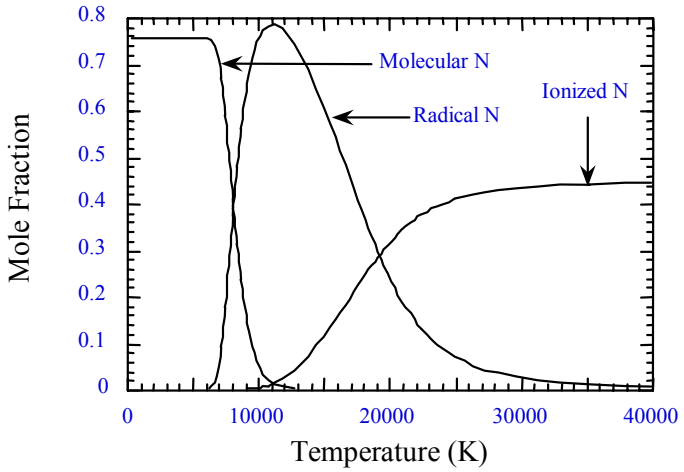

Figure 48. Nitrogen species distributions at the end of the breakdown phase.

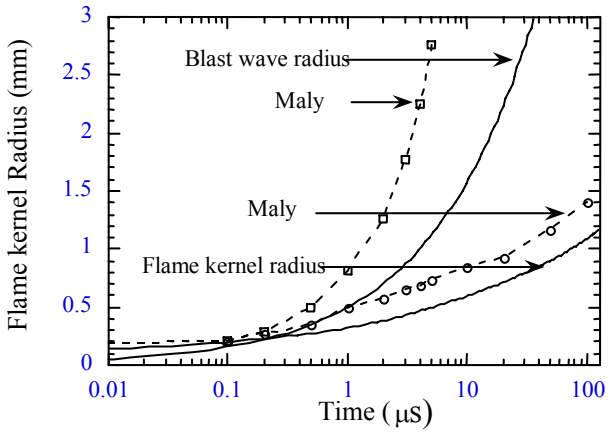

Figure 49. Experimental and predicted, via Model 1, flame kernel and blast wave radii.

The computational results show the same trends as the experimental ones. While there is a significant disagreement observed in the blast wave radius, the flame kernel radius is only approximately 20% different from Maly's results (Maly, 1984) at 100 μs. The surprisingly good agreement with the flame kernel radius suggests that the blast wave has lost most of its effect and errors in its trajectory do not affect the computation of the kernel properties. We will explain why this effect occurs in later results when we use Model 2 to calculate the flow.

To observe the effects of energy deposition at different stages of the spark discharge on flame kernel growth, different values of glow power were used as inputs. For a time period of 100 μs, glow energies of 1.75 mJ, 2.8 mJ, and 5 mJ were given as inputs to the computational model and the results obtained are provided in Figure 50. The results show reasonably good agreement with those presented by Kravchik et al. (1995). Increasing energy input results in an increased rate of flame kernel expansion that also can be attributed to higher reaction rates caused by higher temperatures. It is important to note that the effect of varying energy input on the flame kernel is not pronounced up to a time of approximately 10 μs.

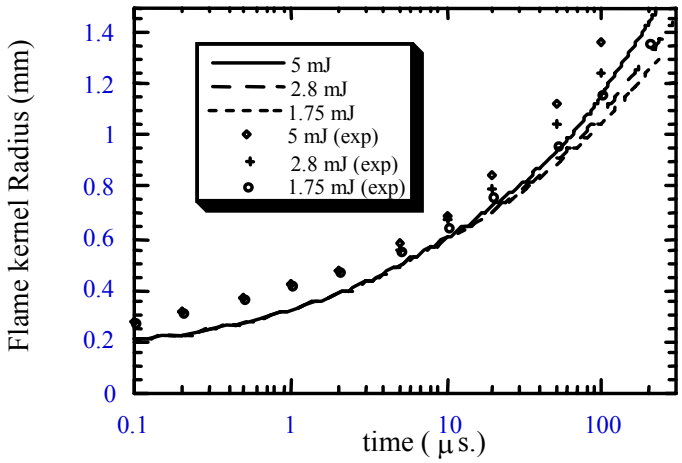

Figure 50. Predicted (using Model 1) and experimental variation of flame kernel radius for various arc/glow energies.

The effect of equivalence ratio on the flame kernel radius was also investigated and these results are presented in Figures 51a and 51b. The effect of equivalence ratio on the flame radius is not observed at early times, as shown in Figure 51a. The flame kernel radius becomes larger for stoichiometric mixtures at later times, as can be seen in Figure 51b. Larger flame expansion rates observed for mixtures with ϕ=1 are due to increased reaction rates.

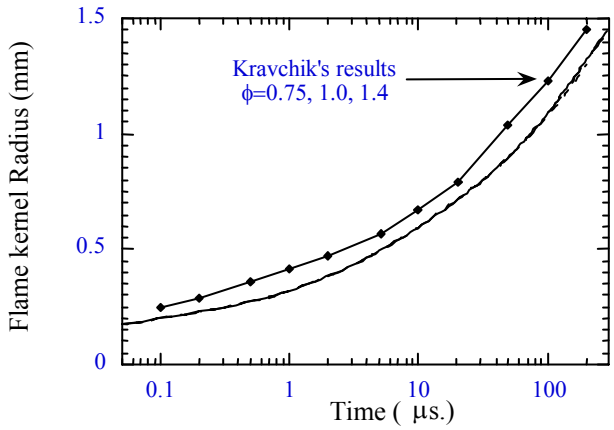

Figure 51a. Predicted (using Model 1) and experimental variation of flame kernel radius with equivalence ratio for times up to O(100 μs).

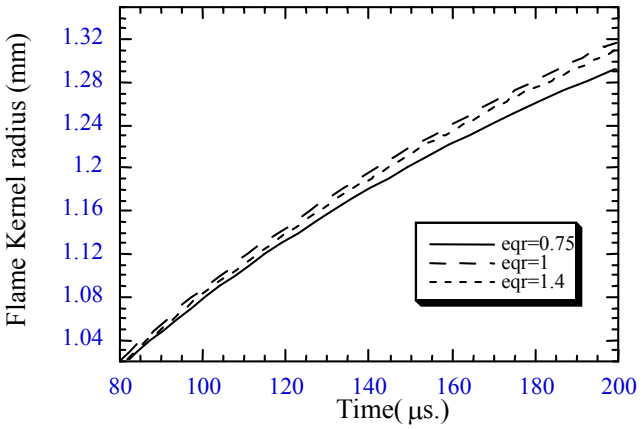

Figure 51b. Predicted variation of flame kernel radius with equivalence ratio for longer time scales.

3.3.B. *Model 2: Complex Flow in Inert Gases*

There is a question as to the ability of one-dimensional modeling to resolve the details of important physics during spark discharge due to "edge" effects (e.g., Akram, 1996). Therefore, we initiated a study of two-dimensional flow effects to gain more physical insight into the phenomena (cf. Figure 46). The spark discharge was simulated by solving the full set of governing equations, Equations 17-19, but without including any chemical reactions. Transport properties, thermal and electrical conductivity for high temperature air based on the data presented in Boulos et al. (1994), were used in the simulations.

The Flux Corrected Transport (FCT) algorithm developed by Boris and coworkers (1993, 1997) was used with some problem-specific modifications to advance all dependent

quantities in time. FCT is a high order, explicit, finite difference code that includes a group of subroutines for solving nonlinear, time-dependent continuity equations. This monotone, conservative, and positivity-preserving algorithm can accurately compute steep gradients, allowing grid scale numerical resolution. Two-dimensional problems are solved by time-step splitting in the different coordinate directions.

3.3.B.1. Electrical Energy Source (Model 2)

Electrical power input to the gas due to resistive heating is given by

$$\dot{q}'''_{el} = \vec{j} \cdot \vec{E} \tag{27}$$

where $\vec{j}$ is the current density and $\vec{E}$ is the electric field. A generalized Ohm's law for an electrically neutral plasma can be written as:

$$\vec{j} = \sigma_e \left(\vec{E} + \vec{u}_e \times \vec{B} \right) \tag{28}$$

With the assumption of a negligibly small magnetic field, and unidirectional flow of the current in the z-direction within the cylindrically symmetric current channel, the Joule heating term is written as:

$$\dot{q}'''_{el} = \frac{j_z^2}{\sigma_e} \tag{29}$$

where σ_e is the electrical conductivity of the plasma, which has a strong temperature dependence. Using total current I, the source term can be distributed over the plasma channel (Thiele et al., 2000) by:

$$\dot{q}'''_{el} = \sigma_e \frac{I^2}{\left(\int 2\pi r \sigma(r,z) dr \right)^2} \tag{30}$$

3.3.B.2. Initial and Boundary Conditions (Model 2)

Arc initiation within the spark gap is achieved with the breakdown of the gases between the electrodes. The duration of the breakdown is on the order of 10 nanoseconds and that period cannot be simulated with continuum models because the gas during this period is not in thermal equilibrium. Therefore, our simulation starts just after the breakdown of air between the electrodes using the conditions at the end of the breakdown as initial conditions. Specific values of the initial conditions used as an input to each simulation will be specified for the relevant result set. Characteristically high-temperature and high-pressure values with the density at the ambient level are used for the current-carrying plasma channel at the initial time (beginning of arc discharge). At the initial time, the gas in the computational domain is assumed to be at rest, resulting in the flow velocity being set to zero everywhere.

Electrodes are treated as walls with slip conditions, and the boundary at r=0 is an axis of symmetry. Outflow boundary conditions are used for the other two boundaries (i.e., the normal components of spatial gradients of dependent variables are set to zero). An adiabatic wall boundary condition is used for the electrodes and this approximation will be discussed later within the results section.

3.3.B.3 Results (Model 2)

To validate our two-dimensional computational model, comparison was made between Model 2, Model 1 (cf. Figure 49), and results presented by Maly (1984). Recall that Model 1 showed significant disagreement in the blast wave radius yet showed reasonable agreement in

the flame kernel radius. In Model 1, because of the one-dimensional approximation, the geometry of the gap does not affect the solution. Obviously, for the two-dimensional case, geometry effects play a significant role. The relevant geometrical parameters are: 1.0 mm spark gap with an electrode radius of 0.5 mm. The initial conditions are 0.12 mm of conducting channel radius with a pressure of 1.01 MPa and a temperature of 35,000 K (Maly, 1984). Note that this is different from Model 1, for which the initial condition was 300 K and power deposition raised the temperature through a modeled breakdown phase. For Model 2, the flame kernel in this pure air simulation was again defined as the region where the temperature is above 1000 K. Both the blast wave and the flame kernel are reasonably predicted with our computation, giving a little larger radius compared to the experiments (see Figure 52). The maximum pressure in the blast wave has decreased to approximately 130 kPa at 5 μs. This confirms the assumption made about pressure effects for Model 1. Strong pressure gradients are no longer present for much of the discharge process. It is important to mention that with these strong initial conditions, further energy deposition (using currents on the order of 1 A) has a negligible effect on the flow physics within the time scales considered here.

In the second set of results, we compared our Model 2 predictions with the simulations of Akram (1996). We used the same initial and boundary conditions for the case of non-tapered electrodes. The initial temperature was set at 10,000 K, and a radius of 0.1 mm was chosen from the range given by Akram (1996) as the initial condition for the plasma channel. The corresponding pressure was calculated using the known density, which is assumed to be at the initial ambient level. The current and calculated energy as functions of time are given in Figure 53. Energy entering the gas during the simulation, calculated from Equation 24, is 11.5 mJ, and is in good agreement with the experimental and calculated values given by Akram (1996): 14 mJ and 12 mJ respectively.

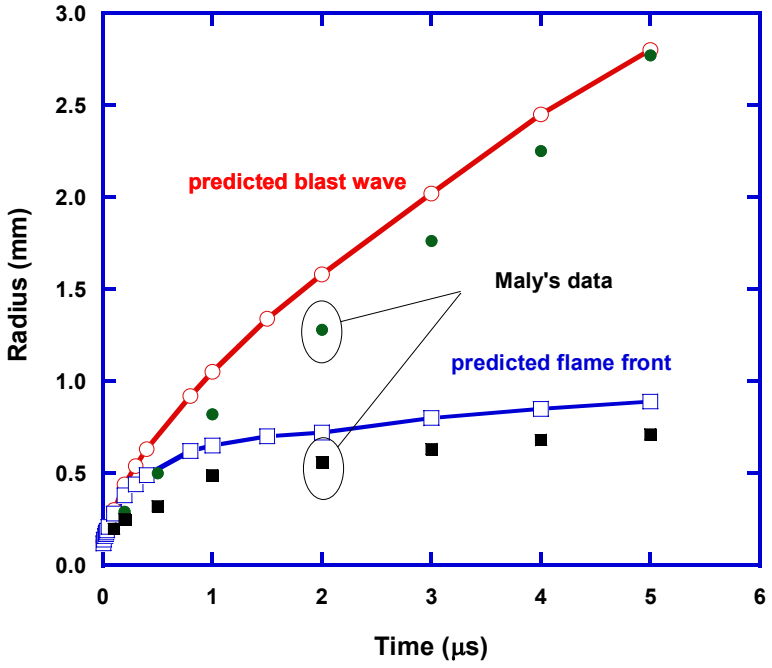

Figure 52. Comparison of the predicted (via Model 2) flame kernel and blast wave radii in air via Model 2 with the experimental results (symbols) from Maly (1984).

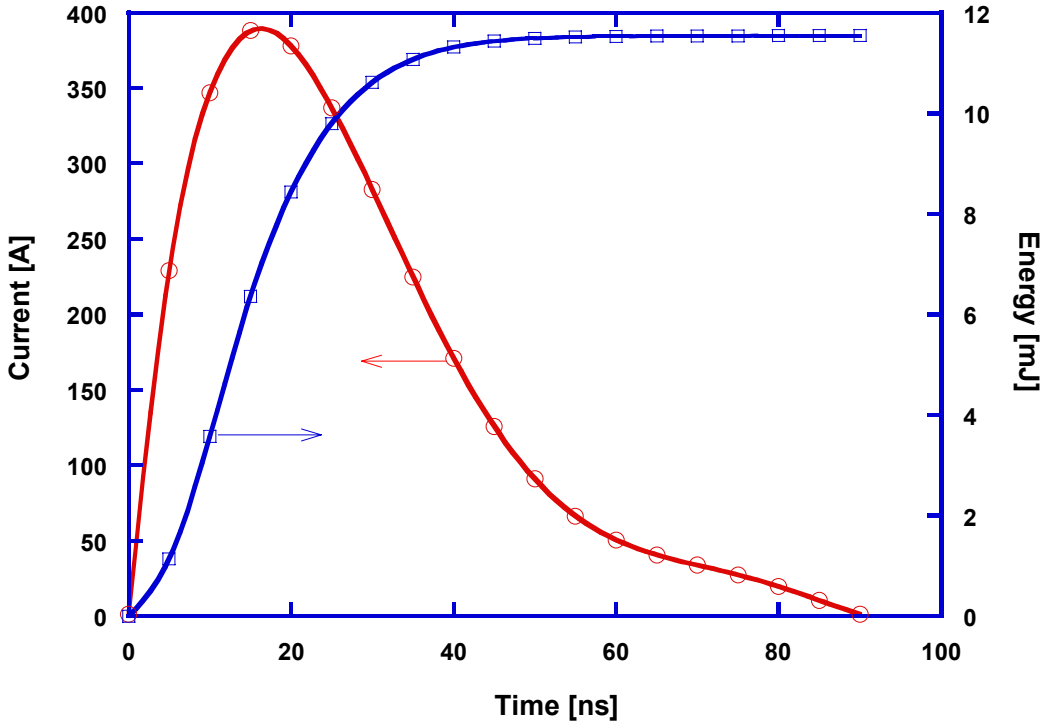

Figure 53. Total current and energy as functions of time.

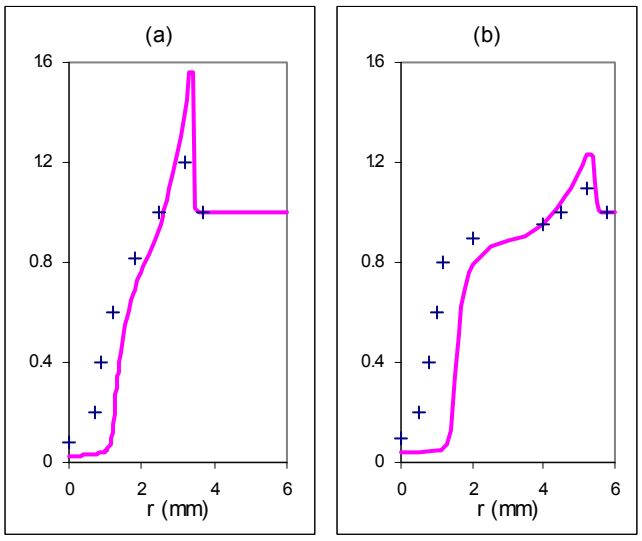

Figure 54. Model 2 predictions of scaled mass density profiles in the z=0 plane at 5 μs (a), and at 10 μs (b); + indicates experimental results from Borghese et al. (1988).

The scaled mass density profiles (normalized by the atmospheric value) in the z=0 plane at 5 and 10 μs are given in Figures 54a and 54b, respectively. It is observed that they match well with both experimental (Borghese et al., 1988) and prior computational (Akram, 1996) results.

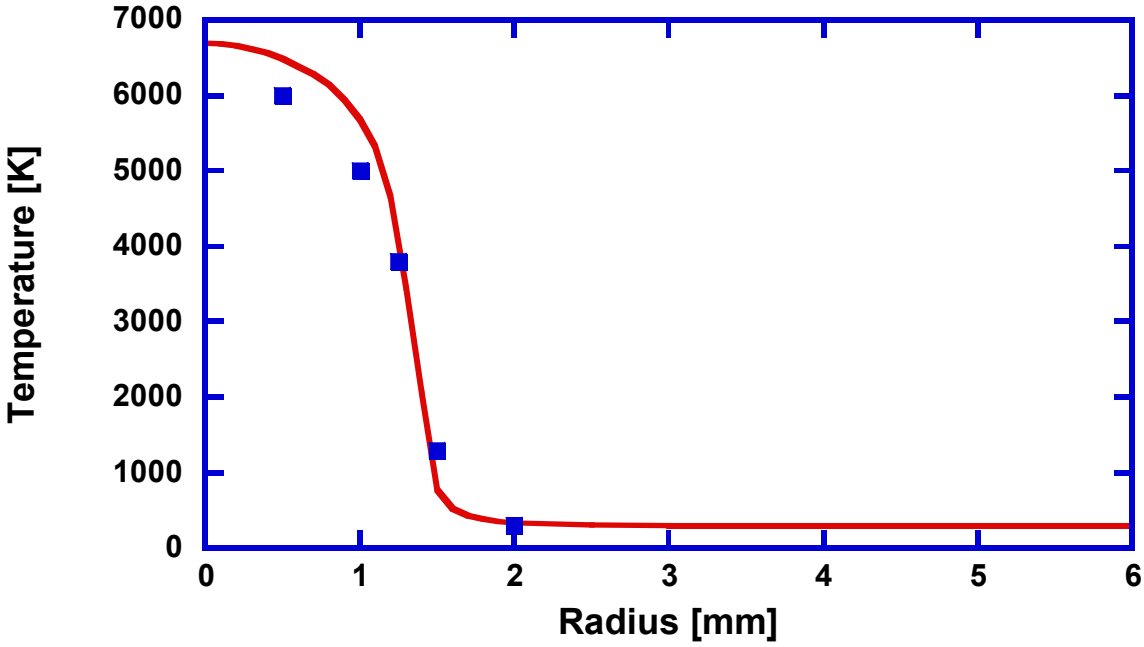

Figure 55. Temperature as a function of radial coordinate at 10 μs for the z=0 plane; symbols are the model predictions of Akram (1996).

As mentioned earlier, our model uses adiabatic boundary conditions for the electrodes. To investigate the effect of this assumption on the solution, the temperature in the z=0 plane is plotted as a function of radius at 10 μs in Figure 55. The results in Figure 55 are both qualitatively and quantitatively in accordance with predictions by Akram (1996), who did NOT assume an adiabatic wall. This indicates that the adiabatic electrode wall approximation is a reasonable assumption within the time scales presented, because heat transfer is slow relative to this time scale. As discussed by Akram (1996), there is a significant difference in peak temperatures near the axis of symmetry between the one-dimensional and two-dimensional computational results. Akram also noted that the convective effects and the heat losses to the electrodes cause this difference. However, our simulation shows that the heat loss to the electrodes has a negligible influence on the solution within these early stages of spark discharge.

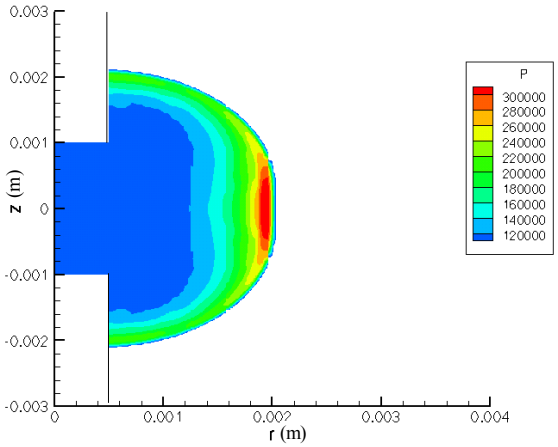

Figure 56. Predicted (Model 2) pressure distribution at 2.0 μs.

Pressure and temperature contours are provided in Figures 56 and 57, respectively, at 2.0 μs. It is seen that the blast wave is growing much faster than the plasma kernel. The pressure in the blast wave is a maximum in the z=0 plane, and decreases toward the electrodes. The plasma kernel is shaped as a consequence of cold gas flow into the gap, and it starts to prevent further growth of the kernel in the radial direction. These results are in accordance with those of Akram (1996).

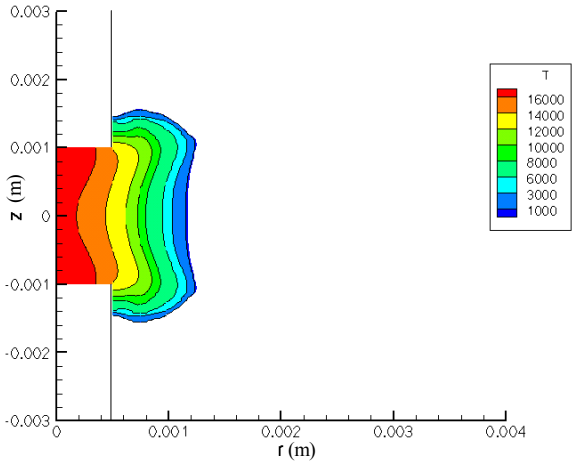

Figure 57. Predicted (Model 2) temperature distribution at 2.0 μs.

Pressure and temperature contours at 5 μs in the computational domain are provided in Figures 58 and 59. The blast wave is still growing although its strength is weakening, as can be seen from the pressure values. It is also important to note that pressures within the gap are lower than atmospheric pressure as a result of sudden and strong expansion. This low-pressure region induces a strong back-flow of the cold gas toward the spark gap. The growth of the plasma kernel is almost stopped at this point and the maximum temperatures within the gap start to decrease rapidly because of the conductive and convective processes within the gas.

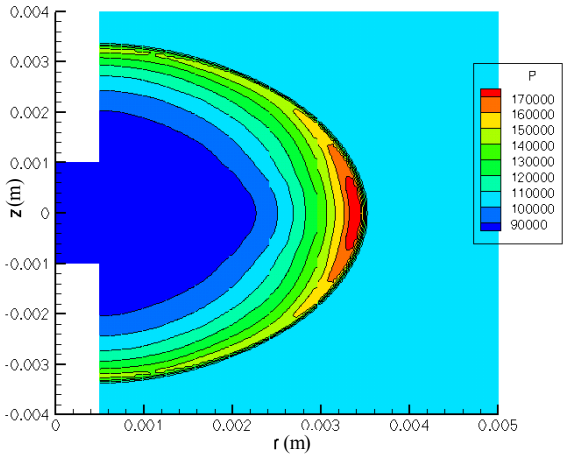

Figure 58. Predicted (Model 2) pressure distribution at 5.0 μs.

The velocity vector field in the computational domain at 5.0 μs is given in Figure 60. It is seen that vortices have already formed near the sharp corners of the electrodes. Also, fresh gas flowing inward along the z=0 plane is visible. Effects of this cold gas movement toward the spark gap and recirculation near the corners of the electrodes will be clearly observed in the temperature contours at later times.

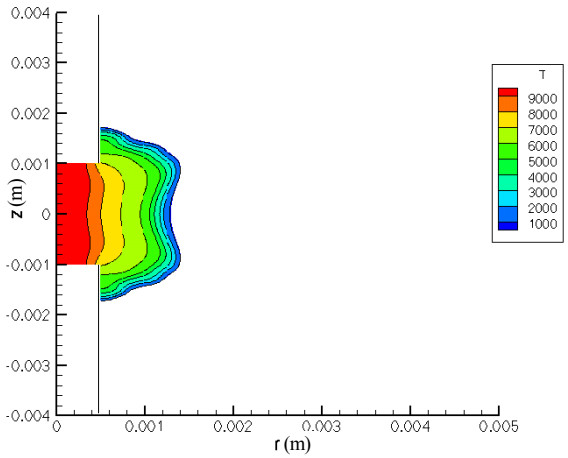

Figure 59. Predicted (Model 2) temperature distribution at 5.0 μs.

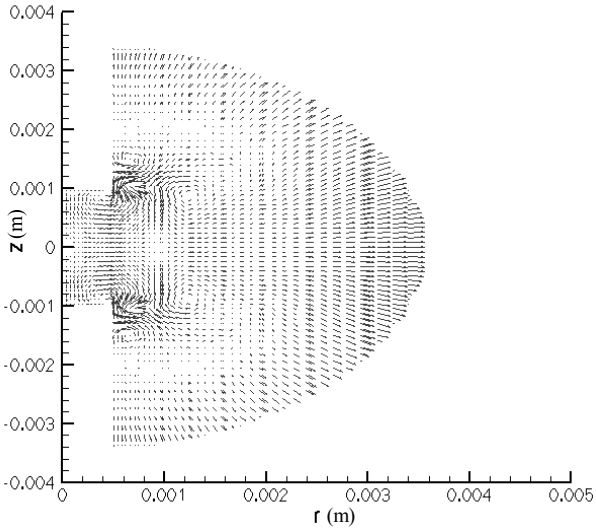

Figure 60. Predicted (Model 2) velocity vector field at 5.0 μs.

Temperature contour and velocity vector field plots at 10 μs are given in Figures 61 and 62, respectively. It is seen that the plasma kernel cannot grow in a spherical shape because of the cold gas inflow near the corners of the electrodes. Two distinct pairs of vortices can be seen in Figure 62, one of which is within the spark gap near the corner, and the other is outside the gap close to the z=0 plane; very similar observations can be found in the results presented by Akram (1996).

At later times, pocket-like high temperature regions are formed as a result of the constant cold gas flow near the electrodes. Figures 63 and 64 show the formation of a high temperature pocket in the computational domain. From the chemical kinetics point of view, a

relevant temperature contour range is assumed from 1000 K to 2200 K. This is similar to the range specified by Akram (1996).

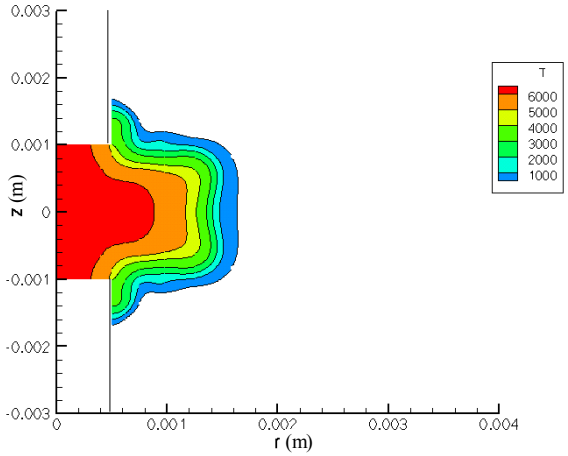

Figure 61. Predicted (Model 2) temperature distribution at 10.0 μs.

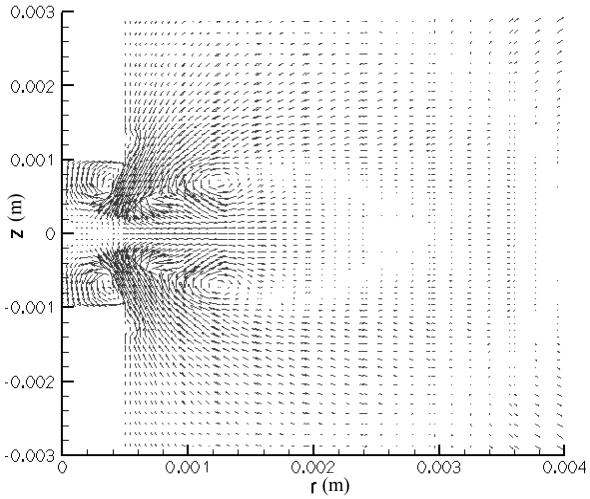

Figure 62. Predicted (Model 2) velocity vector field at 10.0 μs.

These results are in good qualitative agreement with the results by Akram (1996), but the hot temperature pocket formation occurs earlier in our simulation. We believe that this is caused by the existence of stronger inflow with higher velocity magnitudes in our computational results and also because of slightly lower energy deposition compared to Akram.

We ran one more test to demonstrate the effect of including heat conduction within the gas in our computational model on the temperature distribution. The temperature contours at 10 μs are provided in Figure 65 for the flow where heat conduction is neglected within the gas. It is observed that temperatures are significantly higher and a very high temperature core persists compared to Figure 61.

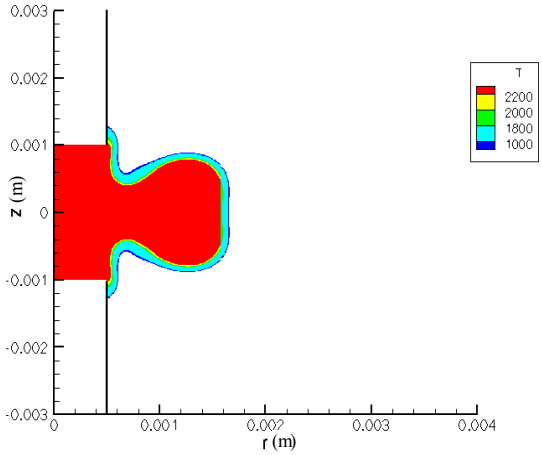

Figure 63. Predicted (Model 2) temperature contour for the assumed ignition range at 15.0 μs.

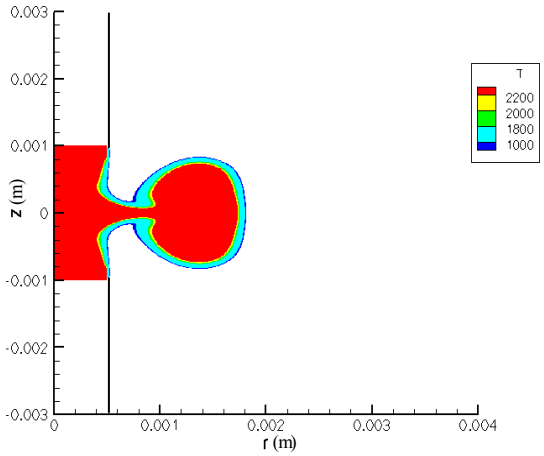

Figure 64. Predicted (Model 2) temperature contours for the assumed ignition range at 20.0 μs.

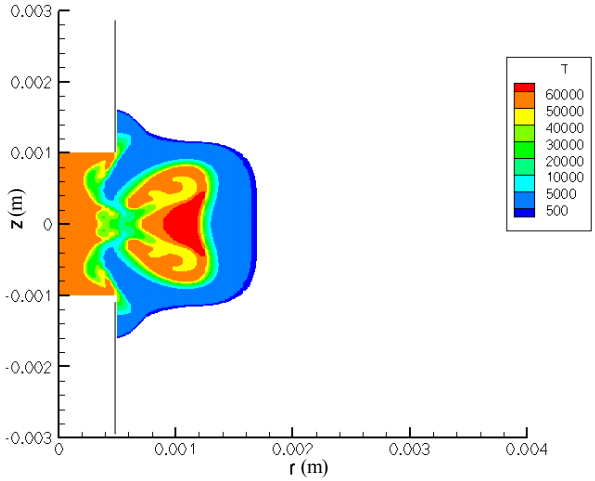

Figure 65. Predicted (Model 2) temperature distribution at 10.0 μs in the absence of conduction.

3.3.C. *3D Spark Ignition Model*

The final model that our research team developed for this project was a three-dimensional model for the spark ignition process. Our primary goal for this model was to examine the effects of flow through the spark gap on the subsequent ignition and flame propagation processes. Flow through the spark gap is of interest because Herweg and Maly (1992) found that the efficiency of electrical-to-thermal energy conversion depends upon the bulk flow through the gap for both arc and glow. This initial version of the 3D model used a simple progress variable to simulate flame growth and did not include the dynamic response of the ignition circuit. The next version of this model, to be generated in the near-term, will incorporate all that we have learned in this project, including plasma kinetics, flame kinetics, and the circuit dynamics. Once completed, this version of the model (i.e., a Fortran code that can be used as a subroutine within an engine modeling code) can be obtained from Prof. Matthews at rdmatt@mail.utexas.edu or Prof. Ezekoye at dezekoye@mail.utexas.edu.

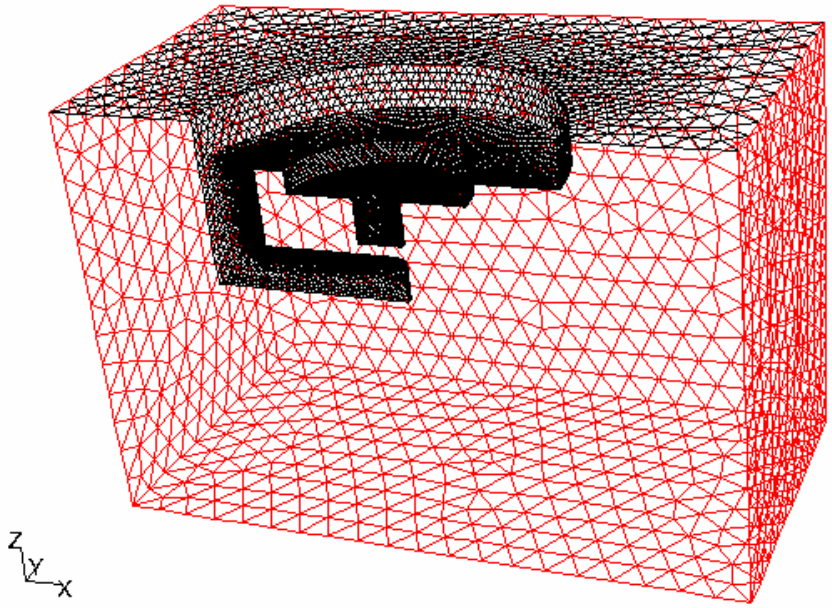

Figure 66a. Overall view of the computational domain for the 3D model.

The computational domain for this model is illustrated in Figures 66a and 66b. The orientation of the spark plug with respect to the x, y, and z axes is shown in Figures 66a and 66b and in each of the figures to be discussed. Because the imposed flow cases have the bulk flow in the z direction, there is an x-z plane of symmetry that is aligned with the center electrode and along the horizontal leg of the ground strap. The spark gap is 1 mm (0.025 in.) and the overall domain size is 3 mm in the x-direction (-1.5 cm < x < 1.5 cm), 3 cm in the y-direction (-1.5 cm < y < 1.5 cm), and 2 cm in the z direction (-1.4 cm < z < 0.6 cm). An adaptive grid was used with a minimum cell volume of $3.788*10^{-5}$ mm^3 (a minimum cell size of about 30 μm) and a maximum cell volume of 1.361 mm^3 (a maximum cell size of about 1 mm). The total number of cells was 217,868.

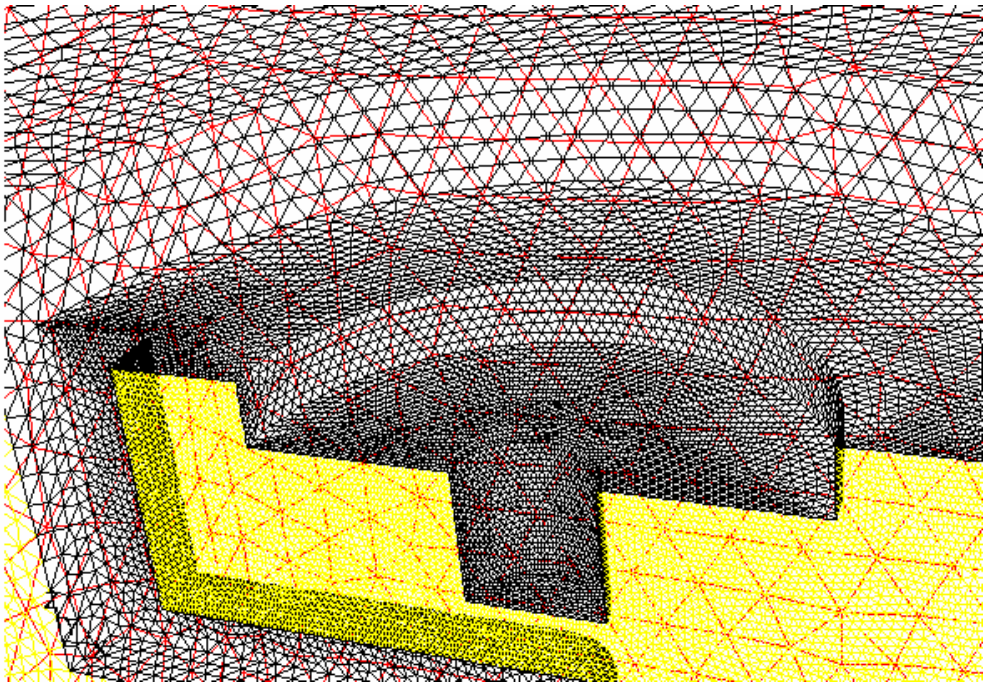

Figure 66b. Close-up view of the computation domain in the region around the spark gap.

The initial simulations were for no bulk flow through the spark gap. The results are shown in Figures 67a-67e. Figure 67a illustrates the temperature contours 1175 μs after breakdown.

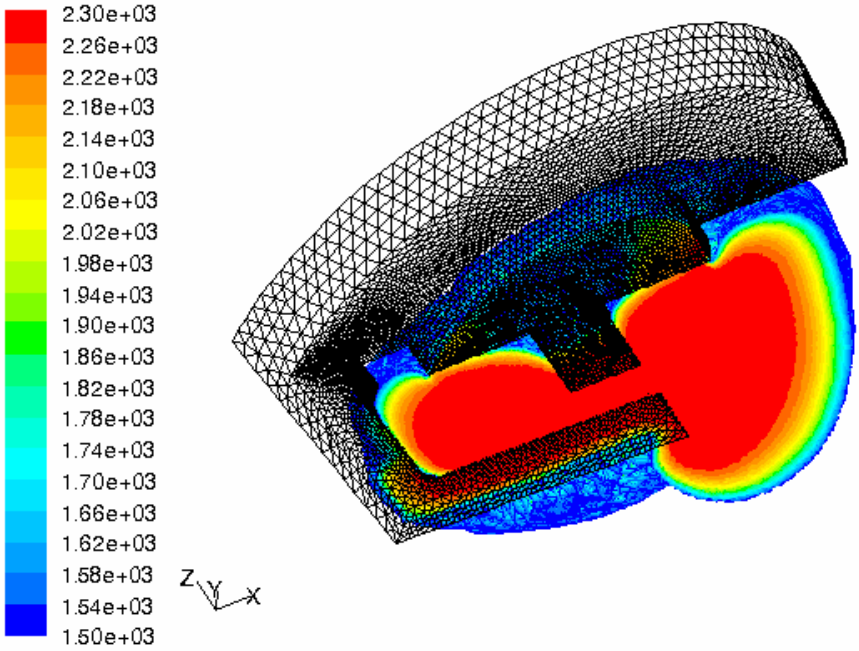

Figure 67a. Temperature contours at 1175 μs without a bulk flow through the spark gap.

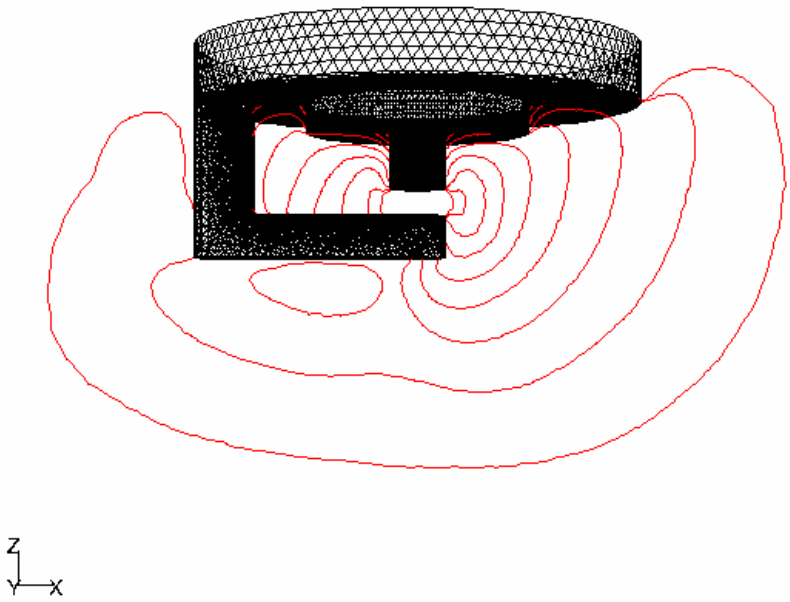

Figure 67b. View of the spark gap, perpendicular to the ground strap, of isotherms (975K < T < 1025K) for a series of times (100, 175, 375, 575, 775, 975, 1175, 1375, and 1575 μs) without a bulk flow through the spark gap.

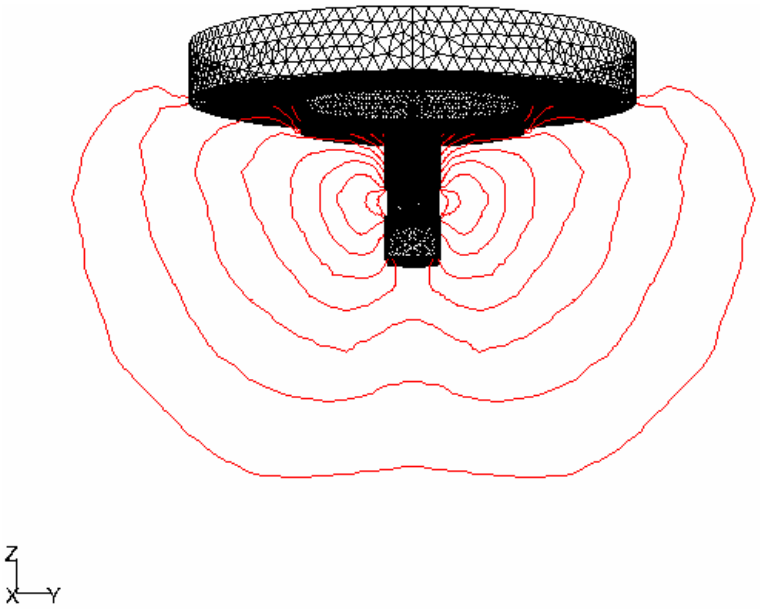

Figure 67c. View of the spark gap, aligned with the ground strap, of isotherms (975K < T < 1025K) for a series of times (100, 175, 375, 575, 775, 975, 1175, 1375, and 1575 μs) without a bulk flow through the spark gap.

Figures 67b and 67c show movement of the 1000 K isotherm as a function of time (for times ranging from 100 to 1575 μs). The 1000 K isotherms are of interest because this is the temperature threshold at which flame chemistry becomes dominant. As illustrated in Figure 67b, the isotherms are almost symmetric relative to the spark channel, except for flow disturbances around the spark plug's ground strap.

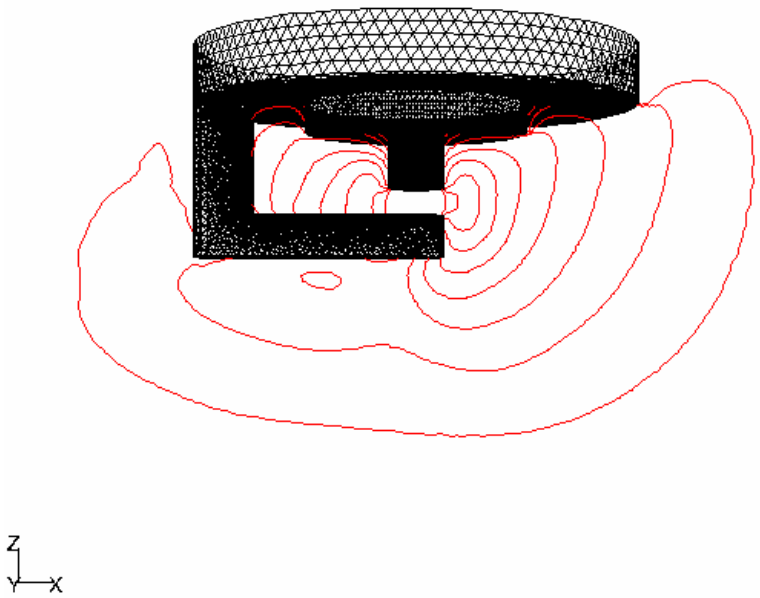

Figure 67d. View of the spark gap, perpendicular to the ground strap, of isotherms (1475K < T < 1525K) for a series of times (100, 175, 375, 575, 775, 975, 1175, 1375, and 1575 μs) without a bulk flow through the spark gap.

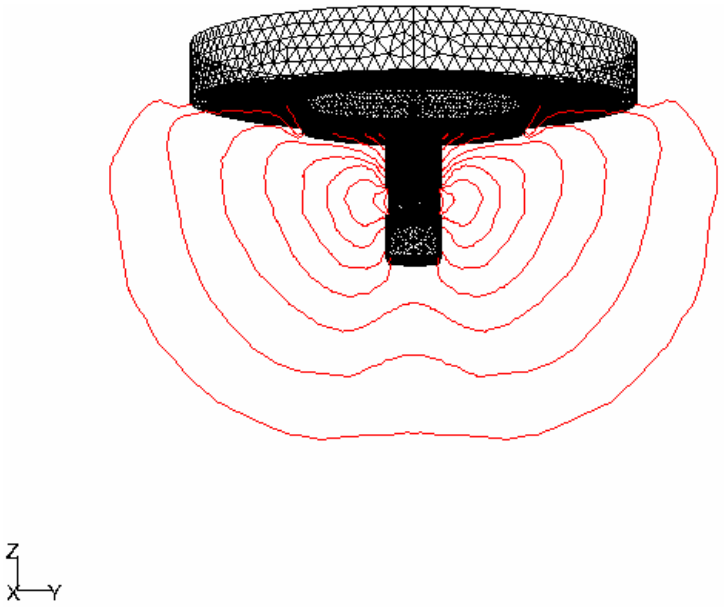

Figure 67e. View of the spark gap, aligned with the ground strap, of isotherms (1475K < T < 1525K) for a series of times (100, 175, 375, 575, 775, 975, 1175, 1375, and 1575 μs) without a bulk flow through the spark gap.

Figures 67d and 67e show the 1500 K isotherms for a sequence of times after breakdown. These results are qualitatively similar to those for the 1000 K isotherms except that the 1500 K isotherms at any specific time are closer to the original spark channel, as expected.

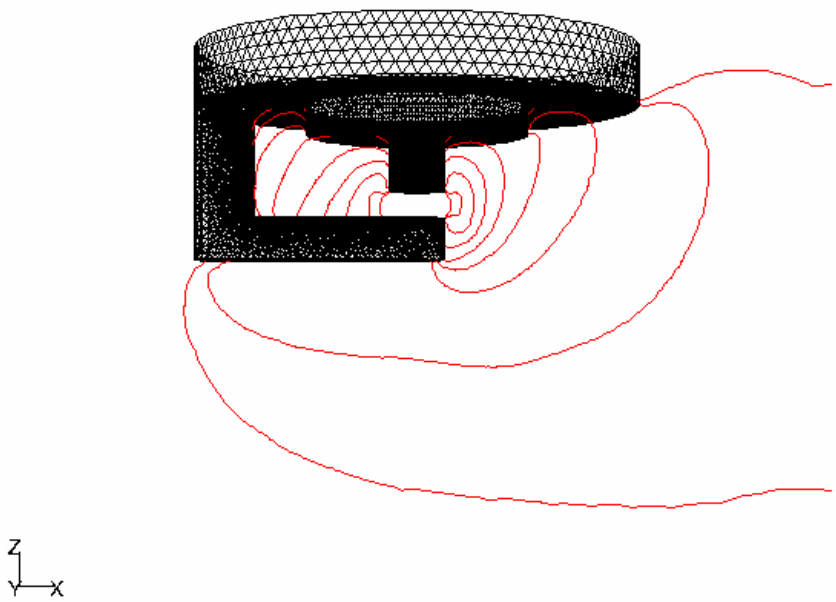

Figure 68a. View of the spark gap, perpendicular to the ground strap, of isotherms (975K < T < 1025K) for a series of times (100, 175, 375, 575, 775, 975, 1175, 1375, and 1575 μs) with a 2 m/s bulk flow through the spark gap.

Our next set of simulations was for a bulk flow of 2 m/s through the spark gap. This imposed bulk flow was in the positive x-direction along the leg of the ground strap, such that the "vertical" portion of the ground strap (in Figure 68a) partially shields the spark gap (that is, the flow is from left to right in Figure 68a).

The effects of the bulk flow are most obvious in Figure 68a, which should be compared to Figure 67b (no bulk flow). In absence of a bulk flow (Figure 67b), the flow structure is caused by the rapid expansion of the burned gases. Thus, whereas the 1000 K isotherms for no bulk flow (Figure 67b) were symmetric around the spark channel, other than for the flow disturbances caused by the ground strap, with an imposed flow (Figure 68a) there is a strong downstream flow and additional flow away from the cylinder head.

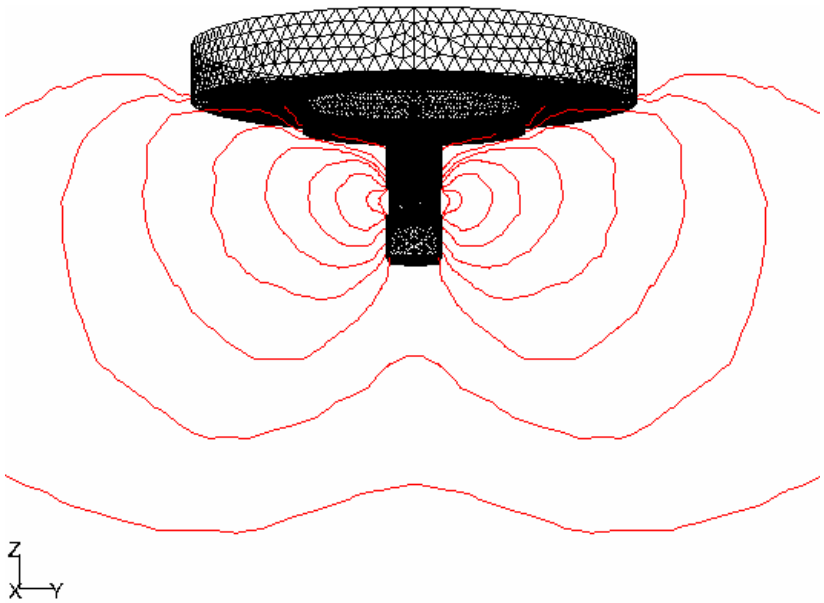

Figure 68b. View of the spark gap, aligned with the ground strap, of isotherms (975K < T < 1025K) for a series of times (100, 175, 375, 575, 775, 975, 1175, 1375, and 1575 μs) with a 2 m/s bulk flow through the spark gap.

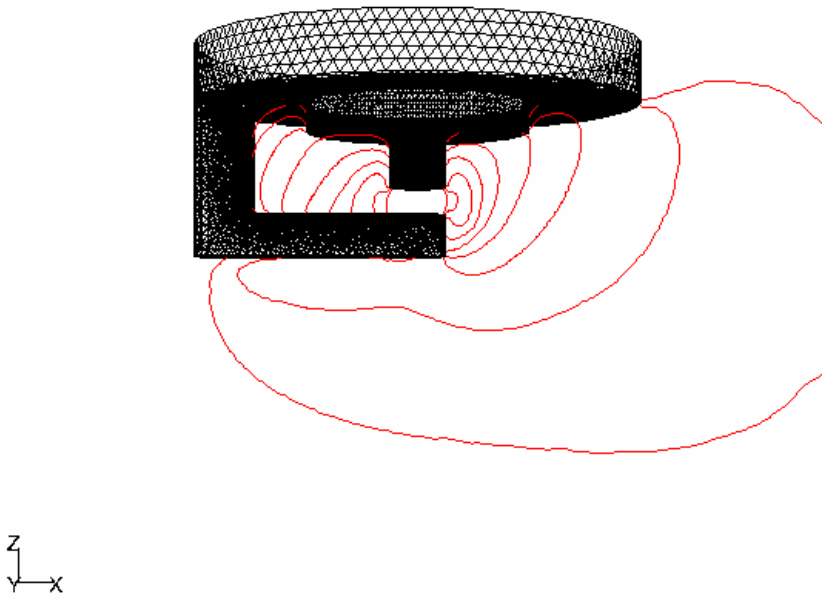

Figure 68c. View of the spark gap, perpendicular to the ground strap, of isotherms (1475K < T < 1525K) for a series of times (100, 175, 375, 575, 775, 975, 1175, 1375, and 1575 μs) with a 2 m/s bulk flow through the spark gap.

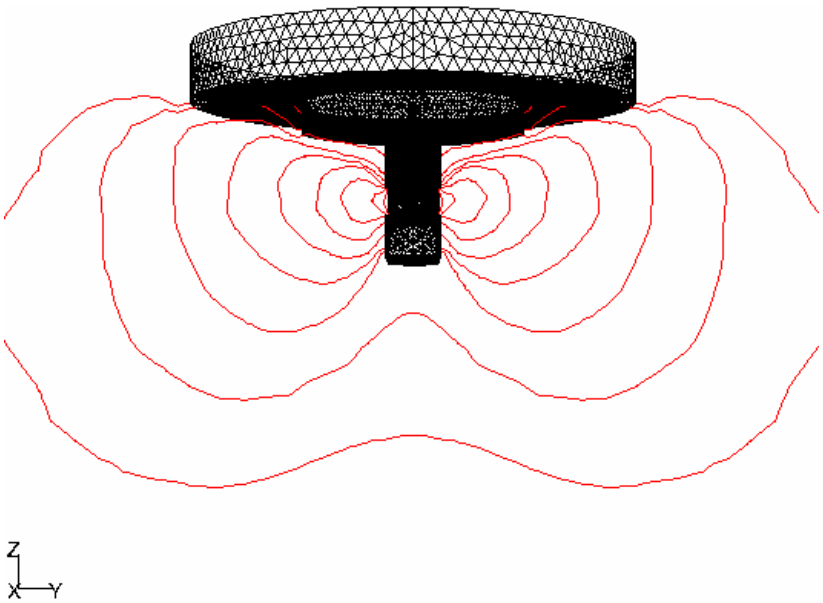

Figure 68d. View of the spark gap, aligned with the ground strap, of isotherms (1475K < T < 1525K) for a series of times (100, 175, 375, 575, 775, 975, 1175, 1375, and 1575 μs) with a 2 m/s bulk flow through the spark gap.

This latter effect is also shown in Figures 68b, which can be compared to Figure 67c. The combination of the bulk flow and the flow induced by expansion also results in a downstream flow away from the cylinder head. These same trends are also observed for the 1500 K isotherms in Figures 68c and 68d (2 m/s) and Figures 67d and 67e (0 m/s).

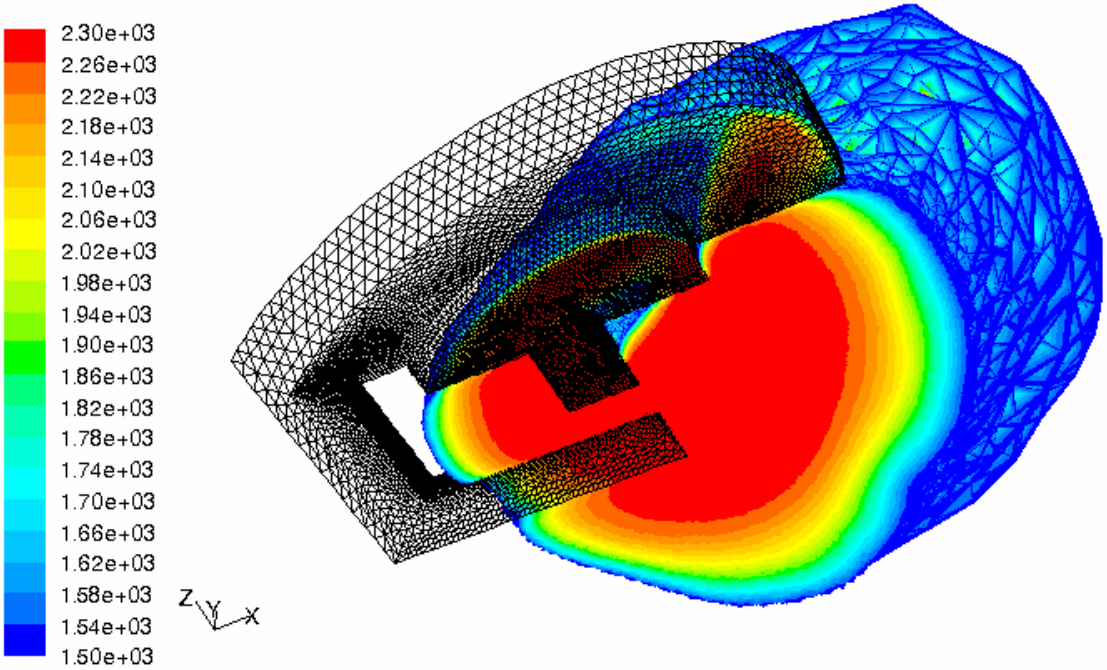

Figure 69a. Temperature contours at 1175 μs with a 10 m/s bulk flow through the spark gap.

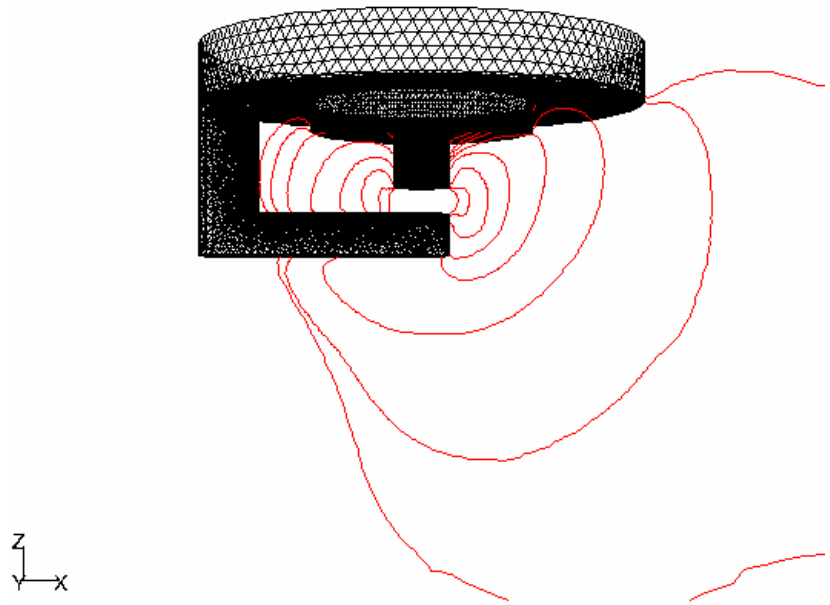

Figure 69b. View of the spark gap, perpendicular to the ground strap, of isotherms (975K < T < 1025K) for a series of times (100, 175, 375, 575, 775, 975, 1175, 1375, and 1575 μs) with a 10 m/s bulk flow through the spark gap.

Our final set of simulations for a conventional spark plug was for a bulk flow of 10 m/s through the spark gap. Again, this imposed bulk flow was in the positive x-direction along the leg of the ground strap, such that the "vertical" portion of the ground strap (in Figure 69a) partially shields the spark gap (that is, the flow is from left to right in Figure 69b).

The temperature contours 1175 μs after breakdown are illustrated in Figure 69a. The effects of the bulk flow are most obvious in Figure 69b, which should be compared to Figures 68a (2 m/s) and 67b (0 m/s). In absence of a bulk flow (Figure 67b), the flow structure is caused by the rapid expansion of the burned gases. Thus, whereas the 1000 K isotherms for no bulk flow (Figure 67b) were symmetric around the spark channel, other than for the flow disturbances caused by the ground strap, with a strong imposed flow (Figure 69b) there is a strong downstream flow and additional flow away from the cylinder head. The flow away from the cylinder head is also shown in Figures 69b and 69c (which can be compared to Figure 67c for no bulk flow, and Figure 68b for a 2 m/s bulk flow). The combination of the bulk flow and the flow induced by expansion also results in a strong downstream flow away from the cylinder head.

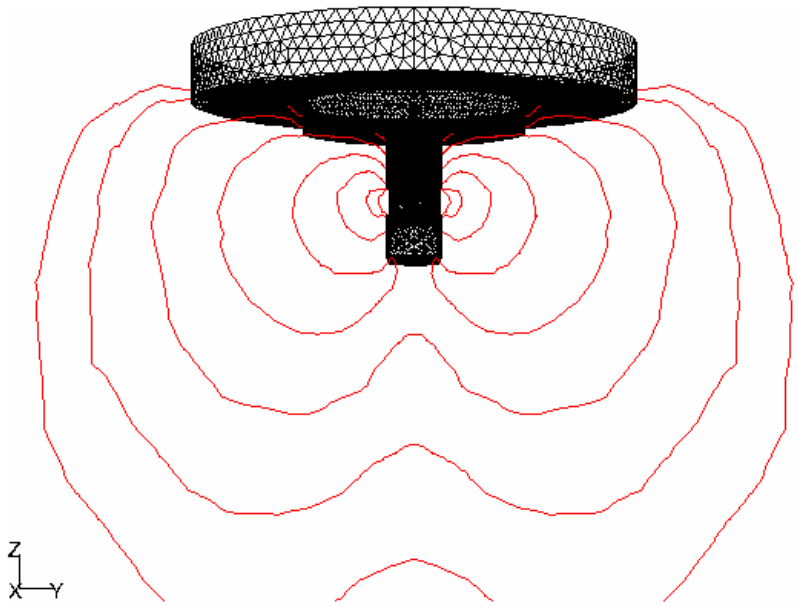

Figure 69c. View of the spark gap, aligned with the ground strap, of isotherms (975K < T < 1025K) for a series of times (100, 175, 375, 575, 775, 975, 1175, 1375, and 1575 μs) with a 10 m/s bulk flow through the spark gap.

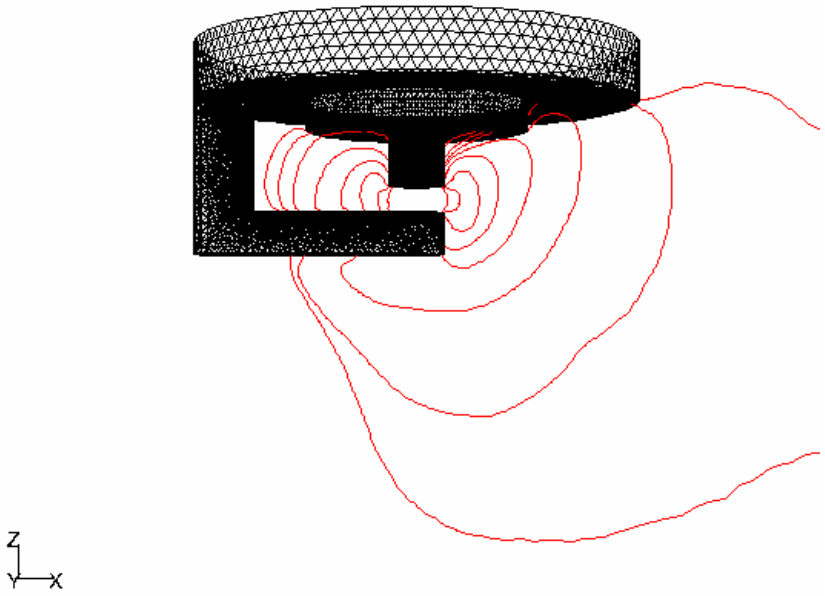

Figure 69d. View of the spark gap, perpendicular to the ground strap, of isotherms (1475K < T < 1525K) for a series of times (100, 175, 375, 575, 775, 975, 1175, 1375, and 1575 μs) with a 10 m/s bulk flow through the spark gap.

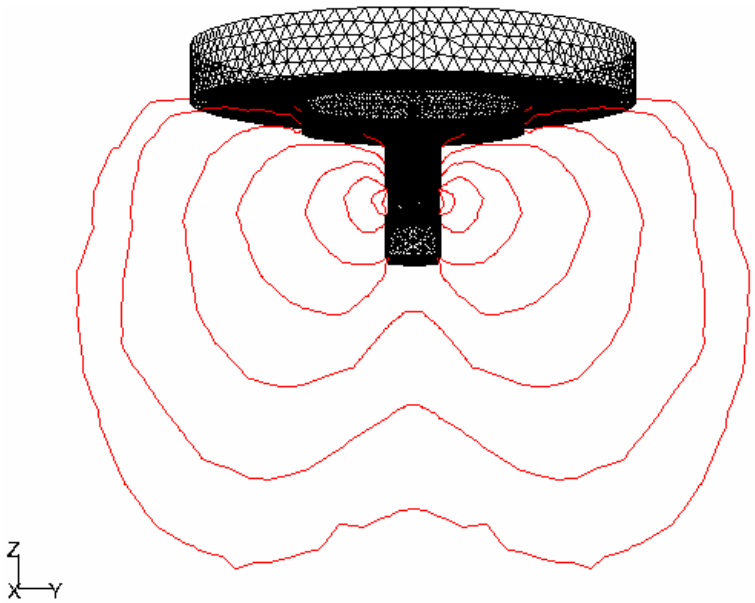

Figure 69e. View of the spark gap, aligned with the ground strap, of isotherms (1475K < T < 1525K) for a series of times (100, 175, 375, 575, 775, 975, 1175, 1375, and 1575 μs) with a 10 m/s bulk flow through the spark gap.

These same trends are also observed for the 1500 K isotherms in Figures 69d and 69e, which can be compared to Figures 68c and 68d (2 m/s) and Figures 67d and 67e (0 m/s).

3.4. Models for Railplug Spark Evolution

In this subsection, we present a simple theoretical model in order to gain better understanding of railplug physics. The railplug is a miniaturized rail gun that has been developed as a new type ignitor for large-bore natural gas engines, and it potentially provides better ignition characteristics and longer life than existing ignition systems used in large natural gas engines. It uses electromagnetic forces and thermal expansion to drive the plasma into the combustion chamber. The main consideration in this portion of the study was to understand the effects of thermal expansion on plasma motion.

Related literature can be classified in two categories: 1) the early railplug studies conducted at The University of Texas and 2) other research that has investigated arc motion between the electrodes of rail guns.

Most prior railplug studies were based on experimental analyses. Hall and coworkers (1991) presented the results from a series of experiments that included demonstration of the effects of electromagnetic forces on plasma movement, a comparison between railplug versus spark ignition, and effects of stored energy levels on railplug performance. A later study by Ellzey et al. (1993) presented the results of a numerical model compared with experimental results. It is worth noting that this computational model did not solve the complete set of magneto-hydrodynamic (MHD) equations. Matthews and coworkers (1992) investigated electronics "matching" and the influences of the railplug geometry, rail materials, and delivered energy on electrode durability.

Plasma arc modeling is the most relevant part of the rail gun research that was conducted extensively in the 1980s and early 1990s. Powell and Batteh (1981) proposed a one-dimensional, steady model in an accelerating frame of reference. This model served as a

baseline model to the two-dimensional, unsteady models of Huerta and Boynton (1991). Another model of arc motion focused on low voltage circuit breaker simulations. Karetta and Lindmayer (1998) presented a three-dimensional model that simulated arc motion between rail electrodes in a simple arc chamber. Before closing this section, it should be noted that although similar physics occur for different arc systems, the total average currents can be very different. For example, the total average currents are on the order of 10^5 A in rail gun systems, and are on the order of 10^3 A in circuit breaker systems, whereas railplugs operate with an average current of about 100 A. In addition, the duration of the arc, which is on the order of milliseconds, in reference studies is much longer than that required by the railplug ignitor, which is on the order of microseconds.

3.4.A. *Model and Governing Equations*

In its most simple form, a railplug consists of two parallel rails (electrodes), which carry current provided by an external circuit. In Figure 70, a schematic of a railplug with parallel rails, the current is carried from the lower to the upper rail through a plasma arc. The space between the electrodes is occupied by gas and a cloud of charged particles, which is called a plasma.

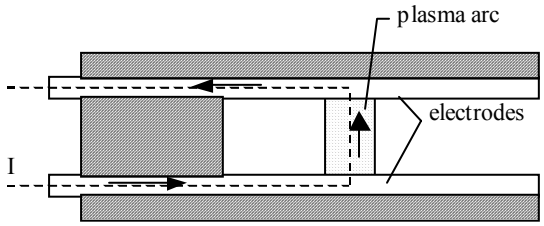

Figure 70. Schematic of a railplug with parallel electrodes.

In our problem, the time required to reach local thermal equilibrium within the plasma is much shorter than the time required to get significant changes in plasma conditions. In other words, the collision time constitutes the smallest time scale, which means that the plasma is collision-dominated and can be described with continuum models. In this study, a single fluid description of the plasma is used with the typical limitations of magnetohydrodynamics (Kulsrud, 1989).

In this one-dimensional model, all quantities change in the x-direction only. The magnetic field has only a z-component that can be shown using the Biot-Savart law to change in the x-direction. The current density can be calculated with the known distribution of magnetic field as described below.

The relevant Maxwell equations in MHD are:

$$\nabla \cdot \vec{B} = 0 \quad \text{(Gauss's Law)} \tag{31}$$

$$\nabla \times \vec{E} = -\frac{\partial \vec{B}}{\partial t} \quad \text{(Faraday's Law)} \tag{32}$$

and

$$\nabla \times \vec{B} = \mu_0 \vec{j} \quad \text{(Ampere's Law)} \tag{33}$$

The generalized Ohm's Law can be written as

$$\vec{j} = \sigma_e \left(\vec{E} + \vec{\mathrm{u}}_\mathrm{e} \times \vec{B} \right) \tag{34}$$

For the one-dimensional geometry, the current density has a y-component only, and using Gauss's law and Ampere's law it can be calculated as

$$j_y = -\frac{1}{\mu_0} \frac{\partial B_z}{\partial \mathrm{x}} \tag{35}$$

Equations 31-34 can be reduced to a single equation by solving Equation 34 for $\vec{E}$, and substituting the result in Equation 32, yielding

$$\frac{\partial B_z}{\partial \mathrm{t}} + \frac{\partial}{\partial \mathrm{x}} \left(\mathrm{u} B_z \right) = -\frac{\partial}{\partial \mathrm{x}} \left(\frac{j_y}{\sigma_\mathrm{e}} \right) \tag{36}$$

The current density in Equation 36 can be eliminated using Equation 35 to get the magnetic induction equation that advances the magnetic field B_z in time:

$$\frac{\partial B_z}{\partial \mathrm{t}} + \frac{\partial \left(\mathrm{u} B_z \right)}{\partial \mathrm{t}} = \frac{\partial}{\partial \mathrm{x}} \left(\frac{1}{\mu_0 \sigma_\mathrm{e}} \frac{\partial B_z}{\partial \mathrm{x}} \right) \tag{37}$$

After having obtained the equations for magnetic field and arc density, it is now necessary to derive a set of equations that describes the fluid dynamics of the problem. One-dimensional, fully compressible equations that express conservation of mass, momentum, and energy can be written as:

$$\frac{\partial \rho}{\partial \mathrm{t}} + \frac{\partial (\rho \mathrm{u})}{\partial \mathrm{x}} = 0 \tag{38}$$

$$\rho \frac{D\mathrm{u}}{D\mathrm{t}} = -\frac{\mathrm{dP}}{\mathrm{dx}} + \frac{\partial}{\partial \mathrm{x}} \left[\left(2\mu \frac{\partial \mathrm{u}}{\partial \mathrm{x}} + \mu' \frac{\partial \mathrm{u}}{\partial \mathrm{x}} \right) \right] + j_y B_z \tag{39}$$

$$\rho \mathrm{C_p} \frac{D\mathrm{T}}{D\mathrm{t}} = \frac{D\mathrm{P}}{D\mathrm{t}} + \frac{\partial}{\partial \mathrm{x}} \left(\mathrm{k} \frac{\partial \mathrm{T}}{\partial \mathrm{x}} \right) + \frac{j_y^2}{\sigma_\mathrm{e}} \tag{40}$$

These are the usual equations in fluid mechanics with the additional terms to the momentum and energy equations that make them suitable for MHD flows. The force term, $j_y B_z$ in the momentum equation, is the electromagnetic force (the Lorentz force), and the source term, $\left(j_y^2 / \sigma \right)$ in the energy equation is the Ohmic heating term. To close the system of equations we need a constitutive relation, namely an equation of state. Therefore, with the assumption of ideal gas behavior of the plasma

$$\mathrm{P} = \rho R \mathrm{T} \tag{41}$$

The aim of this part of the study was to investigate the effects of thermal expansion on arc behavior rather than seek a detailed description of the arc evolution with more complete physics. Therefore, pressure is assumed to be uniform over the computational domain. Physically, this constitutes a slow heating or low Mach number approximation, as discussed by Rehm and Baum (1978).

The final form of the mathematical model used in this study for arc behavior is summarized here for convenience. The equation for the energy to advance the fluid temperature T in time is:

$$\rho \mathrm{C_p} \frac{\partial \mathrm{T}}{\partial \mathrm{t}} + \rho \mathrm{C_p u} \frac{\partial \mathrm{T}}{\partial \mathrm{x}} = \frac{\partial}{\partial \mathrm{x}} \left(\mathrm{k} \frac{\partial \mathrm{T}}{\partial \mathrm{x}} \right) + \frac{j_y^2}{\sigma_\mathrm{e}} \tag{42}$$

The fluid density ρ can be found at each time-step using the Ideal Gas Equation of State (Equation 41) since pressure is known and constant with the assumption of the isobaric flow. The equation of mass conservation is integrated to advance the fluid velocity *u* in time:

$$\rho u = \rho u\big|_0 + \int_0^x \frac{\partial \rho}{\partial t} dx \tag{43}$$

and the magnetic induction equation (Equation 27) is used to advance *B* in time. Finally, the curl of magnetic field B_z is solved to determine the arc density distribution over the computational domain (Equation 35).

3.4.B. *Initial Conditions*

Arc initiation in the railplug ignitor system is achieved with breakdown of gases between the electrodes. The duration of the breakdown is on the order of 10 nanoseconds and that period cannot be simulated with continuum models because the gas during breakdown is not in equilibrium. Therefore, this simulation starts just after the breakdown of air between the electrodes. The initial plasma length is taken as 40 μm with the plasma temperature set to 6000 K. Detailed information on the methods used to find the plasma radius, temperature, and pressure just after breakdown are provided from prior results of the present project (e.g., Seers, 2003). The ambient temperature and the back-wall temperature of the ignitor are taken as 700 K, which is a reasonable assumption for natural gas engines. As mentioned earlier, pressure in the computational domain is taken to be uniform and equal to atmospheric pressure.

3.4.C. *Boundary Conditions*

Temperature and velocity boundary conditions at the upstream wall are used as Dirichlet conditions, i.e., temperature and velocity are given. Neumann conditions are used at the downstream boundary; first derivatives of the temperature and velocity are set to zero. The magnetic field is set to

$$B_z = \mu_o I' \tag{44}$$

at the upstream boundary with the assumption of infinitely wide electrodes, where I' is the current per unit width between the electrodes. At the downstream boundary, the magnetic field is set to zero.

3.4.D. *Numerical Method*

A set of differential equations is discretized implicitly using the finite volume formulation. The implicit solver generated is first order accurate in time and second order accurate in space. The main reason for using an implicit solver is to avoid dealing with the extremely small time-steps that would be required to get stable numerical solution of the magnetic induction equation, which has a very large magnetic diffusion coefficient ($1/\mu_0\sigma_e$). It is also worth noting that lagged coefficients, old time-step level values, are used to linearize the difference equations (e.g., Tannehill et al., 1997). The grid spacing was set at 10 μm and the time-step was set at 5×10^{-10} seconds. The Thomas algorithm is employed to find the unknowns in the discretized energy and magnetic induction equations.

3.4.E. *Results*

The magnetic permeability is constant and taken equal to the vacuum value, $\mu_0 = 4\pi \times 10^{-7}$ Henry/m. Unless otherwise specified, transport and thermodynamic properties of

air are taken as a function of temperature from Boulos et al. (1994). In each figure, time is given in seconds.

In the first set of results (Figures 71-75), a steady current of $5x10^3$A/m was used as an input parameter, and the specific heat of air was taken as a constant, C_p=1100 J/kg-K.

The temperature profile in the computational domain is shown in Figure 71 at different times. A large temperature gradient can be seen near the back wall (x=0), which is a result of the specified constant temperature at the wall. As can be seen in Figure 71, the temperature quickly increases from its initial value to a maximum, which is the same at all times at approximately 8300 K. It should also be noted that the position of the temperature maximum changes in time; this motion will be related to arc motion later.

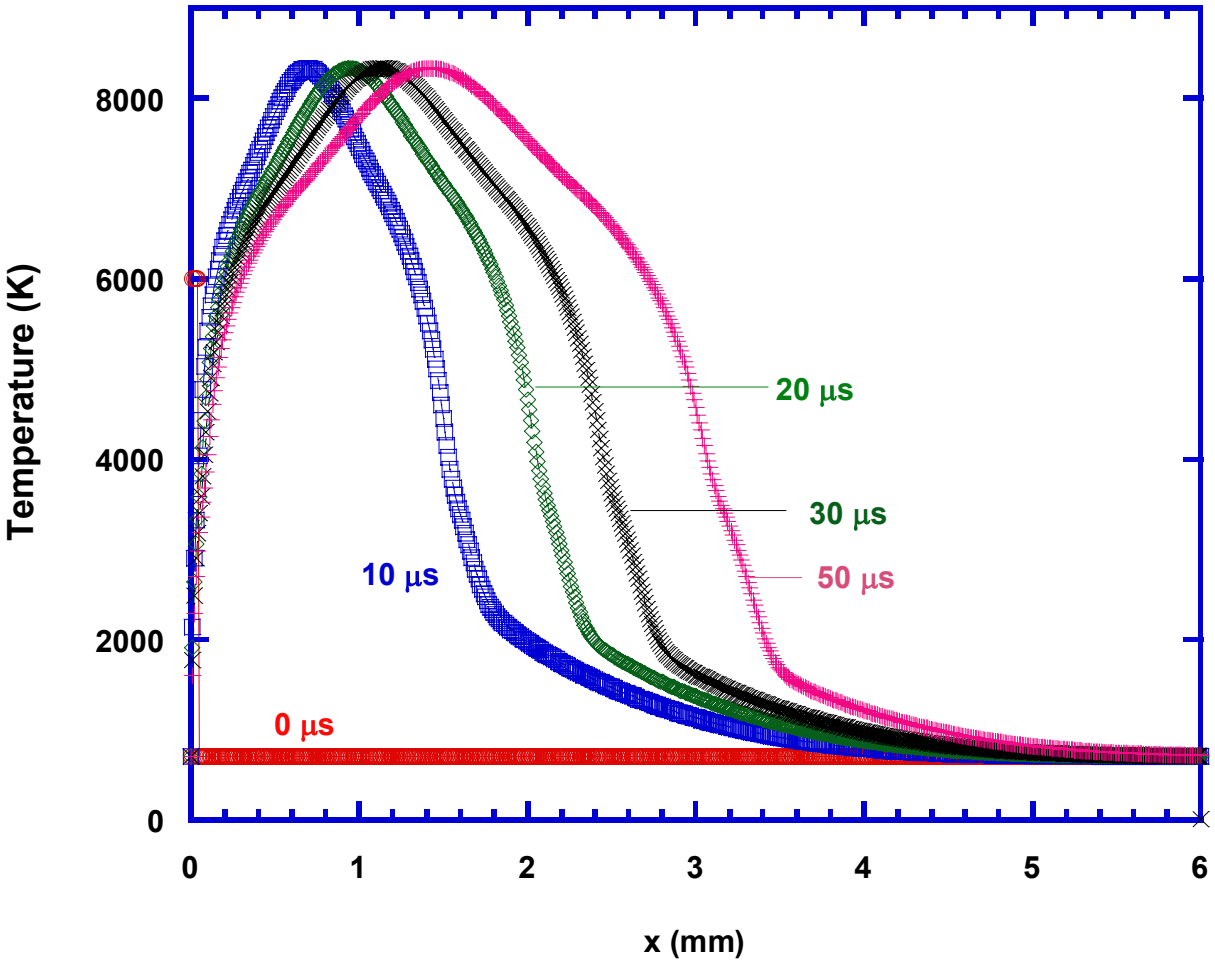

Figure 71. Temperature distribution at different times, assuming constant specific heats.

The density and velocity profiles are provided as Figures 72 and 73, respectively. Spreading of the low-density region between the electrodes is observed due to increased temperature of the fluid. This decrease in density causes expansion of the fluid in the x-direction. The velocities at earlier time-steps are higher because of sudden changes in temperature and, thus, density.

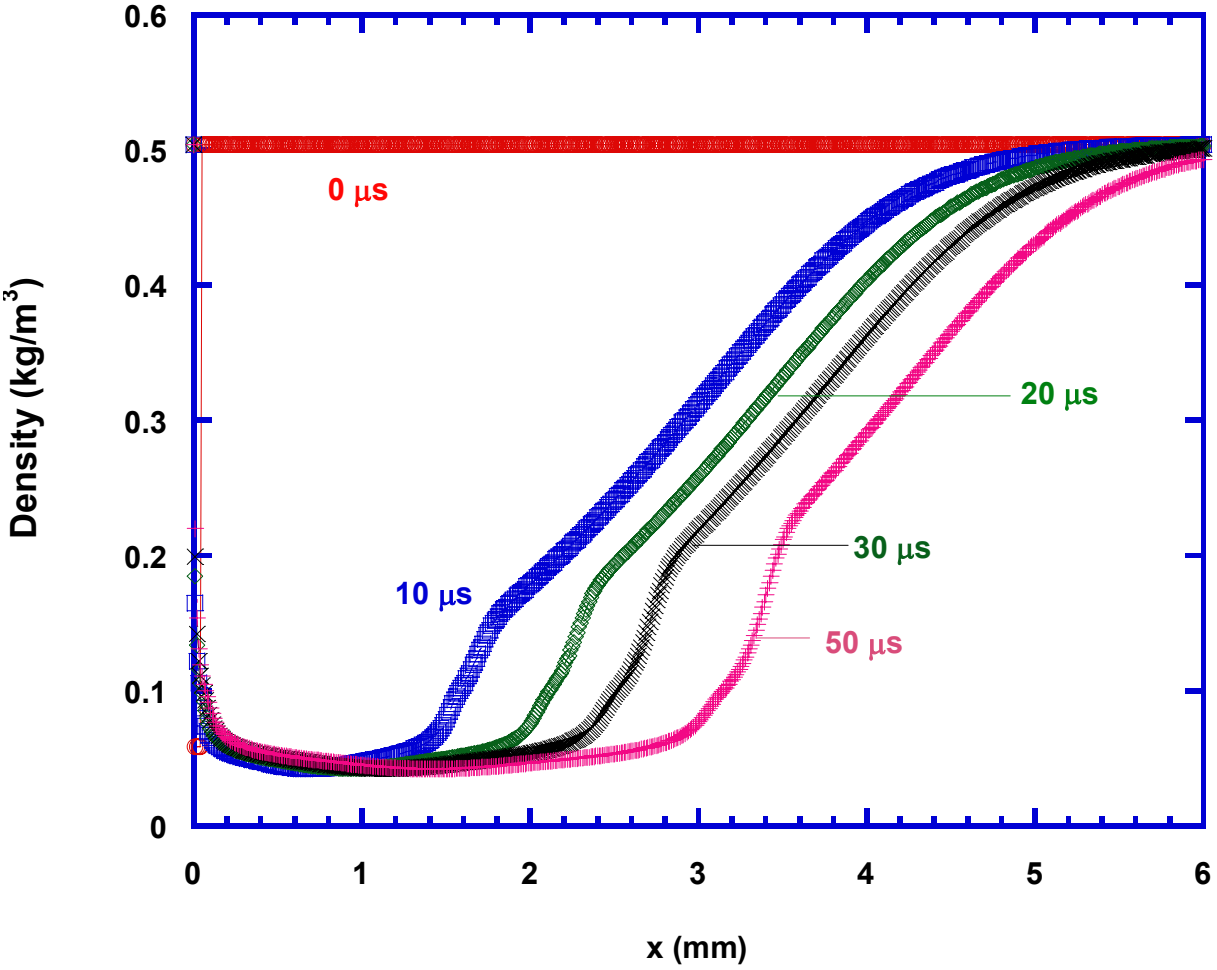

Figure 72. Predicted density distribution at different times; constant specific heats.

Small negative velocities can be seen in Figure 73. These are caused by two different phenomena. First, thermal expansion of the locally heated gases causes fluid to move in both directions. Second, positive movement of the maximum temperature location leaves a cooling region behind. As temperature decreases, density increases and requires net motion of fluid to that region with negative velocities. When velocities reach their steady values, an inflection in the slope is observed in the temperature curves in Figure 71.

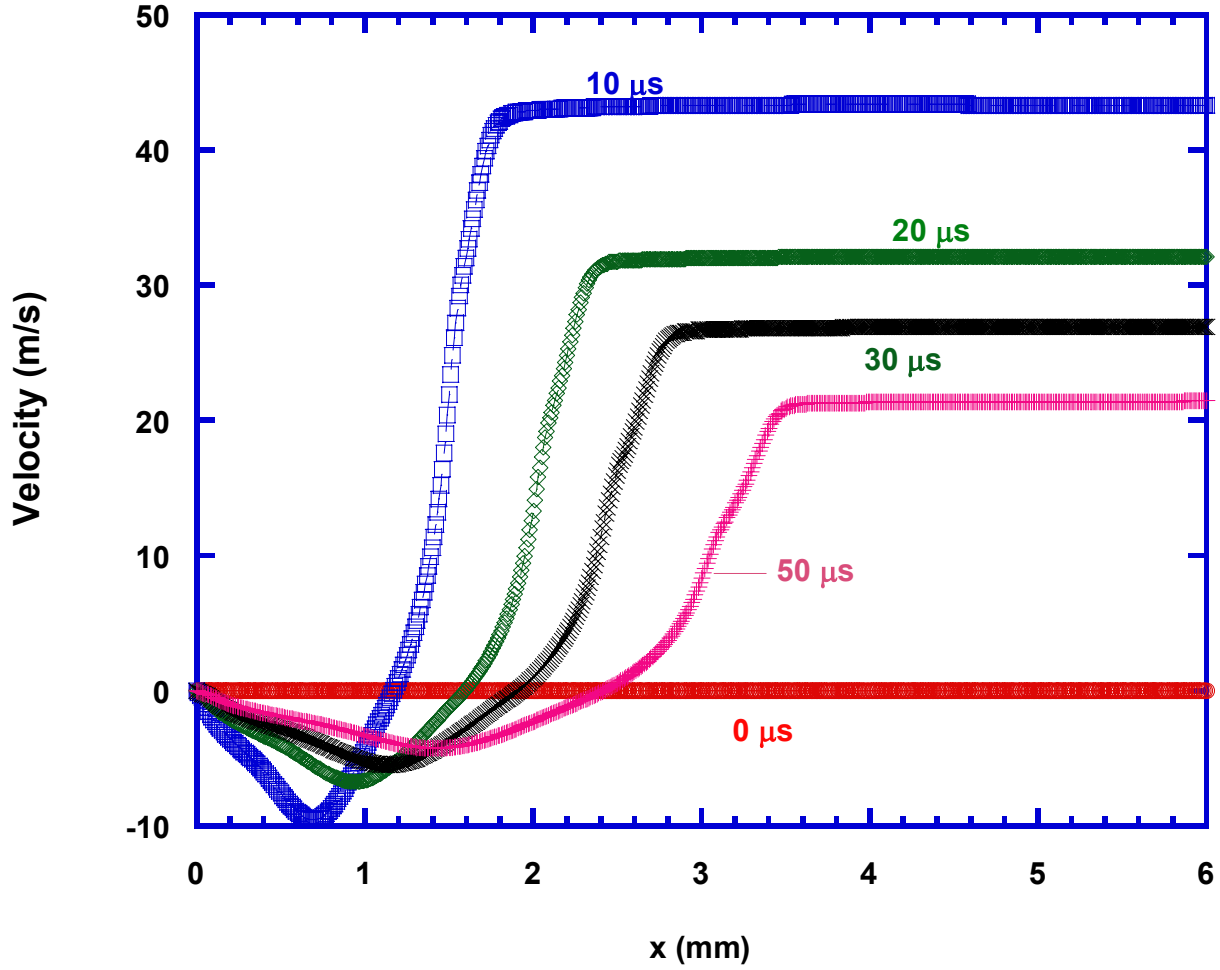

Figure 73. Predicted velocity distribution at different times; constant specific heats.

The magnetic field distribution is shown in Figure 74. This distribution is very important since it specifies the current density distribution. The magnetic induction equation has convective and diffusive parts. The relative contribution of each term to changes in *B* can be determined by checking the magnetic Reynolds number (e.g., Zahn, 1979), where the magnetic Reynolds number is defined as:

$$\mathrm{Re}_m = \sigma_e \mu_o u L \qquad (45)$$

and represents the ratio of convection to diffusion of the magnetic field *B*. With the known values of electrical conductivity σ_e is on the order of 10^3 A/V-m, magnetic permeability μ_0 is on the order of 10^{-6} Henry/m, velocity u is on the order of 10 m/s, and the rail length *L* is on the order of 10^{-3} m, the magnetic Reynolds number is approximately 10^{-5} and the effect of convection of B is negligible in comparison to diffusion. Therefore it should be stated that the *B* profiles presented here are primarily caused by the diffusion of magnetic field. Typical behavior of the curves in Figure 74 can be characterized with three different regions, as discussed below.

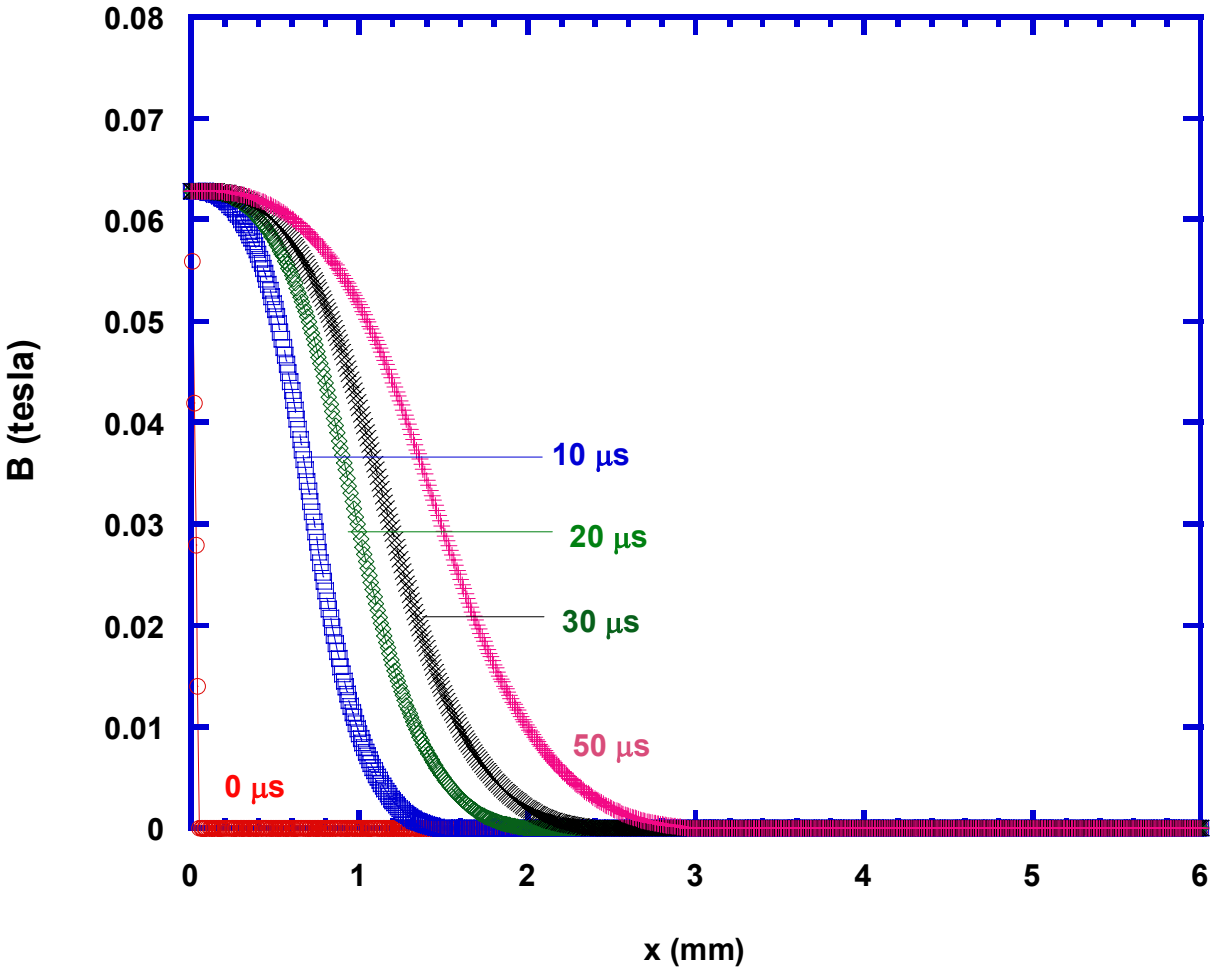

Figure 74. Magnetic field distribution at different times; constant specific heats.

The tail (large values of x), in which magnetic field B is practically zero, identifies the first region. Physically, it is the low temperature, electrically non-conducting region. Electrical conductivity, which is a very strong function of temperature, goes to zero very rapidly at low temperatures. As a result of very low electrical conductivity, the magnetic diffusivity ($1/\mu_0\sigma_e$) goes to very large values, and this means that magnetic diffusion smoothes everything out.

The second region can be identified with the rapid change in magnetic field B. It is the region where most of the current flows, and it has high temperatures. The last region, where the gradient dies out and magnetic field B goes to the boundary value at x=0, has a special importance because it represents the distance that the arc has traveled.

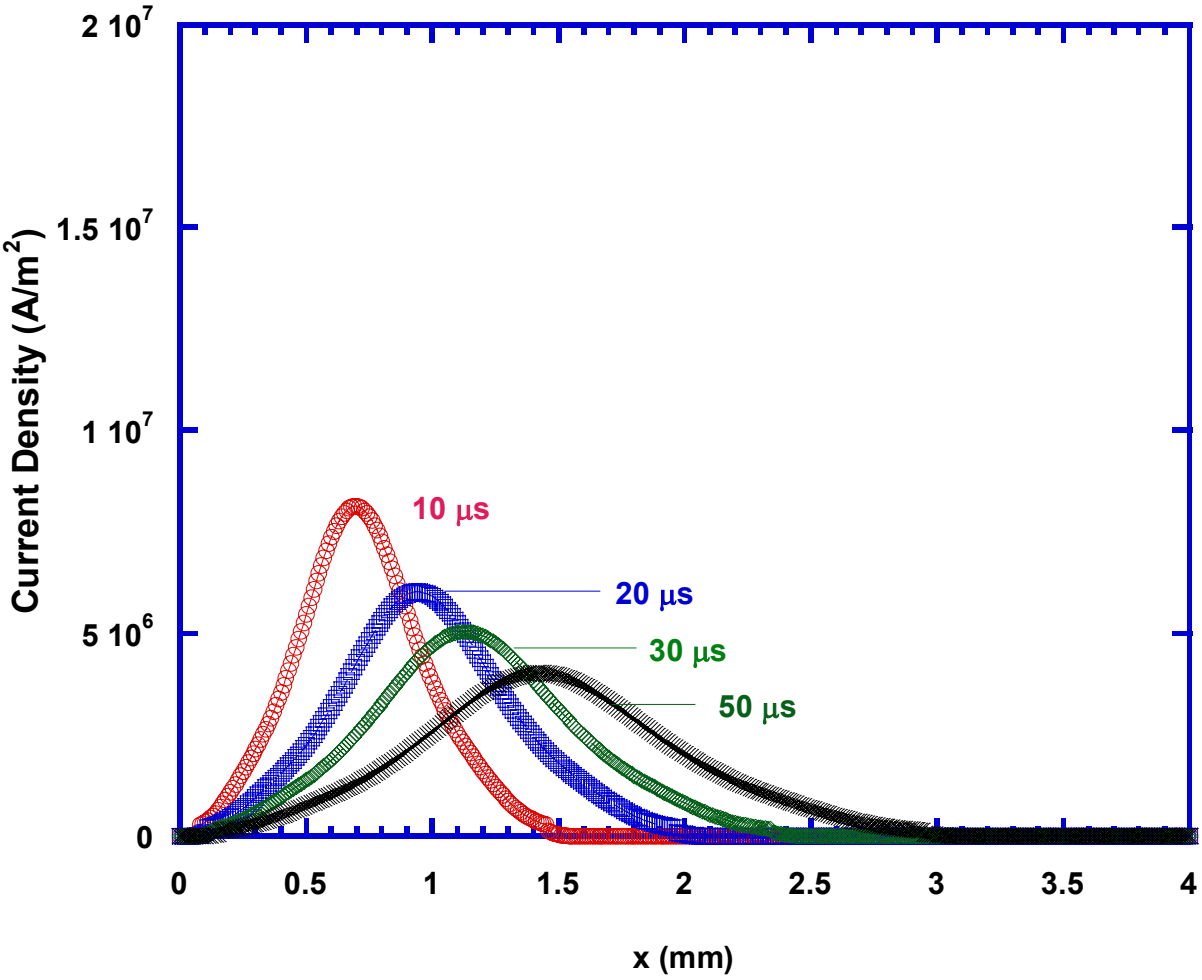

Figure 75. Current density distribution at different times; constant specific heats.

Current density distributions at different times are given in Figure 75. The peaks of the distributions are the maximum currents and it can be seen that the arc is moving in the x-direction with time. The spreading of the distribution as time increases means the arc radius is also increasing. The arc maximum has traveled around 1.5 mm in 50 μs, yielding an average speed of 30 m/s. These speeds are significantly slower than what is encountered for actual arcs, but are valid when one uses the slow electrical energy addition of this work. It is also important to note that the locations where current density goes to zero yield inflection points in the temperature and velocity distribution curves, Figures 71 and 73 respectively.

In the second set of results (Figures 76-82), the variable specific heats of air were used instead of constant C_p, with the same current used as an input parameter ($5x10^3$ A/m). Please note the scale change in the x-axis in Figures 76-82. Figure 76 shows the temperature distribution within the computational domain for the first 50 μsec. Examining the two sets of temperature results, Figures 71 and 76, it is seen that the curves are almost identical in shape with the same maximum temperature values. The only difference between the constant and variable specific heat cases is the width of the high temperature zone. Variable specific heat results show that increasing specific heat causes more inertia (lower thermal diffusivity) in the high temperature regions, which prevents diffusion of temperature through the computational

domain. The temperature maximum has traveled around 0.7 mm for the variable specific heat case as compared to around 1.5 mm with constant specific heat.

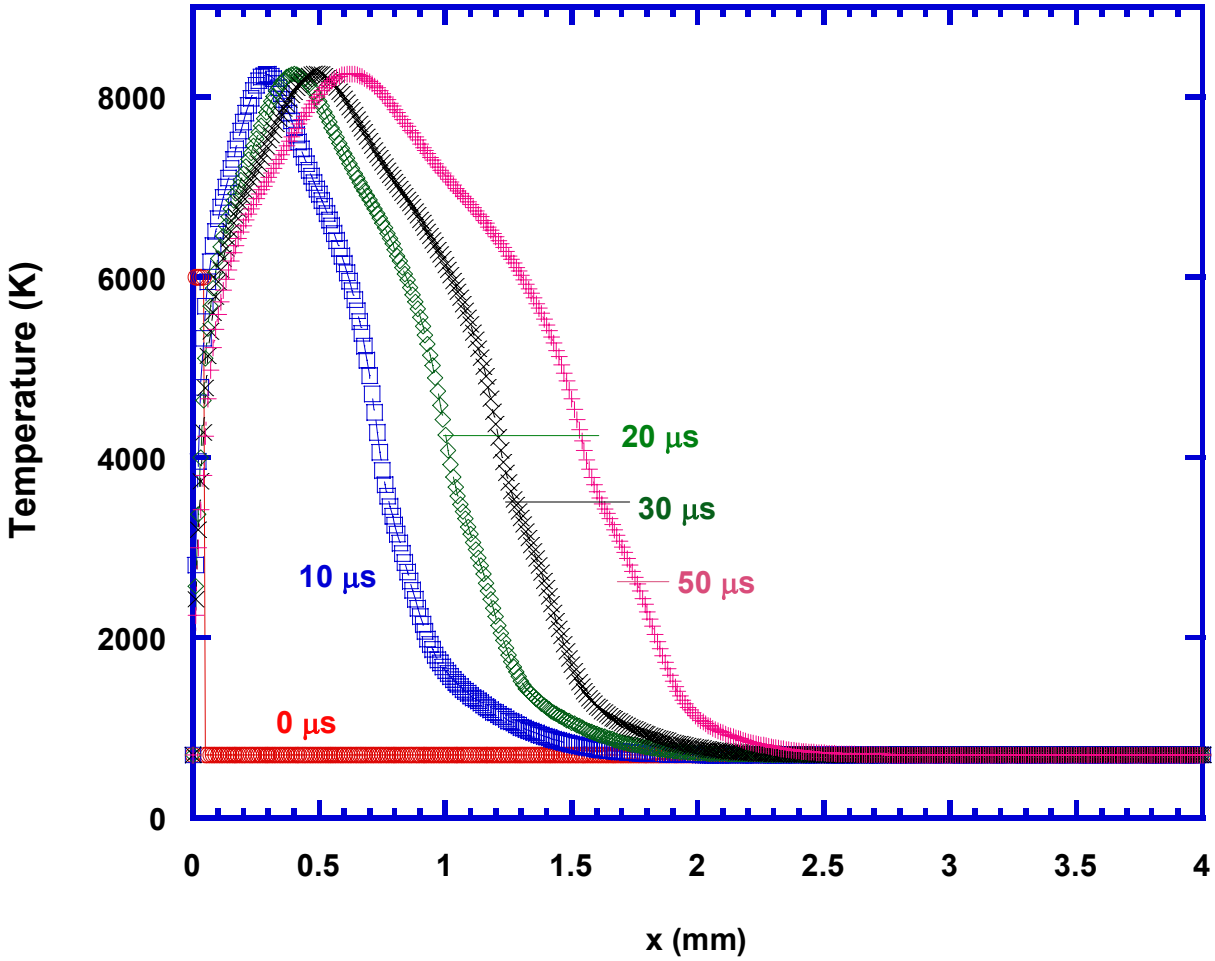

Figure 76. Temperature distribution at different times, variable C_p.

Since the current density distribution is mainly affected by the temperature distribution, using a variable specific heat is expected to show similar effects on the current profile between the electrodes. As can be seen from Figure 77, the arc has moved less than half of the distance it moved in the previous, constant C_p case. Arc widths are also narrower in the variable specific heat case with a result that the current density peaks are higher to preserve the total current.

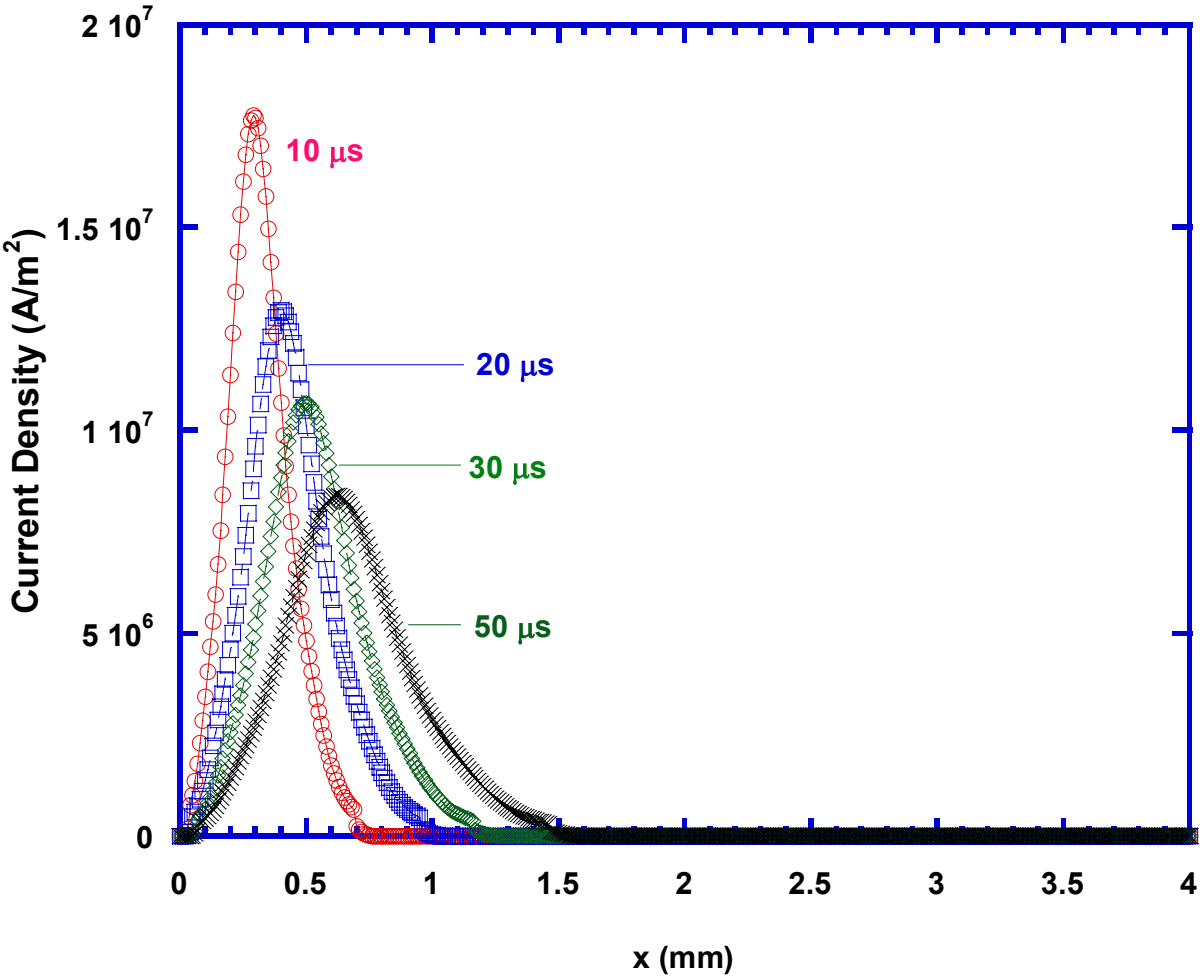

Figure 77. Current density distribution at different times, variable C_p.

More insight on the physics can be gained by analyzing simpler problems. One possibility is to run the model with no convective terms to assess the relative importance of convection to diffusion. The temperature distribution curves in Figure 78 show that, with no velocity, the high temperature regions become more compact. The temperature profile is almost symmetrical with respect to its maximum because there is no flow in the domain to alter the symmetry of the temperature profile.

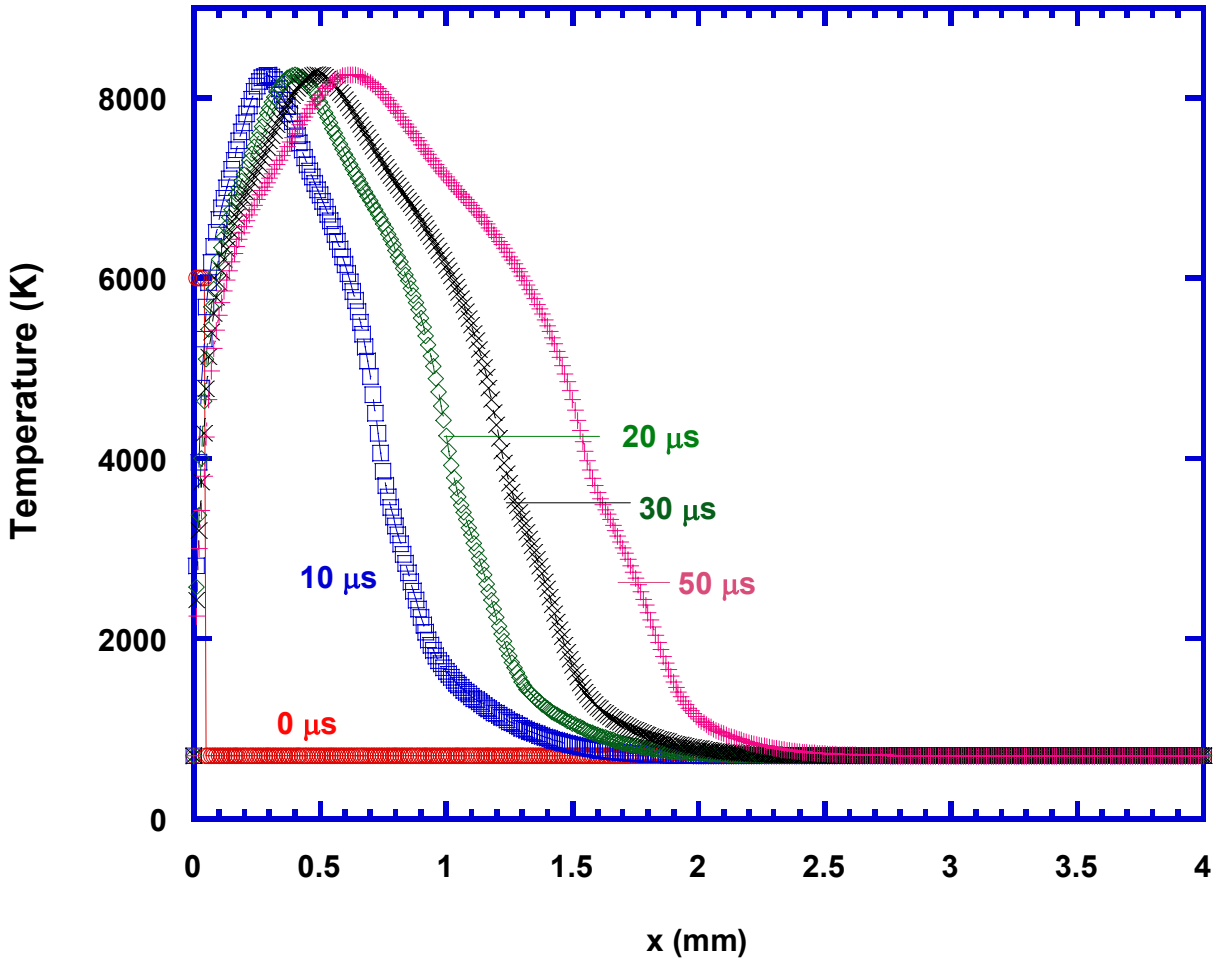

Figure 78. Temperature distribution at different times, variable C_p, no velocity.

Figure 79 shows the current density distribution at different times. Current profiles become narrower as an expected result of the narrowing of the temperature distribution.

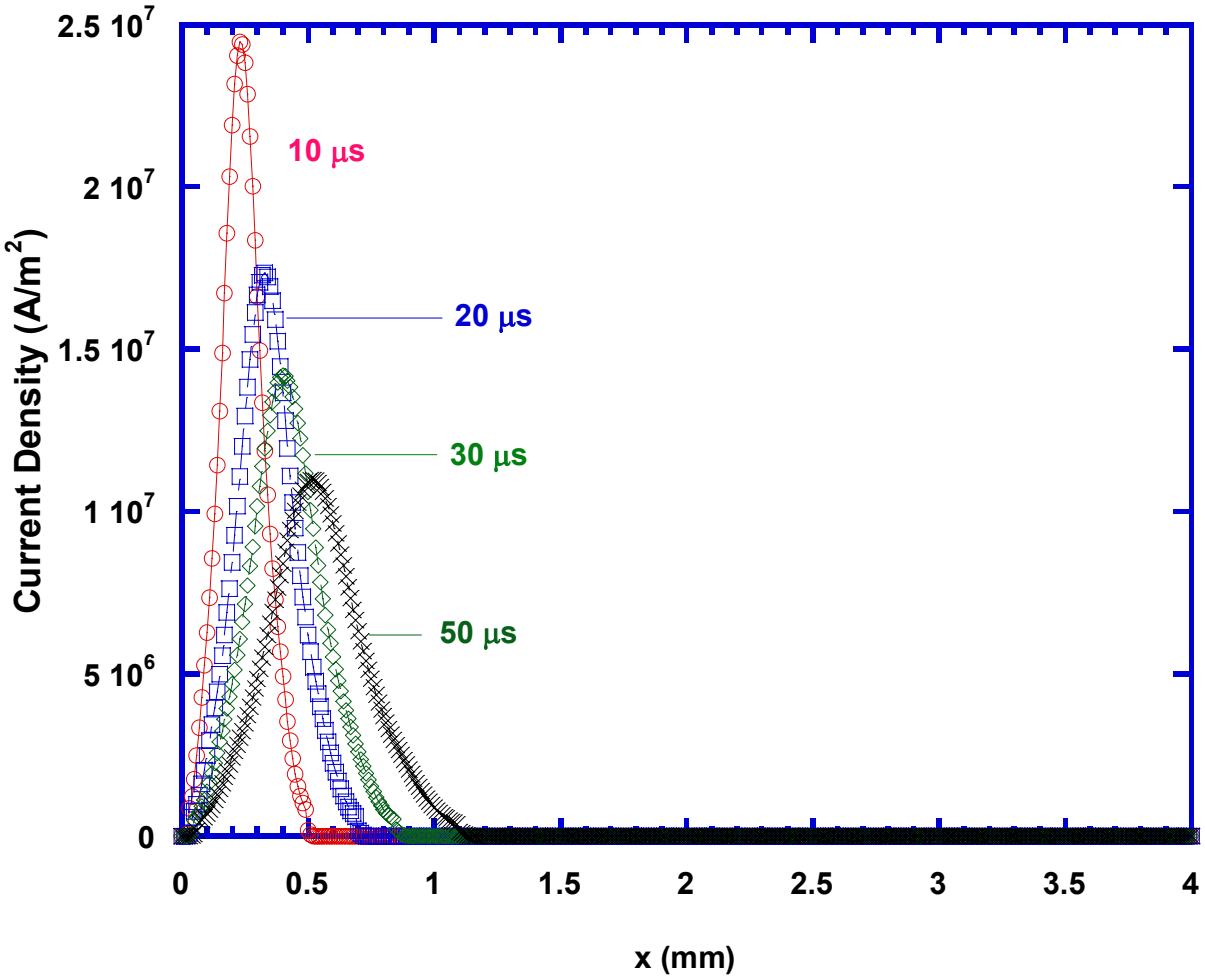

Figure 79. Current density distribution at different times, variable C_p, no velocity.

We ran one more test taking the boundary wall at x=0 as adiabatic, i.e., no heat transfer through the wall. It served as the last numerical experiment conducted in this study. The temperature distribution results in Figure 80 show that the maximum temperature in the computational domain increases to around 10,500 K with an adiabatic wall at the back. No motion of the maximum temperature is observed, as expected; it always stays at its initial position. The adiabatic wall behaves as an axis of symmetry for the computational domain, and temperature is just spreading through the domain keeping its maximum at the center, which is at the adiabatic wall (x=0) in this case.

The magnetic field and current density distributions are shown in Figures 81 and 82, respectively. Note that the range for the x-axis is half that for Figure 81 compared to that used for Figure 80. One of the three different regions described previously using Figure 74 has disappeared. The new magnetic field distribution can be defined with two regions. The first one is the conducting high temperature region that starts with the adiabatic wall at the back.

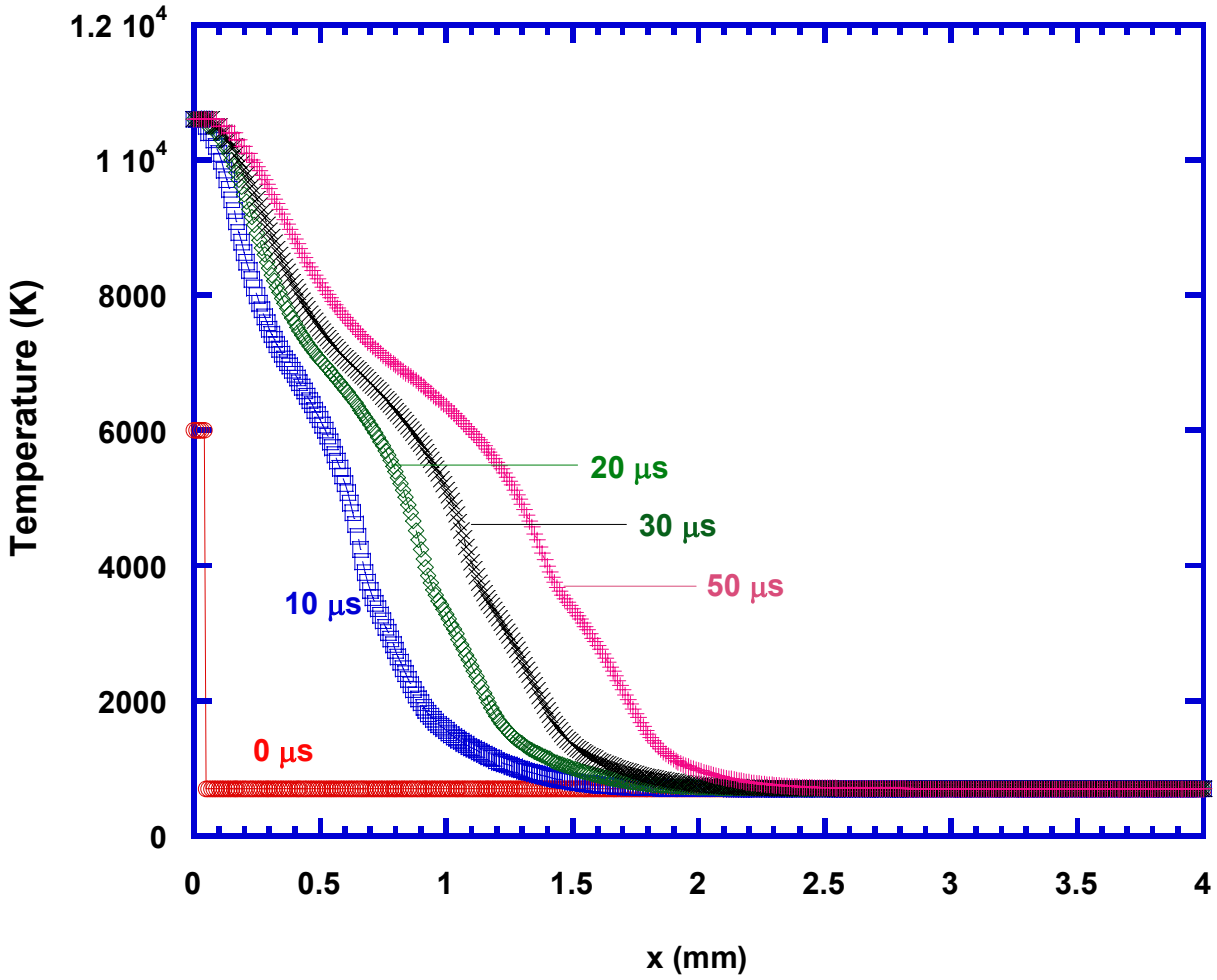

Figure 80. Temperature distribution at different times, variable C_p, adiabatic wall at x=0.

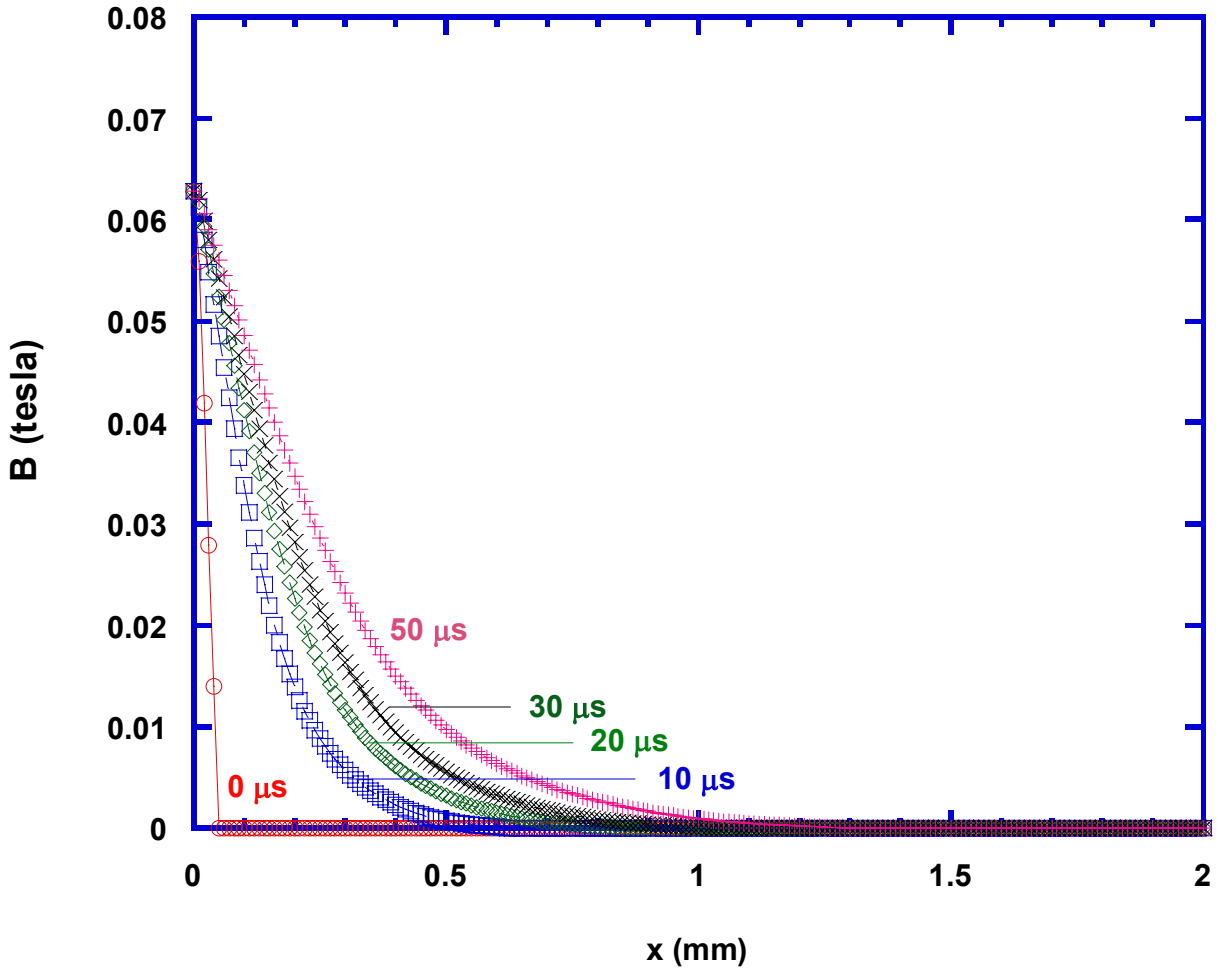

Figure 81. Magnetic field distribution at different times, variable C_p, adiabatic wall at x=0.

The second region is the low temperature non-conducting region that can be seen downstream. As a result of the magnetic field distribution, the arc root shows no motion in the x-direction. It is only expanding, and penetrating into the cold regions by preserving its maximum value at the back-wall.

Figure 83 shows the positions of arc current and temperature maxima as functions of time. It is important to note that arc current and temperature maxima are coincident. Therefore, the current model in this study makes it possible to define motion of the arc by motion of the temperature maximum, as suggested by Keefer (1989).

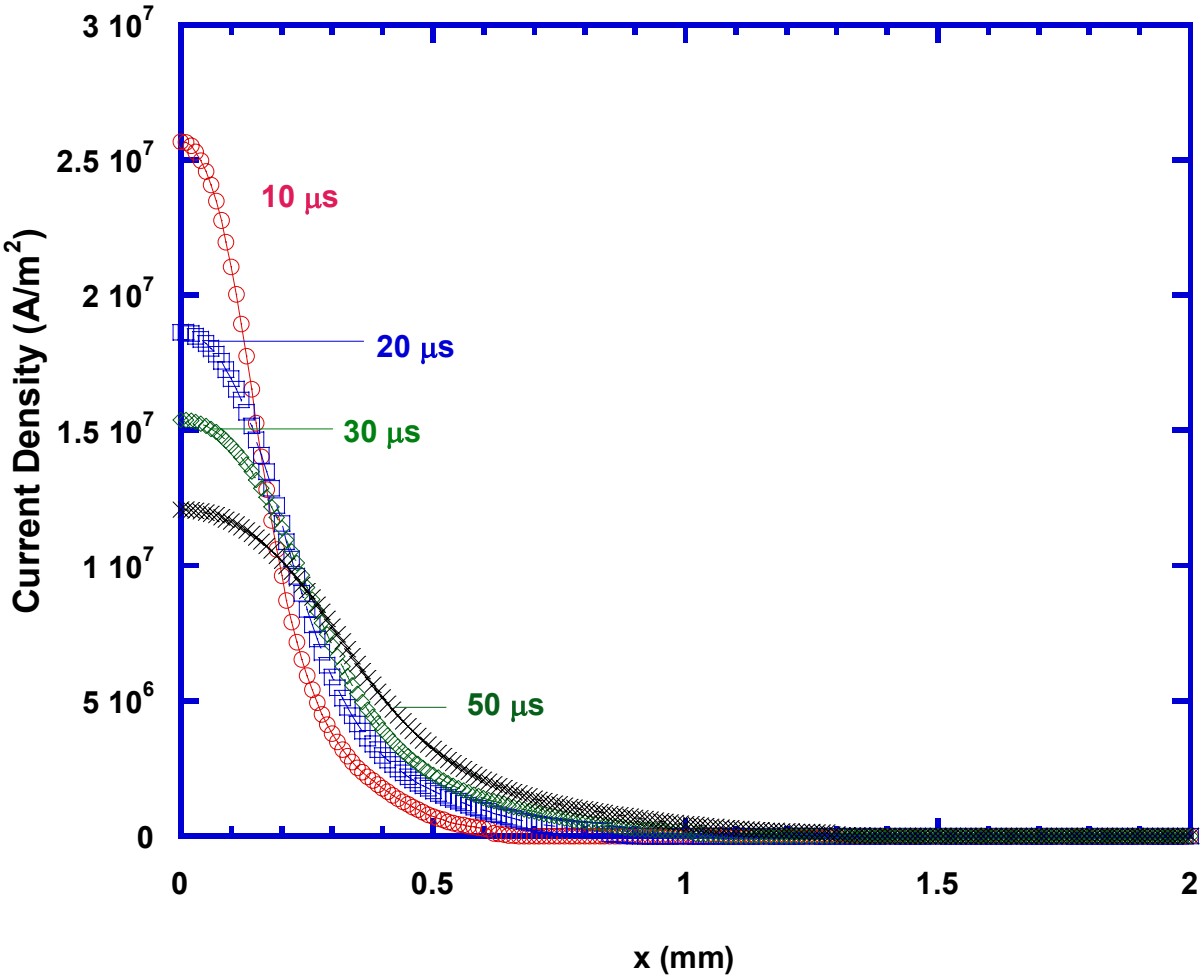

Figure 82. Current density distribution at different times, variable C_p, adiabatic wall at x=0.

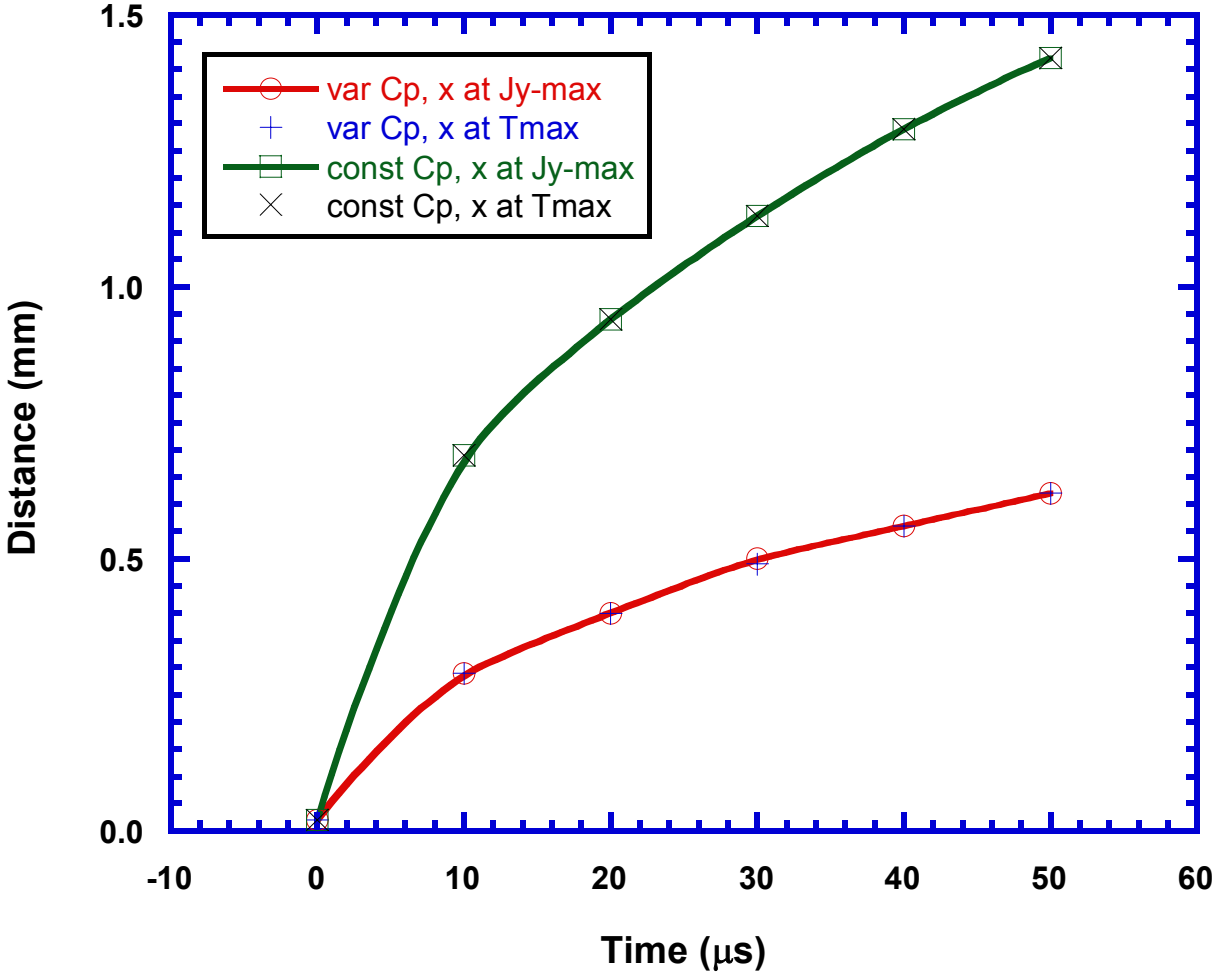

Figure 83. Maximum arc density and temperature variations over time for variable and constant specific heat cases.

The position of maximum arc density relative to time is given in Figure 84 using different total currents. It is seen that the magnitude of total current has a small effect on the final arc velocity. The difference in total travel distance is caused by the initial sudden expansion observed at early times and also by the slightly different slopes of location relative to time. For the relatively constant velocity regions seen in Figure 84 after 20 μsec, the maximum total current case gives a slope of 6.6 m/s while 5.4 m/s is found for the minimum total current case. A plot of maximum temperature in the computational domain as a function of total current is provided in Figure 85. The maximum temperature increases linearly with increasing current, but it should be kept in mind that some important physics, such as dissociation and ionization, are not included in the present simplified model. These will cause decreasing temperature but more moles of gas. Even with lower temperatures, expansion is still expected to be a significant effect.

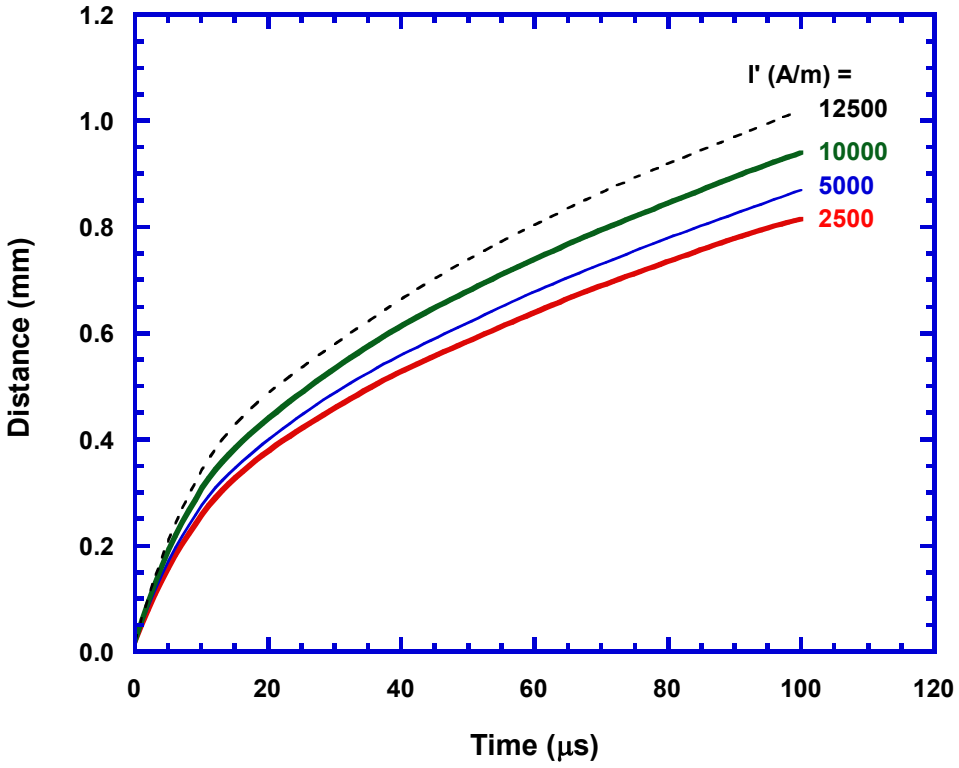

Figure 84. Effect of current on position of maximum arc density, variable C_p.

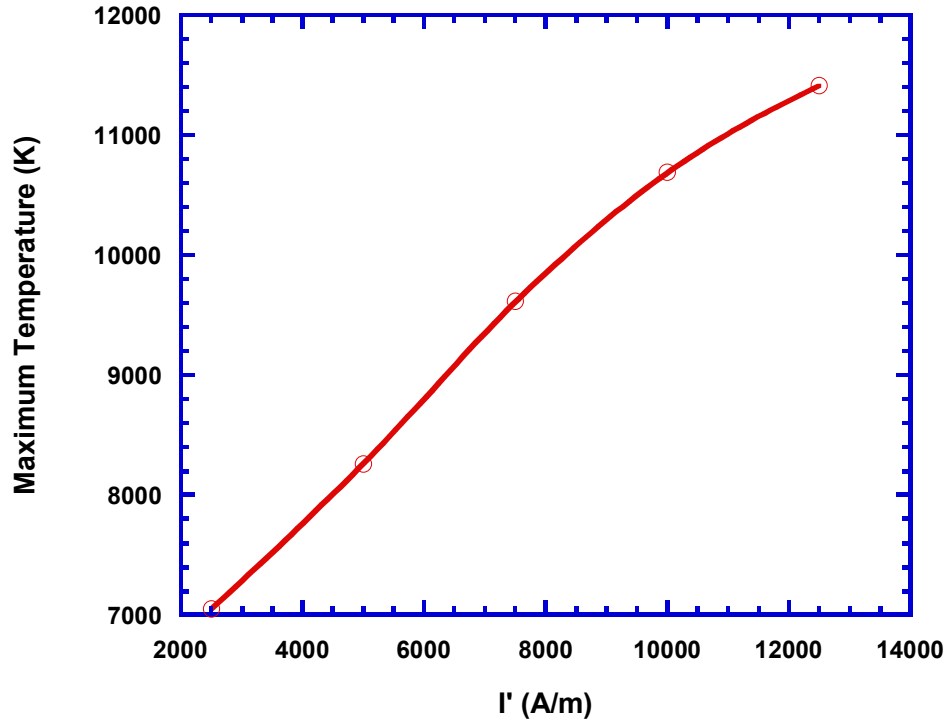

Figure 85. Maximum temperature as a function of current per unit width, variable C_p.

4. CONCLUSIONS

With funding from the DOE ARES program, the University of Texas conducted a study to fulfill two main objectives:

1) develop an improved understanding of the spark ignition process, and
2) develop the railplug as an improved ignitor for large bore stationary natural gas engines.

From the perspective of an improved understanding of the spark ignition process, the conclusions that can be drawn from the results of this study are:

(1) Spark duration decreases with increasing pressure. For example, the overall duration of the spark decreased from 2 ms at 1 bar to 1.5 ms at 6.6 bar (using a 23 kΩ internal resistance spark plug and a 1 mm spark gap). We plan to perform more tests to determine whether the same conclusion can be drawn with respect to gas density.

(2) Spark duration decreases as the size of the spark gap increases. The effect was weak at ~1 bar, but increased with increasing pressure (e.g., at ~7.8 bar, the spark duration for a 2 mm gap was about 1/3 that of a 0.5 mm gap).

(3) In agreement with prior results, the breakdown voltage was found to increase approximately linearly with spark gap size and pressure. We plan to perform more tests to determine whether the same conclusion can be drawn with respect to gas density.

(4) The voltage during both the arc and glow phases increases with increasing pressure, but weakly. We plan to perform more tests to determine whether the same conclusion can be drawn with respect to gas density.

(5) The glow phase was absent for spark discharges at pressures over ~7 bar. We plan to perform more tests to determine whether the same conclusion can be drawn with respect to gas density.

(6) The energy delivered to the spark gap increases approximate linearly with increasing pressure (e.g., from about 11 mJ at 1 bar to about 15 mJ at 18 bar). We plan to perform more tests to determine whether the same conclusion can be drawn with respect to gas density.

(7) For engines, spark duration affects mixture ignitability of both spark plugs and railplugs for lean mixtures. Increased energy delivered to the spark gap of spark plugs did not extend the Lean Stability Limit significantly for the range of conditions examined (a naturally aspirated light-duty engine operating on natural gas at WOT, MBT timing, and 1200 rpm).

(8) Most investigators mark the arc-to-glow transition when the current reaches some threshold value [e.g., 100 mA (Maly, 1984), 60 mA (e.g., Kim and Anderson, 1995)]. In fact, the transition current is a function of the electrode material. An available model (Loeb, 1939) can be used to predict the current at the end of the arc regime of the spark ignition process. This model, which is Equation 12 in this report, can be used to calculate the current at the end of arc given the cathode (ground electrode) area, the cathode fall voltage (15 V), and the cathode surface temperature. Our research team recommends using the melting temperature of the cathode material as the cathode surface temperature due to evidence that the arc-to-glow transition occurs when the melt can no longer be sustained.

We also developed the most complete model of the spark ignition process ever devised. The elements in this model include 1) the dynamic response of the ignition circuit, 2) a chemical kinetics mechanism that is suitable for the reactions that occur in the plasma, 3) conventional flame propagation kinetics, and 4) a multi-dimensional formulation so that bulk flow through the spark gap can be incorporated. The various elements of this model were developed over the duration of this project by several graduate students. Before graduating, the final PhD student on this project, Ozgur Ekici, will assemble all of these elements into a single Fortran code. Once completed, this version of the model (i.e., a Fortran code that can be used as a subroutine within an engine modeling code such as KIVA) can be obtained from Prof. Ron Matthews at rdmatt@mail.utexas.edu or Prof. DK Ezekoye at dezekoye@mail.utexas.edu. The conclusions that can be drawn from our ignition modeling effort include:

(1) The dynamics of the ignition circuit are important because the dynamic response of the ignition circuit dictates the rate of energy deposition to the gases within the spark gap. Equations 8 and 9 provide the breakdown voltage as a function of spark gap and gas pressure and temperature. Equations 10 and 11 provide the voltages during arc and glow and are fairly insensitive to the temperature, pressure, and composition of the gas. Equation 12 can be used to model the arc-to-glow transition if the melting temperature of the cathode material is used for the needed cathode temperature. For an inductive ignition system, the circuit parameters that have the most significant effects on energy deposition and the rate of energy deposition are the turns ratio, the core inductance, and the resistance of the primary windings of the coil. The resistances of the spark plugs and spark plug wires have a smaller effect but must be included in the model for the ignition circuit. The spark plug has an extremely small capacitance (~1 pF) but this capacitance plays an important role in the dynamics of the ignition circuit.

(2) The inclusion of plasma kinetics is important because these reactions are endothermic during breakdown and the early stages of arc but are a new route to thermal energy release as the plasma cools below 6000 K. As the plasma cools, the energy liberation due to recombination reactions involving the ionized species that were generated at very high temperature is an additional route to thermal energy liberation. This occurs on times scales when the young spark kernel is still very "fragile" and prior to significant energy release by flame propagation reactions. That is, as the plasma cools to below 6000 K, the plasma reactions must be accounted for because the recombination reactions help maintain a high temperature prior to the onset of the flame propagation reactions.

(3) The "blast wave" is important because it is a major sink (along with the endothermic plasma reactions) for the energy deposition from the ignition circuit. However, it is only important during the breakdown phase of the ignition process and extremely early in the arc phase (it has almost completely dissipated by 5 μs for the conditions simulated in our study).

(4) Another reason the blast wave is important is that rapid expansion behind the blast wave results in the pressure in the region of the spark gap rapidly decreasing to less than that of the unburned gas. In turn, this results in the inflow of "cold" unburned gas adjacent to the insulator and electrodes.

(5) Vortices form near the corners of the electrodes.

(6) Because heat transfer is a "slow" process relative to the electrical-to-thermal energy conversion process, heat losses to the electrodes are negligible during breakdown and the early stages of arc (10s of μs).

Fundamental experiments, engine experiments, and modeling tasks were used to help develop the railplug as a new ignitor for large bore natural gas engines. The conclusions that may be drawn from our investigations of railplugs are:

(1) In our prior railplug project, there was a sharp discontinuity in the volume between the two rails at the downstream end of the initiation gap. At the time, it was believed that the increase in the inductance gradient across this discontinuity would force the arc to continue to move across this discontinuity. However, it turned out that this discontinuity prevented the electromagnetic field from traveling further downstream. This discontinuity must be eliminated in the design of the railplug.

(2) The railplug ignition circuit (the "follow-on" circuit) should have a resistor, in parallel with the capacitor, that is as large as possible.

(3) The combination of capacitance and charging voltage should be no larger than required to assure ignition.

(4) An inductor should be used to shape the current profile.

(5) The distance the arc travels decreases with increasing pressure, and also depends on the level of delivered energy. We plan to perform more tests to determine whether the same conclusion can be drawn with respect to gas density.

(6) Smaller cross-sectional area rails (electrodes) have the potential to improve ignitability. Suitable analysis is required to optimize the size, however, because smaller electrodes have higher heat loading, leading to higher rail temperatures and the potential for pre-ignition.

(7) From engine tests, it is concluded that, compared to 18 mm spark plugs, railplugs can increase the burning rate of very lean mixtures and extend the lean stability limit (LSL). The engine tests showed that the LSL can be extended from a fuel/air equivalence ratio of $\phi = 0.59$ for the 18 mm spark plugs down to $\phi = 0.53$ using a railplug with the same delivered energy (0.7 J). However, this much delivered energy will rapidly deteriorate a spark plug. For a typical delivered energy for a spark plug (<0.05 J), the LSL for the spark plgu was $\phi = 0.63$.

(8) A permanent magnet can be used to aid the plasma movement. The engine tests showed that it improved the railplug performance. The LSL was extended to $\phi = 0.54$ with delivered energy as low as 0.15 J/shot, a typical discharge energy for commercial capacitive discharge ignition systems.

(9) Our railplug model revealed that both the geometry of the railplug and the dynamic response of the railplug's ignition circuit have significant effects on arc motion.

(10) Thermal expansion of the plasma plays an important role in arc movement.

(11) Our railplug model also revealed that the boundary condition at the upstream end of the railplug has a significant effect on arc evolution because of the strong temperature dependence of the electrical conductivity. It was also found that the magnetic Reynolds number is an important parameter and, for the cases considered

in this study, diffusion is the dominant mechanism for transport of the magnetic field and current density.

(12) The pressure between the rails decreases below the ambient pressure as a result of the expansion behind the shock wave that is a result of breakdown. This low-pressure region induces a strong back flow of the high-density, cold external gas toward the space between the electrodes. Effects of the inflowing cold gas and the recirculation near the downstream corners of the electrodes become apparent at times of the order of 150 μs. This compounds the decrease in maximum temperature of the plasma that results from heat losses to the rails and from decreasing energy deposition (i.e., reduction of the current with time). The cold gas flow into the region upstream of the arc together with the decrease in current result in reversal of the direction of arc motion – movement back upstream. This conclusion reinforces the necessity of "matching" the follow-on circuit to the railplug geometry to ensure that the arc continues moving until it reaches the end of the rails.

REFERENCES

Akram, M. (1996), "Two dimensional model for spark discharge simulation in air", *AIAA Jr*., **34**:1835-1845.

Anderson, R.W., and M.T. Lim (1985), "Investigation of misfire in a fast burn spark ignition engine", Combustion Science and Technology, **43**:183-196.

Anderson, R.W. (1987), "The effect of ignition system power on fast-burn engine combustion", SAE Paper 870549.

Bazelyan, E.M., and Y.P. Raizer (1998), Spark Discharge, CRC Press, Boca Raton.

Bhat, S., O.A. Ezekoye, and R.D. Matthews (2003a), "Impact of ignition circuit characteristics on spark gap energy deposition", submitted to the *International Journal of Engine Research*.

Bhat, S., O.A. Ezekoye, and R.D. Matthews (2003b), "Impact of railplug circuit parameters on energy deposition and durability", SAE Paper 2003-01-3135; also in: Spark Ignition and Compression Ignition Engines Modeling 2003, SAE Special Publication SP-1803; also in: *Journal of Fuels and Lubricants* **112**(4):2221-2233 (2004).

Borghese, A., A. D'Alessio, M. Diana, and C. Venitozzi (1988), "Development of hot nitrogen kernel, produced by a very fast spark discharge", Proceedings of the 22nd International Symposium on Combustion, pp. 1651-1659.

Boris, J.P., A.M. Landsberg, E.S. Oran, and J.H. Gardner (1993), LCPFCT- Flux-Corrected Transport Algorithm for Solving Generalized Continuity Equations, report NRL/MR/6410-93-7192, Naval Research Laboratory, Washington DC.

Boris. J.P, and D.L. Book (1997), "I. Shasta, a fluid transport algorithm that works", *Journal of Computational Physics*, **135**:172-186.

Borman, G., and K. Nishiwaki (1987), "Internal combustion engine heat transfer", *Prog. Energy Combust. Sci*., **13**:1-46.

Boulos, M.I., P. Fauchais, and E. Pfender (1994), Thermal Plasmas, Vol. 1, Plenum Press, New York.

Browne, W.G., D.R. White, and G.R. Smookler (1969), "A study of the chemical kinetics of shock heated H2/CO/O2 mixtures", Proceedings of the 12th International Symposium on Combustion, pp. 557-.

Cambel A.B. (1963), Plasma Physics and Magnetofluid Mechanics, McGraw-Hill Book Company, Inc., New York.

Cho, Y.S., D.A. Santavicca, and R.M. Sonntag (1992), "The effect of spark power on spark-ignited flame kernel growth", SAE Paper 922168.

Drellishak, K.S., D.P. Aeschliman, and A.B. Cambel (1965), "Partition functions and thermodynamic properties of nitrogen and oxygen plasmas", *The Physics of Fluids*, **8**: 1590-1560.

Druyvesteyen, M.J. (1939), *Z. Physics*, **111**:770-.

Edwards, C.F., A.K. Oppenheim, and J.D. Dale (1983), "A comparative study of plasma ignition systems", SAE Paper 830479.

Ekici, O., O.A. Ezekoye, and R.D. Matthews (2004a), "Arc evolution modeling for a railplug ignitor", Proceedings of the 2004 Technical Meeting of the Central States Section of the Combustion Institute, Austin, TX.

Ekici, O., V.J. Bokka, O.A. Ezekoye, and R.D. Matthews (2004b), "A numerical study of spark ignition", ASME Paper ICEF2004-884, presented at the ASME Internal Combustion Engine Division Conference, Long Beach, CA, October 2004, in Proceedings of the ASME Internal Combustion Engine Division: 2004 Fall Technical Conference.

Ekici, O., O.A. Ezekoye, M.J. Hall, and R.D. Matthews (2005), "A numerical study of a railplug ignitor", Proceedings of the 2005 Fourth Joint Meeting of The US Sections of The Combustion Institute, Philadelphia, PA.

Ellzey, J.L., M.J. Hall, X. Zhao, and H. Tajima (1993), "Computational and experimental study of a railplug ignitor," *Experiments in Fluids*, **14**:416-422.

Fincke, J.R., R.P. Anderson, A.H. Timothy, and B.A. Detering (2002), "Plasma pyrolysis of methane to hydrogen and carbon black", *Ind. Eng. Chem. Res*., **41**:1425-1435.

Frendi, A., and M. Sibulkin (1990), "Dependence of minimum ignition energy on ignition parameters," *Combustion Science and* Technology, **73**:395-413.

Gao, H., R.D. Matthews, M.J. Hall, and S. Hari (2004a)," From spark plugs to railplugs – the characteristics of a new ignition system", SAE Paper 2004-01-2978; also in: *Journal of Engines*, **112**(3):1546-1556 (2005).

Gao, H., R.D. Matthews, S. Hari, and M.J. Hall. (2004b), "Use of railplugs to extend the Lean Limit of natural gas engines", ASME Paper ICEF 2004-881, presented at the ASME Internal Combustion Engine Division Conference, Long Beach, CA, October 2004, in Proceedings of the ASME Internal Combustion Engine Division: 2004 Fall Technical Conference.

Gao, H., O.A. Ezekoye, M.J. Hall, and R.D. Matthews (2005a), "A new ignitor for large-bore natural gas engines – Railplug design improvement and optimization", SAE Paper 2005-01-0249, also in: SI Combustion and Direct Injection SI Engine Technology, pp. 364-177, SAE Special Publication SP-1972, ISBN 0-7680-1617-7.

Gao, H., M.J. Hall, O.A. Ezekoye, and R.D. Matthews (2005b), "Railplug design optimization to improve large-bore natural gas engine performance", ASME Paper ICES 2005-1031, to be presented at the ASME Internal Combustion Engine Division Conference,

Chicago, Illinois, April 5-7; in Proceedings of the ASME Internal Combustion Engine Division: 2005 Spring Technical Conference, ISBN 0791841847.

Gao, H. (2005), "Investigation of a Railplug Ignition System for Lean-Burn Large-Bore Natural Gas Engines," Ph.D. dissertation, Mechanical Engineering Department, The University of Texas at Austin.

Gupta, R.N., J.M. Yos, R.A. Thompson, and K-P. Lee (1990), "A review of reaction rates and thermodynamic and transport properties for an 11-species air model for chemical and thermal non-equilibrium calculation to 30000 K", NASA Reference Publication 1232.

Hall, M.J., H. Tajima, R.D. Matthews, M.M. Koeroghlian, W.F. Weldon, and S.P. Nichols (1991), "Initial studies of a new type of ignitor: the railplug", SAE Paper 912319.

Hari, S., M.J. Lee, M.J. Hall, O.A. Ezekoye, and R.D. Matthews (2005), "Analysis of factors that affect the performance of railplugs", SAE Paper 2005-01-0252, presented at the SAE Congress, Detroit, MI, April; also in SI Combustion and Direct Injection SI Engine Technology, pp. 403-416, SAE Special Publication SP-1972, ISBN 0-7680-1617-7.

Herweg, R., and R.R. Maly (1992), "A fundamental model for flame kernel formation in S.I. engines", SAE Paper 922243.

Hori, T., M. Shibata, S. Okabe, and K. Hashizume (2003), "Super ignition spark plug with fine center and ground electrodes", SAE Paper 2003-01-0404.

Huerta, M.A., and G.C. Boynton (1991), "Two-dimensional heat conducting simulation of plasma armatures," *IEEE Trans. Magnetics*, **27**:261-265.

Howatson, A.M. (1976), An Introduction to Gas Discharges, Pergamon Press, Oxford.

Karetta, F., and M. Lindmayer (1998), "Simulation of the gasdynamics and electromagnetic processes in low voltage switching arcs," *IEEE Trans. Components, Packaging, and Manufacturing Tech*., **21**:96-103.

Karim, G.A., T.J. Himyary, and J.D. Dale (1989), "An examination of the combustion processes of a methane fuelled engine when employing plasma jet ignition", SAE Paper 891639.

Keefer, D.R. (1989), "Arc motion in railgun plasma armatures," *IEEE Trans. Plasma Science*, **17**:446-449.

Kim, J., and R.W. Anderson (1995), "Spark anemometry of bulk gas velocity at the plug gap of a firing engine", SAE Paper 952459.

Kochubei, V.F., and F.B. Moin (1969), "Kinetics of the reaction of CO2 with hydrogen", *Kinet. Catal.* pg. 992.

Kravchik, T., E. Sher, and J.B. Heywood (1995), "From spark ignition to flame initiation", *Combustion Science and Technology*, **108**:1-30.

Kulsrud, R.M. (1989), "MHD description of plasma" in Basic Plasma Physics, edited by A.A. Galeev and R.N. Sudan, North-Holland Pub., Netherlands.

Lee, M., M.J. Hall, O.A. Ezekoye, and R.D. Matthews (2005), "Voltage and energy deposition characteristics of spark ignition systems", SAE Paper 2005-01-0231. presented at the SAE Congress, also in SI Combustion and Direct Injection SI Engine Technology, pp. 143-156, SAE Special Publication SP-1972, ISBN 0-7680-1617-7.

Loeb, L.B. (1939), Fundamental Processes of Electrical Discharge in Gases, John Wiley and Sons, New York.

Maly, R., B. Saggau, E. Wagner, and G. Ziegler (1983), "Prospects of ignition enhancement", SAE Paper 830478.

Maly, R. (1984), "Spark ignition: its physics and effect on the internal combustion engine", in Fuel Economy in Road Vehicles Powered by Spark Ignition Engines, Chapter 3, pp. 91-148, Editors: J.C. Hilliard and G.S. Springer, Plenum Press, New York.

Matthews, R.D., M.J. Hall, R.W. Faidley, J.P. Chiu, X.W. Zhao, I. Annezer, M.H. Koenig, J.F. Harber, M.H. Darden, W.F. Weldon, and S.P. Nichols (1992), "Further analysis of railplugs as a new type of ignitor", SAE Paper 922167, also in: *Journal of Engines* **101**(3):1851-1862..

McMillian, M.H., S. Woodruff, S. Richardson, and D. McIntyre (2004), "Laser spark ignition: laser development and engine testing", Proceedings of the ASME ICE Division 2004 Fall Technical Conference, ICEF2004-917.

Meek, J.M., and J.D. Craggs (1953), Electrical Breakdown of Gases, Oxford at the Clarendon Press, Chapter 12.

Mick, H-J., M. Burmeister, and P. Roth (1993), "Atomic resonance absorption spectroscopy measurements on high-temperature CO dissociation kinetics", *AIAA J.*, **31**:671-676.

Miyamoto, H., H. Ogawa, and K. Doi (1990), "Calculations of ignition lags for methane-air mixtures by chemical kinetics", International Symposium COMODIA 90, pp. 99-104.

Ozdor, N., M. Dulger, and E. Sher (1994), "Cyclic variability in spark ignition engines: a literature survey", SAE Paper 940987.

Pischinger, S., and J.B. Heywood (1988),"A study of flame development and engine performance with breakdown ignition systems in a visualization engine", SAE Paper 880518.

Powell, J.D., and J.H. Batteh (1981), "Plasma dynamics of an arc-driven, electromagnetic, projectile accelerator," *J. Appl. Phys*., **52**:2717-2730.

Raether, H. (1964), Electron Avalanches and Breakdown in Gases, Butterworths, Washington.

Rehm, R.G., and H.R. Baum (1978), "The equations of motion for thermally driven, buoyant flows," *Journal of Research of the National Bureau of Stand*ards, **83**:297-308.

Ronney, P.D. (1994), "Laser versus conventional ignition of flames", *Optical Engineering* **33**(2):510-521.

Saito, H., T. Sakurai, T. Sakonji, T. Hirashima, and K. Kanno (2001), "Study on lean burn gas engine using pilot oil as the ignition source", SAE Paper 2001-01-0143.

Schroeder, C. (2002), www.beyond-designs.com/pspice_inductive.htm (accessed March 2002).

Seers, P. (2003), "Spark ignition: an experimental and numerical investigation," Ph.D. dissertation, Department of Mechanical Engineering, The University of Texas at Austin.

Sher, E., J. Ben-Ya'ish, and T. Kravchik (1992), "On the birth of spark channels", *Combustion and Flame*, **89**:186-194.

Sloane, T.M. (1990), "Numerical simulation of electric spark ignition in atmospheric pressure methane air mixtures", *Combustion Science and Technology,* **73**:367-381.

Smith, G.P., D.M. Golden, N.F. Nigel, W. Moriarty, B. Eiteneer, M. Goldenberg, C.T. Bowman, R.K. Hanson, S. Song, W.C. Gardiner, V.V. Lissianski, and Z. Qin, (downloaded 2002), `http://www.me.berkeley.edu/gri_mech/`

Sze, S.M. (1969), Physics of Semiconductor Devices, Chapter 5, John Wiley and Sons, New York.

Tannehill, J.C., Anderson, D.A., and Pletcher, R.H., Computational Fluid Mechanics and Heat Transfer, Taylor & Francis Press, Washington, DC, 1997.

Sedov, L. I. (1959), Similarity and Dimension Methods in Mechanics, Academic Press, New York.

Thiele, M., S. Selle, U. Riedel, J. Warnatz, and U. Maas (2000), "Numerical simulation of spark ignition including ionization", *Proceedings of the Combustion Institute,* **28**:1177-1185.

von Engel, A. (1965), Ionized Gases, second edition, Oxford at the Clarendon Press.

Westbrook, C.K., and F.L. Dryer (1981), "Simplified reaction mechanism for the oxidation of hydrocarbon fuels in flames", *Combustion Science and Technology*, **27**:31-43.

Westbrook, C.K., and F.L. Dryer (1984), "Chemical kinetic modeling of hydrocarbon combustion", *Progress in Energy and Combustion Science*, **10**:1-.

Zahn, M. (1979), Electromagnetic Field Theory, John Wiley & Sons, New York.

Zheng, J., S. Capiaux, J.P. Chiu, R.D. Matthews, R.W. Faidley, M.H. Darden, W.F. Weldon, and S.P. Nichols (1993), “Effects of railplugs on the dilution tolerance of a spark ignition engine”, SAE Paper 931800.

LIST OF FIGURES

LIST OF TABLES

LIST OF ACRONYMS AND ABBREVIATIONS

A	a Richardson Constant (Equations 13 and 15)
A_C	cross-sectional area
A_i	the i^{th} level of ionized particle
ARES	Advanced Reciprocating Engine Systems
B	strength of the local magnetic field
B	a Richardson Constant (Equations 13 and 14)
$\vec{B}$	the vector of B
B_z	magnetic field strength in the z direction
Bi	Biot number
C	capacitance
C_m	mean-piston-speed
C_p	constant pressure specific heat
C_v	constant volume specific heat
COV	coefficient of variability (the standard deviation normalized by the mean)
d	separation distance between the centroids of the rails
D_i	species diffusivity
DOE	U.S. Department of Energy
e	specific internal energy
E	total energy per unit volume
$\vec{E}$	electric field vector
E_d	delivered energy
E_J	discharge energy
EGR	exhaust gas recirculation
F	force
f	cathode area
FCT	Flux Corrected Transport
g	spark gap size
h	Planck's constant (6.63E-34 J-s)
h_c	convective heat transfer coefficient
i	current

i_t	the thermionic current
I	total current
I’	current per unit width of spark channel
IC	internal combustion
IMEP	indicated mean effective pressure
J	current flow per unit area
$\vec{j}$	current density (the vector of J)
j_y	y-component of the current density
j_z	current density in the z direction
K_{i+1}	equilibrium constant for ionization from level i to level (i+1)
k	thermal conductivity
k	Boltzmann’s constant [1.380E-23 J/K]
L	inductance
L’	inductance gradient (inductance per unit length of the rails)
L	rail length
LPP	location of peak pressure
LSL	lean stability limit; the fuel/air equivalence ratio at which the COV of IMEP = 10%
M_i	molecular weight of species i
m	effective mass (the mass of a free electron for metals)
m_e	electron rest mass.
n_e	number density of electrons
n_i	number density of ionized particles at the i^{th} level
n_{i+1}	number density of ionized particles at the $(i+1)^{th}$ level
NOx	oxides of nitrogen
p	perimeter of the electrode
P	pressure
q	charge on an electron [1.602E-19 A-s/electron]
$\dot{q}'''_{ch}$	rate of energy release or absorption via chemical reactions per unit volume
$\dot{q}'''_{el}$	rate of Joule heating of the gas per unit volume
r	radial coordinate
R	resistance

R	universal gas constant [8.314 kJ/kmole-K]
R_a	aspect ratio (the rail length divided by the rail separation)
Re_m	the magnetic Reynolds number, defined in Equation 45
rpm	revolutions per minute
SAE	Society of Automotive Engineers
t	time
T	temperature
T^*	non-dimensional electrode temperature
T_B	the temperature of the plug base
T_c	cathode surface temperature
T_g	the in-cylinder gas temperature
u	x-component of velocity
$u\|_0$	velocity at x = 0
u_i	ionization energy for the i^{th} level of ionization
$\vec{u}_e$	velocity vector of the charged particles
UT	University of Texas
V	voltage
V_{arc}	arc voltage
V_{BD}	breakdown voltage
V_C	the cathode fall voltage
V_{glow}	glow voltage
$\vec{V}$	velocity vector
WOT	wide open throttle
x	distance, axial coordinate
y	coordinate that is orthogonal to x and z in the Cartesian coordinate system
Y_i	mole fraction of species i
z	transverse coordinate
Z	partition function

Greek:

β	parameter defined in Equation 6b

μ	dynamic viscosity
μ'	bulk viscosity
μ_o	permeability constant ($4\pi*10^{-7}$ T-m/A, where 1 Tesla = 10^4 Gauss)
υ	specific volume
ρ	gas density
σ	the Stefan-Boltzmann constant [5.67E-8 W/(m^2-K^4)]
σ_e	electrical conductivity of the plasma
ϕ	the fuel/air equivalence ratio
ϕ	the work function of a metal
χ	non-dimensional parameter in Equations 8 and 9